Superconductivities of High-T_c Materials and Alkali Compounds of Buckminsterfullerene

Thesis by
Guanhua Chen

In Partial Fulfillment of the Requirements
for the Degree of
Doctor of Philosophy

California Institute of Technology
Pasadena, California
1992
(Submitted May. 19, 1992)

To MY FAMILY

Acknowledgments

My Ph.D study at Caltech has been and always will be the most unforgettable experience of my life. During the years, I have benefited from the help of many generous people. I would like to take this opportunity to express my deep appreciation to them.

Bill Goddard is the most influential person in my academic life at Caltech. I thank him for his support and guidance. I especially enjoyed the intellectual freedom under his supervision.

Collaborating with Yuejin Guo, Naoki Karasawa, Jean-Marc Langlois and Hong-Qiang Ding on various projects has expanded my horizons and broadened my knowledge. I learned much from each one of them. The discussions with Yuejin and Naoki, the topics of which covered a wide range of scientific subjects, were ever so stimulating and eye-opening. In the early days, Jean-Marc's help with the computer system was invaluable. I would also like to thank him and Dr. Siddharth Dasgupta for helping me understand Group Theory, an essential part of my later work on C_{60}. Collaboration with Dr. Ding on Heisenberg Model culminated in *Section 1.3* of my thesis.

Alan Mathiowetz has been a tolerant roommate and a good friend. I thank him for many lively conversations. He helped me understand more about American culture. As a system manager of our group, he helped me solve many problems I encountered with the computer.

I would like to thank Bob Donnelly and Kian-Tat Lim for their help with the graphics so that I didn't have to resort to the primitive art of cut and paste during the preparation of this thesis. Toshi Takeuchi's help with Quantum Graph

was also invaluable.

I also would like thank our system managers, Kian-Tat Lim, Alan Mathiowetz, Terry Coley, and Rick Muller for their patience and time.

Jeannie Chen has been the most important person in my life during the past two years. I appreciate her companionship, understanding, and encouragement. She patientlly read the draft of this manuscript, corrected many grammar and spelling mistakes, and detected some errors in logic.

Finally, I would like to thank all members of the Goddard group for numerous help, especially my closest neighbors Ann Miller, Charles Musgrave, Xinlei Hua, Ersan Demiralp, and Changmoon Park.

Abstract

This thesis is composed of two chapters. Chapter I is an investigation of the spin wave spectrum of the two-dimensional spin-1/2 Heisenberg model and its relevance to high-T_c superconducting materials. Chapter II is a study on another interesting family of superconductors, the alkali compounds of Buckyminsterfullerene A_xC_{60}. The electron-phonon coupling constant of one member of these compounds, K_3C_{60}, has been calculated and discussed in the context of the phonon-mediated superconducting mechanism.

Chapter 1 consists of two projects. The first project is an exact diagonalization of a 4×4 S = 1/2 Heisenberg model. Energy vs. momentum spectra is derived and compared with the dynamic structure factors. The comparison shows that spin wave or magnon of a certain momentum corresponds to the lowest spin triplet state of that particular momentum. The second project, an extension of the first, is a Projector Monte Carlo simulation of 2D S = 1/2 Heisenberg square lattices of size 4×4, 6×6, 8×8 and 12×12. The lowest lying spin wave spectrum has been obtained for each of the above lattices, and the extrapolation to the infinitely large 2D square lattice has been derived. These results suggest that the exact spectrum for the infinite lattice is that of linear magnon with an overall renormalization factor. These results are also used to infer the value of the exchange energy from inelastic neutron scattering experiments of a high-T_c superconductor La_2CuO_4.

The first part of Chapter 2 is a MNDO study of the electronic structure of a C_{60} molecule; this study excludes a proposed mechanism for the superconductivity in A_xC_{60}, namely, Stability of Molecular Singlets ("SMS"). Secondly, Chapter II

describes an investigation of the electron-phonon interaction caused by the changes of the electron-ion coulomb interactions, i.e., the static electron-phonon coupling. An accurate formalism based on the force field and phonon spectrum available is established to calculate the electron-phonon coupling matrix. This formalism includes exactly the available information about the phonon eigenvectors and eigenenergies and about the localized Wannier orbital for electrons in the conduction bands. The major contributions to the static electron-phonon coupling is found from the low frequency intermolecular phonon modes. Thirdly, a study on the electron-phonon coupling caused by the responses of the local electronic states to the vibrations of a C_{60} molecule (i.e., dynamic electron-phonon coupling) is presented. The study concludes that the dynamic coupling is strong enough to be relevant to the superconductivity in A_xC_{60}. Finally, various properties related to the superconducting phase have been calculated, and are compared with the experimental results. On the basis of all these, an experiment is proposed to confirm our findings, and to determine the superconductivity mechanism in A_xC_{60} systems.

Table of Contents

Chapter 1.

The 2D Heisenberg Model and High-T_c Superconductivity

Guanhua Chen and William A. Goddard III

Materials Simulation Center, Beckman Institute

California Institute of Technology, Pasadena, CA 91125

1.1 Model

Since the discovery of high T_c superconductors[1], many mechanisms[2-7] have been proposed to explain the superconductivity in these materials. All high T_c superconductors share the following structural and crystal-chemical properties[8]. Superconductivity is associated with CuO_2 planes, which are separated from each other by "charge reservoir" building blocks and cation blocks; the number of closely spaced CuO_2 layers can vary from 1 to 4, and the "charge reservior" units involve, e.g., $Bi-O$, $Tl-O$ layers; in $YBa_2Cu_3O_7$, the $Cu-O$ chains act also as "charge reserviors" while the apical oxygen atoms, connecting planes and chains, move in response to the charge transfer between these two building blocks. *ab initio* calculations on Cu_xO_y (x=2,3;y=10-12) by Guo, Langlois and Goddard [9] indicate that the high T_c superconductors also have the following characteristics :

1) A network of Cu^{II} (d^9) sites with the singly occupied d orbital localized in the plane of four short $Cu-O$ bonds (~ 9Å).
2) The spins of adjacent d electrons are coupled antiferromagnetically by superexchange.
3) Oxidation of the system beyond Cu^{II} leads not to Cu^{III} as was suggested earlier but rather to holes localized in the p orbitals of oxygen atoms[9].
4) The magnetic coupling of the singly occupied oxygen orbitals with the adjacent copper d electrons is antiferromagnetic if the singly occupied orbital is $p\sigma$, and ferromagnetic if the orbital is $p\pi$.

Given these results, we propose the following Hamiltonian[2],

$$H_{eff} = H_d + H_{pd} + H_p, \tag{1}$$

where

$$H_d = -\sum_{<didj>} 2J_{dd}\mathbf{S}_{di}\cdot\mathbf{S}_{dj} \tag{2}$$

is the Hamiltonian for interaction of d electrons on adjacent Cu^{II}; $\mathbf{S}_{di}$ is the spin operator for a d electron on site di; and J_{dd} is the exchange energy (negative) between adjacent copper d electrons.

$$H_{pd} = -\sum_{<pidj>} 2J_{pd}\mathbf{S}_{pi}\cdot\mathbf{S}_{dj} \tag{3}$$

represents the interaction between oxygen p holes and adjacent copper d electrons. $\mathbf{S}_{pi}$ is the spin operator for a p electron on site pi, and J_{pd} is the exchange energy between adjacent oxygen p and copper d electrons.

H_p is the Hamiltonian for p holes on oxygens, which describes holes on oxygen hopping to the adjacent oxygen site. In Ref. [2], we write it as the following,

$$H_p = \sum_{<pipj>\sigma} t_{pi\sigma pj\sigma} a^{+}_{pi\sigma} a_{pj\sigma}, \tag{4}$$

where $a^{+}_{pi\sigma}$ and $a_{pi\sigma}$ are creation and annihilation operators for holes with spin σ on oxygen site pi; $t_{pi\sigma pj\sigma'}$ is the hopping matrix element between site pi with spin σ to the adjacent site pj. Here we omit spin exchanges between Cu d electrons and O p holes as holes hop to the adjacent site through Cu. It is a good approximation if holes are on oxygen pπ orbitals. Lang, Ding and Goddard investigated the effects of these spin exchange hoppings on superconductivity[10].

The above model is being supported by the results of many later experiments. Photoemission experiments[11,12] show a sharp fermi edge that is clearly indicting the fermi liquid or near fermi liquid characters of the system. Resonant photoemission

experiments[11] also reveal that the bands near and across the fermi edge are dominated by oxygen p character. Furthermore, the Knight shifts[13] of both Cu and O in the planes are proportional to the static susceptibility $\chi(\omega = 0, \mathrm{q} = 0)$, strongly supporting the notion that the spin density on the $\mathrm{Cu} - 3\mathrm{d}$ and $\mathrm{O} - 2\mathrm{p}$ state are not only closely connected but are also part of the same single component system. This indicates that the O hole has $\mathrm{p}\sigma$ character rather than $\mathrm{p}\pi$. Neutron Scattering experiments[14] performed on undoped La_2CuO_4 measured correlation lengths, which revealed that localized spins on Cu behave as the 2D Heisenberg model[14].

To understand the origin of superconductivity in these materials, one has to understand the behavior of the undoped CuO_2 sheet, which is best described by the 2D square $\mathrm{S} = 1/2$ Heisenberg model. With this model we concentrate on the excitation spectra and compare them with those of the spin wave theory. In Section 1.2, we present an exact diagonalization of 2D $\mathrm{S} = 1/2$ Heisenberg Hamiltonian on 4×4 square lattice[15]. In Section 1.3 we use the Projector Quantum Monte Carlo method to study the lattices of the size 4×4 up to 12×12 [16,17]. In section 1.4 we summarize the current status of research on experiments.

1.2

The Exact Excited States of Heisenberg Hamiltonian on 4 × 4 Lattice

Guanhua Chen and William A. Goddard III

Materials Simulation Center, Beckman Institute

California Institute of Technology, Pasadena, CA 91125

Abstract

We solve the exact eigenstates for various excited states of 2-dimensional spin-1/2 Heisenberg Hamiltonian on a 4×4 square lattice. Comparison with the dynamical structure factor $S(\mathbf{k}, \omega)$ at $T = 0$ shows that the magnon state corresponds to the lowest excited triplet state ($\mathbf{S} = 1$) at each $\mathbf{k}$.

1.2.1 Introduction

The interest in 2D spin-1/2 Heisenberg model has been growing because of its possible role in the superconductivity of high-Tc materials[1]. Direct diagonalization and Monte Carlo calculation have been done on lattices with various sizes[18-23], and many spin wave theories have been proposed[24-28]. In the meantime, the following questions have not been fully addressed : 1) What does the energy vs. momentum spectra look like ? 2) To what states does the spin wave or magnon correspond ? and 3) Where is the spin wave located in the energy spectra ? Although for 1D spin-1/2 Heisenberg model these issues have been solved[29,30] (1D energy spectra is a "belt" like spectra and spin wave locates at the bottom of the "belt"), for the 2D Heisenberg model however, the same issues have been neglected, except for some consensus that 2D and 1D behave much in the same fashion. Thus, it will be interesting to explore these issues explicitly. By obtaining the energy spectra and comparing them with the dynamical structure factor of the 4 $\times$ 4 square lattice, the above questions can be answered.

1.2.2 Exact Diagonalization:

The antiferromagnetic Heisenberg Hamiltonian is,

$$H = \sum_{<i,j>} J\, \mathbf{S}_i \cdot \mathbf{S}_j. \tag{5}$$

For 4 $\times$ 4 spin system there are 2^{16} configurations. By making use of spin conservation and translational invariance, we reduce the size of the Hamiltonian matrix. For instance, the reduced Hamiltonian matrix is only 822 $\times$ 822 for a subspace with a total spin z-component $M_z = 0$ and momentum $K = 0$. Therefore, we may obtain all eigenstates and their correspondent eigenenergies for 4 $\times$ 4 system.

To obtain the reduced Hamiltonian matrix, we need to construct the states with translational symmetry and constant total spin z-component. This can be accomplished in two steps. (1) Pick a configuration ϕ_0 with the desired total spin z-component. (2) Apply the following translational operation on it :

$$\begin{aligned} \Psi(\mathbf{k}) &= \mathrm{T}(\mathbf{k})\,\phi_0, \\ &= \frac{1}{\mathrm{N}} \sum_{\mathbf{r}} \exp(-i\mathbf{k}\cdot\mathbf{r})\,\phi_{\mathbf{r}}.' \end{aligned} \tag{6}$$

where ϕ_0 is a spin configuration, and $\phi_{\mathbf{r}}$ is a configuration obtained after translating ϕ_0 by $\mathbf{r}$ in space; $\Psi(\mathbf{k})$ is a new state with constant $\mathbf{M}_z$ and momentum $\mathbf{k}$; and $\mathrm{T}(\mathbf{k})$ is an operator which constructs a wavefunction of translational symmetry and momentum $\mathbf{k}$. Since the size of the reduced Hamiltonian matrix is only about 800 $\times$ 800, it can be solved exactly.

1.2.3 Dynamic Spin Structure Factor

The dynamic spin structure factor at zero temperature T = 0 is a probe for energies of magnon states. Knowing the ground state wavefunction, it can be obtained by a projective technique for the memory-function formalism[31,32,33].

Denote

$$\mathrm{A} = \sum_{\mathrm{j}} e^{i\mathbf{k}\cdot\mathbf{r}_j} \mathrm{S}^z_{\mathrm{j}}. \tag{7}$$

Then the dynamic spin correlation function is[31]

$$\mathrm{S}(\mathbf{k},\mathrm{t}) = < \psi_0 | \mathrm{A}^\dagger(\mathrm{t})\mathrm{A}(0) | \psi_0 >, \tag{8}$$

where $|\psi_0>$ is the ground state wavefunction and $\mathrm{A}^\dagger(\mathrm{t}) = e^{i\mathrm{Ht}}\mathrm{A}^\dagger e^{-i\mathrm{Ht}}$. Neutron scattering experiment measures directly the Fourier transform of $\mathrm{S}(\mathbf{k},\mathrm{t})$, i.e. the dynamic spin structure factor $\mathrm{S}(\mathbf{k},\omega)$, which is given by[31]

$$\mathrm{S}(\mathbf{k},\omega) = \sum_{\mathrm{n}} < \psi_0 | \mathrm{A}^\dagger | \psi_{\mathrm{n}} >< \psi_{\mathrm{n}} | \mathrm{A} | \psi_0 > \cdot \delta(\omega - (\mathrm{E}_{\mathrm{n}} - \mathrm{E}_0)), \tag{9}$$

where the summation is taken over all the eigenstates $|\psi_n>$ of H with energy E_n, where E_0 is the ground state energy.

To obtain the dynamic spin structure factor, define

$$G_s(E) =< \psi_0|A^\dagger(E-H)^{-1}A|\psi_0> . \tag{10}$$

And $S(\mathbf{k},\omega)$ is obtained as

$$S(\mathbf{k},\omega) = \pi^{-1}ImG_s(\omega + i\eta + E_0). \tag{11}$$

While $G_s(E)$ is written in the form of a continued fraction:

$$G_s(E) = \frac{<\psi_0|A^\dagger A|\psi_0>}{E - a_0 - \frac{b_1^2}{E-a_1-\frac{b_2^2}{E-\ldots}}}, \tag{12}$$

where the coefficients a_n and b_n can be evaluated by a projective technique developed for the memory-function formalism[31,32,33]. The procedure is as follows[31]: (1) Define the state $|f_0>= A|\psi_0>$; (2) generate a set of orthogonal states with the relation

$$|f_{n+1}>= H\,|f_n> - a_n|f_n> - b_n^2|f_{n-1}>, \tag{13}$$

and

$$a_n =< f_n|H|f_n> / < f_n|f_n>, \tag{14}$$

$$b_n =< f_{n+1}|f_{n+1}> / < f_n|f_n>, b_0 = 0. \tag{15}$$

1.2.4 Results

(1) Energy Spectra

Table 1.lists energy **E**, total spin **S** of the lowest energy state for each momentum **k** and excited energy Δ**E**.

$\mathbf{k_x}(\frac{\pi}{2})$	$\mathbf{k_y}(\frac{\pi}{2})$	**S**	**E(J)**	Δ**E(J)**
0	0	0	−11.2285	
0	1	1	−8.7944	2.4341
0	2	1	−8.5183	2.7102
1	1	1	−8.5183	2.7102
1	2	1	−8.8864	2.3421
2	2	1	−10.6499	0.5786

The ground state has momentum $\mathbf{k} = 0$ and total spin $\mathbf{S} = 0$ and the lowest lying excited states have $\mathbf{S} = 1$.

Fig (1) is the energy spectra with $\Delta E \leq 5.0J$ for total spin $S = 0, 1, 2, 3$. Notice that the spectra are "belt"-like, just as 1D Heisenberg spectra; below a certain energy level, there are no available states for a particular momentum. We also plot the linear spin wave data, which appear beneath the actual spectra. Dots are results of calculations, and the line connects them. If we follow the lowest lying crosses at each momentum, we notice that these crosses form a spectrum whose shape resembles that of the linear spin wave theory. These crosses correspond to the triplet states $S = 1$. All the above features are observed in the 1D case.

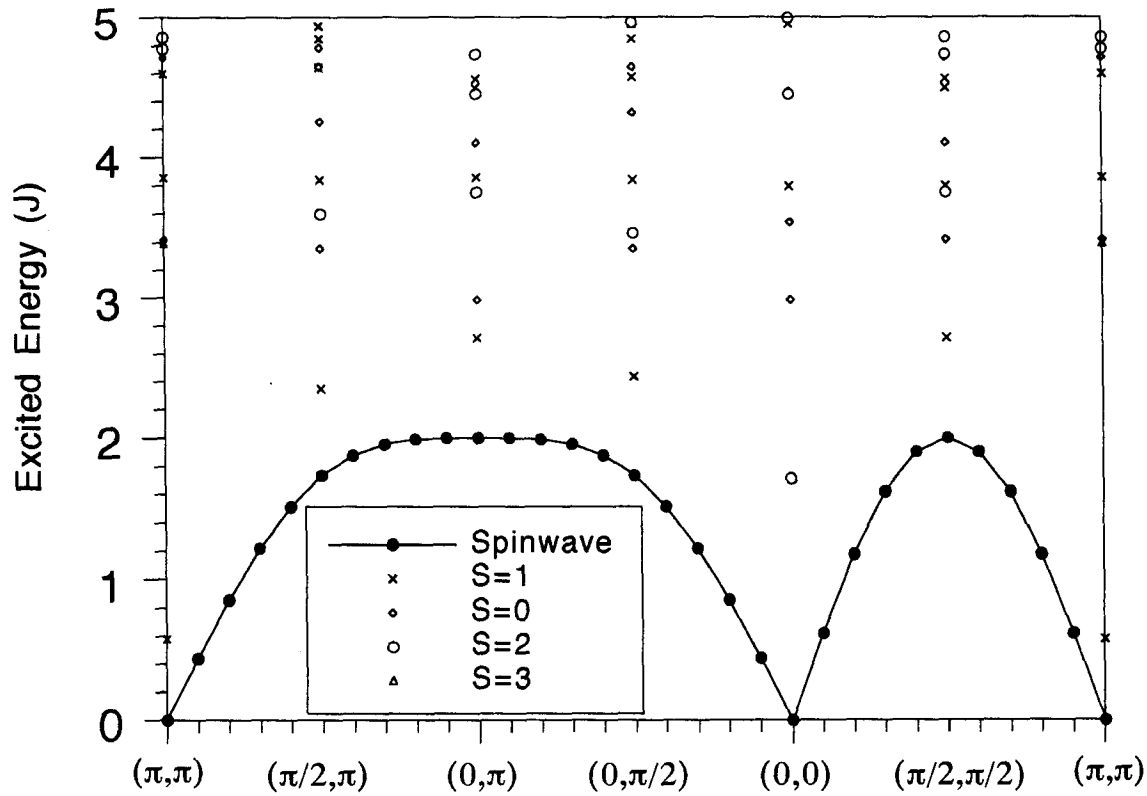

Fig. (1), energy spectra of spin-1/2 Heisenberg antiferromagnet on 4× 4 square lattice

In Fig. (2) we plot dynamic structure factors at various momenta. Energy ranges from 0.0 to 5.0 J. Each curve in Fig. (2) corresponds to the dynamic structure factor of a certain momentum and has two distinguished peaks. The intensity of the first peak at lower energy is much larger than that of the second peak, which is at higher energy. Comparing Fig. (1) and Fig. (2), we find that the first peak in each curve of Fig. (2) corresponds exactly to the lowest energy state of the particular momentum in Fig. (1). This fact at once proves that magnon or spin wave correspond to the lowest lying spin triplets, Fig. (1). The smaller second peak in each spectrum of dynamic structure factor corresponds also to another spin triplet of the particular momentum. The magnitude of the second peak is so small that it is not observed in neutron scattering experiments.

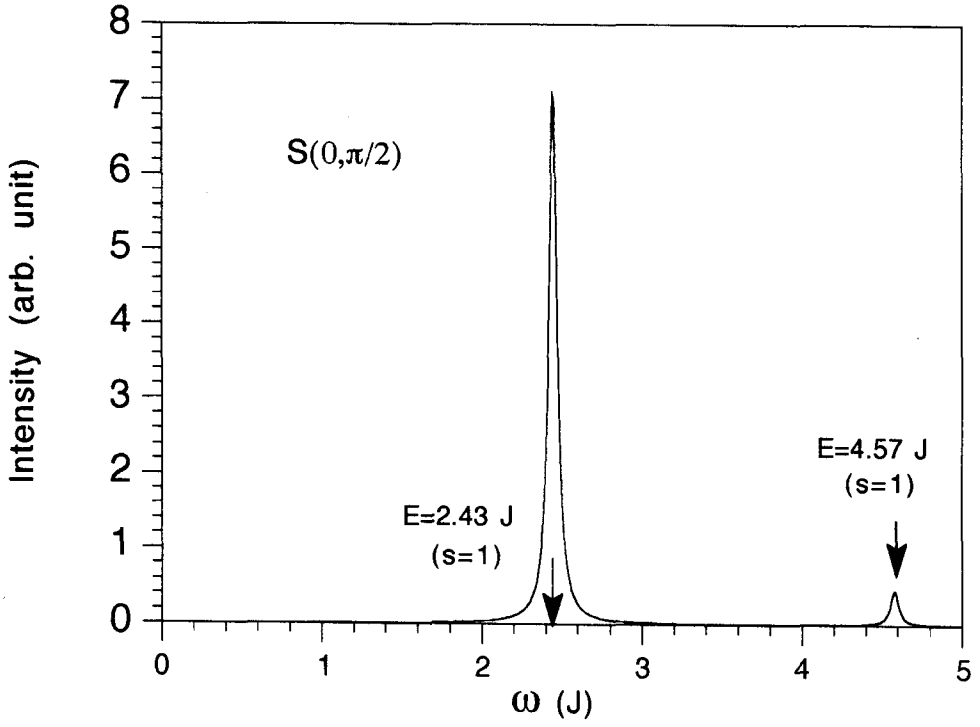

Fig. (2a), the dynamic structure factor at $\mathbf{k} = (0,\pi/2)$; arrows correspond to the energies of two spin triplet excited states.

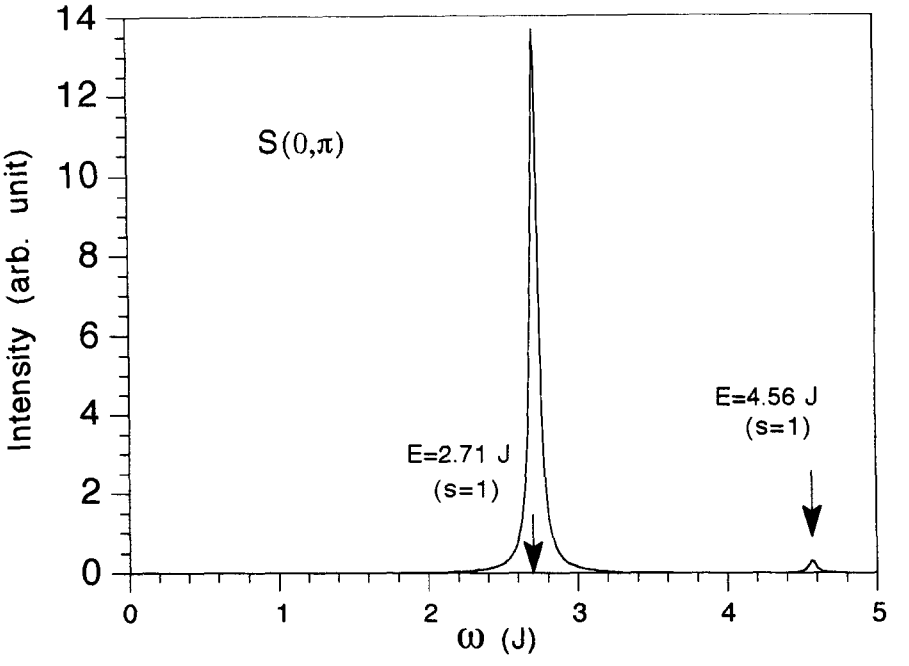

Fig. (2b), the dynamic structure factor at $\mathbf{k} = (0,\pi/2)$

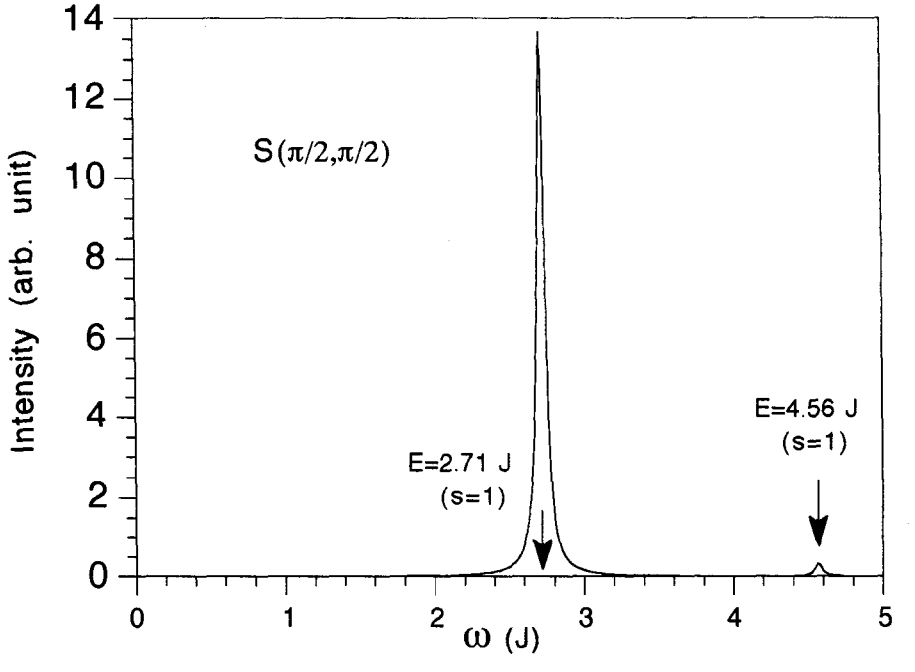

Fig. (2c), the dynamic structure factor at $\mathbf{k} = (0,\pi/2)$

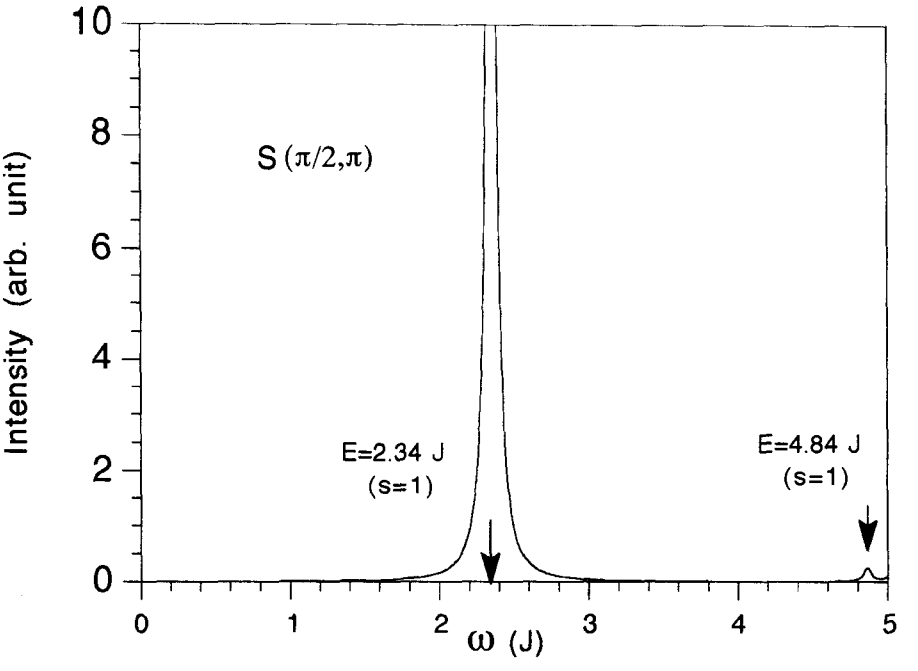

Fig. (2d), the dynamic structure factor at $\mathbf{k} = (0,\pi/2)$

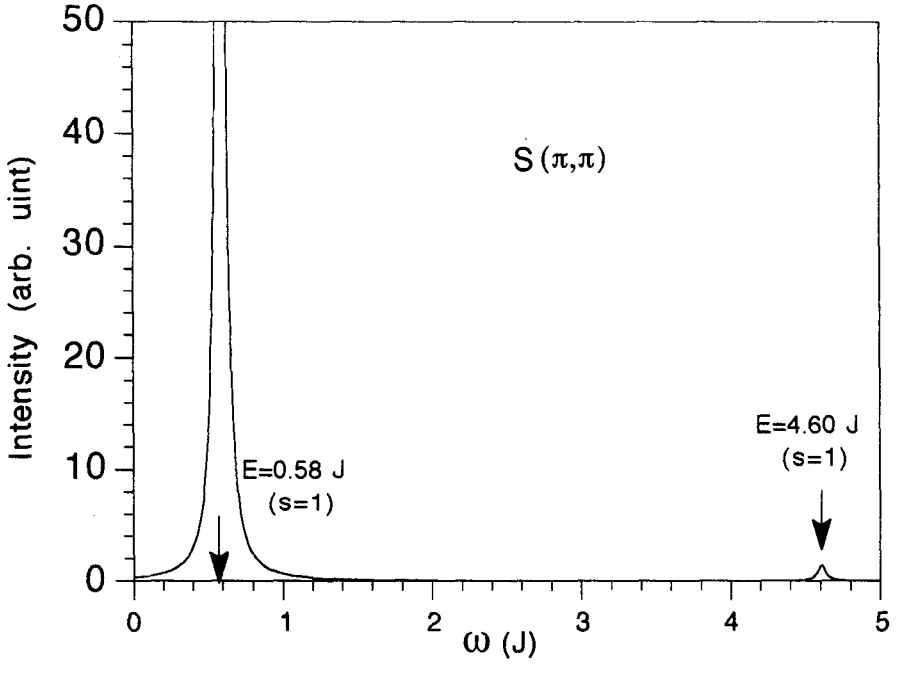

Fig. (2e), the dynamic structure factor at $\mathbf{k} = (0,\pi/2)$

1.2.5 Discussion and Conclusion:

This is the first report of the full energy vs. momentum spectra for the 4 × 4 spin-1/2 Heisenberg model, using an exact diagonalization technique. The precise fit between the energy spectra and the dynamical structure factor shows that the magnon or spin wave corresponds to the lowest lying triplet states for each **k**. It is observed that the spectra are "belt-like", with magnons locating at the bottom of the spectra, and the shape of spectrum calculated by the linear spin wave theory is similar to that of the exact magnon of 4 × 4 lattice. These characters are observed for 1D Heisenberg model[30]. And for 1D Heisenberg model, the magnon spectrum[30] of an infinite chain is

$$\omega_{\mathbf{k}} = \frac{1}{2}\pi|\sin k|, \tag{16}$$

while the linear spin wave theory gives

$$\omega_{\mathbf{k}}^{\mathrm{sw}} = |\sin k|. \tag{17}$$

The exact 1D magnon spectrum is equal to the value of the linear spin wave spectrum multiplied by an overall factor of $\pi/2$. The results of our study on 4×4 lattice suggest that for the 2D Heisenberg model of infinite square lattice, the magnon spectrum may be obtained by scaling the $\omega_{\mathbf{k}}^{\mathrm{sw}}$ of the linear spin wave theory, just as it was for the one-dimension case.

The 4 × 4 lattice is sufficiently large that the magnon properties inferred from our study should be qualitatively correct. Therefore, the above conclusions may also apply to the infinitely large lattice. It would, of course, be desirable to extend the study to larger systems, because it will show how the size of the lattice affects the results. The diagonalization method is not practical for 6 × 6 or larger

systems because of the limitation of the current computers' memory. Only Monte Carlo calculation can be performed on the larger systems. We have finished some Monte Carlo studies which indicate the above conclusions to be correct for the larger lattices[16]. The results will be presented in the next section.

1.3

Elementary Excitation of the Two-Dimensional Quantum Heisenberg Antiferromagnet

Guanhua Chen, Hong-Qiang Ding, and William A. Goddard III

Materials Simulation Center, Beckman Institute

California Institute of Technology, Pasadena, CA 91125

Abstract

The excitation spectrum of the antiferromagnetic spin-half Heisenberg Hamiltonian $H = \Sigma J\hat{S}_i \cdot \hat{S}_j$ on $L \times L$ lattices is evaluated by a Projector Quantum Monte Carlo method. These results suggest that the exact spectrum for the infinite lattice is $\omega_k \simeq Z(L)\ \omega_k^{SW}$, for all $\mathbf{k}$, where $\omega_k^{SW} = 4JS\sqrt{1-\gamma_k^2}$ with $\gamma_k = (\cos k_x + \cos k_y)/2$ is from the linear spin wave theory. We find $Z(L) = Z_E + B/L^3$, leading to $Z_E = 1.21 \pm 0.03$ for $L = \infty$. Comparison with experiments on La_2CuO_4 is made.

1.3.1 Introduction

Largely because of its relevance for high-T_c superconductors[1], the 2-dimensional Heisenberg antiferromagnetic Hamiltonian

$$H = \sum_{\langle ij \rangle} J\hat{S}_i \cdot \hat{S}_j, \; J > 0 \tag{18}$$

has been extensively studied recently[15-27,34]. However, there remains considerable uncertainty about the excitation spectrum for Hamiltonian (18).

The most common approximation to Hamiltonian (18) is the linear spin wave theory[35] (SW), which for one dimension leads to

$$\omega_k^{SW,1D} = J|\sin(ka)| \tag{19}$$

and for two dimensions leads to

$$\omega_k^{SW} = 4JS\sqrt{1-\gamma_k^2} \tag{20a}$$

where

$$\gamma_k = [\cos(k_x a) + \cos(k_y a)]/2. \tag{20b}$$

For the one-dimensional (1D) case the exact spectrum is solved by using the Bethe ansatz,[30] giving

$$\omega_k^{1D} = Z_E^{1D}\omega_k^{SW,1D}, \tag{21}$$

where

$$Z_E^{1D} = \frac{\pi}{2} = 1.57.$$

Thus the spin wave theory leads to results low by 36%, but the *shape* of the spectrum is exactly correct. Unfortunately for 2D and higher, there has been no general solution of Hamiltonian (18).

In this paper we calculate numerically the exact spectrum for 2D periodic $L \times L$ lattices ($L = 4, 6, 8, 12$). Extrapolated to $L = \infty$ these results lead to

$$\omega_{\mathbf{k}} \simeq Z_E \omega_{\mathbf{k}}^{SW} = Z_E \left[4JS\sqrt{1-\gamma_{\mathbf{k}}^2} \right] \tag{22}$$

where $Z_E = 1.21 \pm 0.03$. Thus, for 2D the shape of the lowest excitation spectrum is also the same as for the linear spin wave theory, but the renormalization factor is 1.21 rather than 1.57.

1.3.2 Method

To calculate the eigenstates of Hamiltonian (18), we use the Projector Monte Carlo (PMC)[17,36] method for finite $L \times L$ lattices and extrapolate to $L = \infty$. The basic idea in PMC is to start with trial functions ϕ, ψ (not orthogonal to the ground state) and to apply the *projector* $\exp(-\tau H)$ on ϕ for a sufficient time τ such that the wavefunction $\exp(-\tau H)\phi$ is a good approximation to the ground state wavefunction. The ground state energy is then computed as

$$E(0) = \langle \psi | H e^{-\tau H} | \phi \rangle / \langle \psi | e^{-\tau H} | \phi \rangle, \tag{23a}$$

and the excitation energy is computed as

$$E(\mathbf{k}) = \frac{\langle \psi | R(-\mathbf{k}) H e^{-\tau H} R(\mathbf{k}) | \phi \rangle}{\langle \psi | R(-\mathbf{k}) e^{-\tau H} R(\mathbf{k}) | \phi \rangle}, \tag{23b}$$

where the $R(\mathbf{k})$ operator projects out the states with definite momentum $\mathbf{k}$ from a mixed wavefunction. Takahashi has used such a momentum operator in 1D.[17] Here we extend it to the 2D case:

$$R(\mathbf{k}) = \sum_{\mathbf{r}} (\hat{S}_{\mathbf{r}}^z - S) e^{i\mathbf{k}\cdot\mathbf{r}}, \tag{24}$$

where $\hat{S}_r^z$ is the spin-1/2 operator at site $\mathbf{r} = (r_x, r_y)$, and the sum is over the L^2 sites in the periodic lattice.

A. Phase Convention

The Hamiltonian (18) has non-negative off-diagonal matrix elements, making PMC inapplicable. Thus, we make a unitary transformation[22,17]

$$U = \exp(i\pi \sum_r \hat{S}_r^z), \tag{25}$$

where the sum is over alternate sites. This flips the x,y components of spins on alternative sites,

$$UHU^{-1} = J \sum_{<ij>} (-S_i^x S_j^x - S_i^y S_j^y + S_i^z S_j^z), \tag{26}$$

(i.e., the x,y terms change signs). Consequently, all off-diagonal elements become non-positive and PMC is applicable. This does not change any observables, but the momenta of wavefunctions are shifted by

$$UT_x U^{-1} = e^{i\pi(L^2 S - M_z)} T_x, \tag{27a}$$

$$UT_y U^{-1} = e^{i\pi(L^2 S - M_z)} T_y, \tag{27b}$$

where $M_z = \sum_i S_i^z$ is a conserved quantity and S=1/2. Since L is even numbers in our calculation and the lowest state is in $M_z = 0$ subspace, there is no momentum shift. In two dimensions, all $L \times L$ (L even) antiferromagnetic system have $\mathbf{k} =$ (0,0) as the ground states.

B. Partitioning of the Hamiltonian

The trial wavefunction ϕ is the sum

$$|\phi\rangle = \sum_{m=1}^{C} w_m |m\rangle, \tag{28}$$

where the spin state $|m\rangle$ is a product of L^2 one-spin eigenstates of $\hat{S}_i^z$ for an $L \times L$ system and where $C \sim 10^6$ is the number of walkers which jump from one state to another in the calculation. The total number of spin states for the $L \times L$ system (with $M_z = 0$) is the binomial coefficient

$$C_{max} = \binom{L^2}{\frac{1}{2}L^2} \simeq \sqrt{\frac{2}{\pi}} \frac{1}{L} e^{L^2}. \tag{29}$$

(for $L = 8$ this is 2×10^{18}). Thus, C is much smaller than C_{max}. Applying the projector, the ground state wavefunction is approximated by

$$e^{-\tau H}|\phi> = \sum_m w_m(\tau)|m(\tau)> . \tag{30}$$

As the computation evolves from τ_n to τ_{n+1}, each walker m evolves from spins state $|m(\tau_n)\rangle$ to spin state $|m(\tau_{n+1})\rangle$, according to the propagator $e^{-\Delta\tau H}$.

A problem here is that the $2L^2$ terms in the Hamiltonian do not commute. To simplify the calculations, we decompose H into four sub-Hamiltonians[22]

$$H = H_1 + H_2 + H_3 + H_4, \tag{31a}$$

where each H_s has $L^2/2$ terms that commute among themselves (see Fig.1):

$$H_1/J = \hat{S}_{11} \cdot \hat{S}_{21} + \hat{S}_{12} \cdot \hat{S}_{22} + \cdots, \tag{31b}$$

$$H_2/J = \hat{S}_{21} \cdot \hat{S}_{31} + \hat{S}_{22} \cdot \hat{S}_{32} + \cdots. \tag{31c}$$

Using (10), we can write $e^{-\Delta\tau H}$ as

$$\begin{aligned} & e^{-\Delta\tau(H_1+H_2+H_3+H_4)} \\ & = e^{-\delta_4 H_1} e^{-\delta_2 H_2} e^{-\delta_4 H_1} e^{-\delta_4 H_3} e^{-\delta_2 H_4} e^{-\delta_4 H_3} \\ & \cdot e^{-\delta_4 H_4} e^{-\delta_2 H_3} e^{-\delta_4 H_4} e^{-\delta_4 H_2} e^{-\delta_2 H_1} e^{-\delta_4 H_2} + O(\Delta\tau)^3, \end{aligned} \tag{32}$$

where $\delta_2 = \Delta\tau/2$, $\delta_4 = \Delta\tau/4$. Because the $L^2/2$ terms in each H_s commute among themselves, the propagator $e^{-\delta H_s}$ factors into a product of $L^2/2$ 2-spin *transfer matrices*, each of which can be further decomposed into a product of two matrices[17,36],

$$\langle S^z_{i,\tau_n} S^z_{j,\tau_n} | e^{-\delta S_i \cdot S_j} | S^z_{i,\tau_{n+1}} S^z_{j,\tau_{n+1}} \rangle = p_{\alpha\beta} q_\beta . \tag{33a}$$

where $\sum_\alpha p_{\alpha\beta} = 1$. The transition matrix **p** changes the 2-spin state from β to α with probability $p_{\alpha\beta}$. The diagonal matrix q contributes to the weight multiplicatively,

$$w_i(\tau_{n+1}) = \left(\prod_{j=1}^{12} \prod_{\beta=1}^{\frac{1}{2}L^2} q_\beta \right) w_i(\tau_n), \tag{33b}$$

where j is over the 12 factors in Eq. (32).

B. Redistribution

One application of $e^{-\Delta\tau H}$ contributes $6L^2$ factors to each weight [cf. Eq.(33b)]. Successive applications of $e^{-\Delta\tau H}$ thus leads to large increases in some w_m and large decreases in others, resulting in orders of magnitude differences in w_m for different walkers. As a result, the wavefunction ϕ_τ becomes quickly dominated by a few walkers having very large weights, leading to an effective reduction of the sampling space. To solve this problem we periodically *redistribute* the weights to obtain a new set of C walkers equivalent to the existing set but with equal weight[17,37]. In this way, walkers with very small weights are eliminated and those with large weights multiply in number. For the 8×8 lattice, we find it necessary to redistribute about every two applications of $e^{-\Delta\tau H}$.

C. Contraction

A second issue is the choice of the *contraction* function ψ in Eq. (23). One common choice[16] is setting $\psi = \phi$. However, we find that it is important to use the

all states function

$$|\psi\rangle_{\text{all}} = \sum_{\text{all states}} |\text{m}\rangle. \tag{34}$$

The reason is that $\langle \text{m}_1|\text{H}|\text{m}_2\rangle$ is very sparse. Using $\psi = \phi$ would lead to very few nonzero off-diagonal contributions, resulting in large fluctuations in energies. The *all states* function of Eq. (34) guarantees that each term of ϕ will makes nonzero off-diagonal contributions. In addition, since ψ has the same coefficient for all possible states, we need not store ψ, nor do we need to search ψ for the corresponding spin state, once $\text{H}|\text{m}\rangle$ is generated.

Another significant advantage of the *all states* choice is that with ψ independent of ϕ, we can *coherently* add the contributions from independent runs

$$\frac{\langle\psi|\text{H}|\phi_1+\phi_2\rangle}{\langle\psi|\phi_1+\phi_2\rangle} = \frac{\langle\psi|\text{H}|\phi_1\rangle + \langle\psi|\text{H}|\phi_2\rangle}{\langle\psi|\phi_1\rangle + \langle\psi|\phi_2\rangle}. \tag{35}$$

Typically, we do 500 such independent runs. Thus, from each run ϕ_i we need only accumulate the two numbers $\langle\psi|\text{H}|\phi_\text{i}\rangle$ and $\langle\psi|\phi_\text{i}\rangle$ from different runs until sufficient accuracy is obtained. With the other choice of $\psi = \phi$ the coherent average would require evaluation of cross terms $\langle\phi_1|\text{H}|\phi_2\rangle$, $\langle\phi_1|\phi_2\rangle$; this would require storing 500 wavefunctions, each with 50,000 terms and would require evaluating 50000^2 matrix elements.

D. Procedure

The calculation of E_0 and $\text{E}(\mathbf{k})$ is done simultaneously for all values of $\mathbf{k}$. We start with an initial function ϕ randomly chosen and propagate it according to Eq. (30,32,33) to approximate the ground state wavefunction ϕ_0. We allow this relaxation of the initial ϕ for 100 time steps ($\tau_0 = 100\Delta\tau$), during which the redistribution is applied every 5 time steps (for 8×8 lattice).

Next, we apply the following process of $\tau_1 + \tau_2$ steps many times until convergence is reached. During the τ_1 process ($\approx 50\Delta\tau$ steps), the function ϕ_0 is relaxed with a more frequent redistribution of every two steps. At the beginning of the next τ_2 process ($\approx 20\Delta\tau$ steps), we compute the phase factors $R(\mathbf{k}, m) = \langle m(\tau')|R(\mathbf{k})|m(\tau')\rangle$. $R(\mathbf{k}, m)$ remains associated with the mth walker, although the walker may well possibly walk into different spin states $|m(\tau)\rangle$. With each set of the phase factors $\{R(\mathbf{k}, m), m = 1, \cdots, C\}$ for a momentum $\mathbf{k}$, the corresponding wavefunction is constructed as

$$\phi(\mathbf{k}) \equiv e^{-\tau H} R(\mathbf{k})|\phi\rangle = \sum_m w_m(\tau) R(k, m)|m(\tau)\rangle \tag{36}$$

and $E(\mathbf{k})$ is evaluated every two steps (This is very similar to the *forward-walking* in the Green Function Monte Carlo method[38]). At the end of the τ_2-process, we take the current wavefunction as the starting wavefunction of the next $\tau_1 + \tau_2$ process. We found that τ_2 cannot be too large because ϕ_0 is not the exact ground state wavefunction at the beginning of the τ_2 process when $R(\mathbf{k},m)$ is calculated. The τ_1 process separates the τ_2 process so that the consecutive measurements of E_0, $E(\mathbf{k})$ are less correlated.

We calculated the excited states for L = 4, 6, and 8, using C = 4000, 64000, and 128000, respectively. In each case, the ϕ was chosen to have a total spin projection component (M_z) of zero. We found that $\Delta\tau$ =0.1 leads to accurate results (e.g., tests on L = 4 and 6 using $\Delta\tau$ = 0.05 led to energies differing by less than 0.5%). In all cases the coherent averages were carried out on the $\tau_1 + \tau_2$ process for 500 repetitions. As a test, we computed the spectrum on a 4×4 lattice and compared with the exact results from direct diagonalization[15] in Table 2. The agreement is excellent.

We found that the ground state energy converges quickly, leading to accurate results up to L = 12. [This is a singlet spin state ($\hat{S}^2\Psi = 0$) for the L^2 spin system.] The excited states energies are much more difficult to calculate for large lattices, and the excited state spectrum for $L \geq 10$ did not converge well. [In each case the excited state is a triplet spin state, $\hat{S}^2\Psi = 2\Psi$.] Probably the large configuration space ($\sim 10^{42}$ for L = 12) requires a substantially larger number of walkers or a larger number of runs in the coherent average. Another difficulty in obtaining the spectrum $\omega_k = E(k) - E_0$ is the subtraction of two large numbers. Both E(k) and E_0 are extensive quantities proportional to the area of the system L^2, whereas their difference remains a constant (very weakly dependent on the sizes). For an 8×8 lattice, $E_0 = -43.03 \pm 0.05J$, while ω_k is about 1J. Consequently to obtain an accuracy of a 5% error in ω_k requires an accuracy of 0.1% error in E(k) and E_0. Considering the Monte Carlo nature of our method, this is a rather stringent requirement. The coherent addition mentioned above is critical to obtain reasonably accurate results.

The program was developed on a parallel supercomputer, the 64-node Caltech/JPL MarkIIIfp Hypercube.[39] Each node contains a fixed number (C/64) of spin states. Application of $e^{-\Delta\tau H}$ is carried out locally on each node. However, redistribution must be done globally because the weights on one processor will influence the redistribution of walkers on other processors. We have devised an efficient algorithm for this redistribution, which for C = 64000 takes only 15% of the total time. For C = 64000, the total time for one $\Delta\tau$ step in the 64 node hypercube is 4 sec. In comparison, the same code (written in "C") running on a 1 processor CRAY XMP (at JPL) is 20 sec. Thus, the hypercube is about 5 times faster.

1.3.3 Results and Analysis

The calculated ground state energy density (energy per atom), $E(0,L)/L^2$, is shown in Fig. (3a) for L = 4 to 12. We find that $E(0,L)/L^2$ is very accurately fitted by

$$E(0,L)/L^2 = e_0 + B/L^3, \tag{37a}$$

as indicated in Fig. (3a). This fit ($B = -2.17 \pm 0.04$) gives the ground state energy per site of the infinite system,

$$e_0 = -0.668 \pm 0.001J, \tag{37b}$$

in good agreement with other calculations. The Green Function MC results[19,20] are $e_0 = -0.6692(2)$, and the World-line MC results are $e_0 = -0.670(1)$[18], $-0.6661(2)$[21], $-0.6693(2)$[23]. (See Ref. [34] for a more complete review.)

The point $\mathbf{ka} = (\pi,\pi)$ is of special interest. This state is a spin triplet state, whereas the ground state (0,0) is a spin singlet. In the spin wave theory the (π,π) and (0,0) states are degenerate. Similarly in 1-D the state $\mathbf{ka} = \pi$ is degenerate with $\mathbf{k} = 0$ for both the spin wave theory and the exact energy. However for finite L, $\mathbf{k} = (\pi,\pi)$ has an energy higher than $\mathbf{k} = (0,0)$ by

$$\Delta = E(\pi,\pi) - E_0 > 0. \tag{38}$$

This gap decreases with L, and we find that the gap goes to zero[20,21,40] as

$$\Delta \approx \frac{A}{L^2}, \tag{39}$$

where A = 9.26 (see Fig. (3b)). The triplet state (π,π) is difficult to calculate directly in the $M_z = 0$ subspace. we instead obtain $E(\pi,\pi)$ as the lowest energy for in the $M_z = 1$ subspace.

Our goal is to obtain an analytical expression of the spectrum for ω_k for the infinite lattice. In principle, for each fixed (k_x, k_y) one could compute ω_k on a series of lattices and then extrapolate to the infinite lattice. However, this is difficult to implement because each L × L lattice leads to a different set of discrete momenta (k_x, k_y) with few in common. Here, we use the alternative approach of finding an analytical expression which fits the data for each finite lattice and then extrapolating the fitting parameter to the infinite lattice.

As discussed in the introduction, for 1D the linear spin wave spectrum has the same analytical form as the exact spectrum except for a scaling or renormalization constant, $Z_E^{1D} = 1.57$. Motivated by this result, we factor the finite size dependence for the 2D system into the form

$$\omega_k^{2D}(L) = Z(L,k)\left[4JS\sqrt{1-\gamma_k^2+A_k^2/L^4}\right], \tag{40a}$$

where $Z(L,k) = 1$ and $A_k = 0$ would lead to the ω_k^{SW} of Eq.(3a). Here the term A_k^2/L^4 accounts for the finite size effects[40] which break the symmetry of $1-\gamma_k^2$ between (0,0) and (π,π), and thus generates the gap. A_k changes smoothly with $\mathbf{k}$, and the exact form is not important as shown below. At $\mathbf{k} = (\pi,\pi)$, this form leads to a gap for that scales as $1/L^2$. For all other momenta, except (0,0), of course, the A_k^2/L^4 term is very small compared to $1-\gamma_k^2$ so that this correction can be neglected. [Even in the most extreme case of $\mathbf{k} \to 0$, $1-\gamma_k^2 \simeq (k_x^2+k_y^2)/2 = 2\pi^2(n_x^2+n_y^2)/L^2$, where $n_x, n_y \ll L$ are integers. This is still much larger than A_k^2/L^4.]

The above analysis also suggests that $Z(L,k)$ has little dependence on k, i.e., $Z(L,k) \approx Z(L)$. Thus, we have

$$\omega_k^{2D} \approx Z(L)4JS\sqrt{1-\gamma_k^2} = Z(L)\omega_k^{SW,2D}. \tag{40b}$$

Indeed, using the only parameter Z(L) for a given L × L lattice , one can fit the obtained $\omega(\mathbf{k})$ to Eq.(40) for all $\mathbf{k}$. as shown in Fig. (4). Plotted in units of 4JSZ(L), all data points on the three lattices (L = 4, 6, 8) collapse into a single curve [except at $\mathbf{k} = (\pi, \pi)$ due to the gap term $A_{\mathbf{k}}^2/L^4$], giving clear evidence that the exact spectrum has the same shape as the spin wave spectrum, $\sqrt{1-\gamma_{\mathbf{k}}^2}$. The fact that one parameter Z(L) fits all data points on each lattice confirms the usefulness of Eq. (40).

These data fits to theoretical form give $Z(L) = 1.38, 1.26 \pm 0.01, 1.22 \pm 0.02$ for L = 4, 6, 8 respectively. [For 4 × 4 we used the exact spectrum at $(\frac{\pi}{2}, 0)$ and $(\pi, 0)$ in the fit.] To estimate the limit for $L \to \infty$, we fit Z(L) to L^{-n} and find a size dependence of Z(L) as

$$Z_E(L) = Z_E + B/L^3, \tag{41}$$

as shown in Fig. (3c); the result is $Z_E = 1.21 \pm 0.03$, and $B = 11.1 \pm 0.8$. [Here we use Z_E to distinguish from Z_c, the renormalization of the spin wave form at $\mathbf{k} \to 0$ limit.]

To give some further understanding of the $1/L^3$ extrapolation found in our data fit, we examined $E(\mathbf{k}, L)$ within the framework of the Schwinger Boson Mean Field Theory.[25] This theory is an approach different from the spin wave theory, and it gives improved results on a number of aspects, such as the correlation length, uniform susceptibility etc. The theory leads to a spectrum very close to the spin wave result: For a L × L square lattice, the spectrum is given by

$$\omega_{\mathbf{k}}^{MF} = 2\Lambda(L)\sqrt{1-\eta^2(L)\gamma_{\mathbf{k}}^2}, \tag{42a}$$

where $\gamma_{\mathbf{k}}$ is given in (20b). The Λ and η are determined by minimizing the free

energy, leading to:

$$1 = \sum_{k} \frac{2}{L^2} |\gamma_k|^2 \omega_k^{-1} \coth\left(\frac{1}{2}\beta\omega_k\right), \tag{42b}$$

subject to the condition

$$\frac{1}{\Lambda(L)} = \sum_{k} \frac{1}{L^2} \omega_k^{-1} \coth\left(\frac{1}{2}\beta\omega_k\right), \tag{42c}$$

where $\beta = \frac{1}{T}$. Clearly, $\Lambda(L)$ is very similar to $Z(L)$ in Eq. (40), and we are interested in the size scaling of $\Lambda(L)$. For this purpose, we solved Eq. (42) for $L = 4$ to 24 at the $T \to 0$ limit. [We used $T = 0.02J$ and verified with $T = 0.01J$.] First, $\eta(L)$ is found to be very close to 1 (η increases from 0.993 for $L = 4$ to 0.9999 for $L = 16$ and becomes indistinguishable from 1 for larger lattices). Second, the $\Lambda(L)$ can be well fitted by

$$\Lambda(L) = \Lambda_\infty + D/L^3, \tag{43}$$

as shown in Fig. (3d). We find $\Lambda_\infty = 1.158 \pm 0.001$ and $D = 2.24 \pm 0.01$, in good agreement with the original calculation[25]. This is a theoretical justification to our empirical scaling.

1.3.4 Discussion

At the long wavelength, limit $\mathbf{k} \to 0$, the spin wave spectrum is simplified to

$$\omega_k^{SW} = \sqrt{8}JSka, \; k^2 = k_x^2 + k_y^2. \tag{44}$$

The linear coefficient, $\sqrt{8}JSa$, is the usual spin velocity. The correction to this linear coefficient, the spin velocity renormalization factor Z_c, has been calculated by a number of authors[21,19,26–28]. On the other hand, our results suggest an overall renormalization, Z_E, for all $\mathbf{k}$. Thus, $Z_E = Z_c$. Oguchi[28] obtained $Z_c = 1.16$ using

a 1/2S expansion of the higher order spin wave theory. Singh, *et al.*[26] obtained $Z_c = 1.18 \pm 0.02$, by a series expansion around the Ising limit. The Green Function MC simulation of Trevedi and Ceperly[19] gave an estimate $Z_c = 1.14 \pm 0.05$ from a variational method. Gross *et al.*[21] measured ground state energies of various size square lattices by a Projector Monte Carlo technique and compared them with those of spin wave theory, giving $Z_c \approx 1.18 \pm 0.10$. Our result $Z_E = 1.21 \pm 0.03$ is in reasonable agreement with these calculations.

The linear dispersion relation at small $\mathbf{k}$ has been observed in inelastic neutron scattering experiments[41]. For La_2CuO_4, the experiment gives a spin wave velocity of $hc_s = 0.85 \pm 0.03$ eVÅ. Using a lattice parameter of a = 3.80Å (determined by X-ray diffraction[42]) and an exchange coupling value of $J = 1450 \pm 30K = 0.125 \pm 0.003$ eV (obtained by fitting the Monte Carlo results[22] to the observed spin correlation length[42]), our result $Z_E = 1.21 \pm 0.03$ leads to $hc_s = Z_E\sqrt{8}JSa = 0.80 \pm 0.03$eVÅ, quite close to the experimental value. (Using $Z_c = 1.16$ leads to $hc_s = 0.77$eVÅ.) This indicates that the simple Heisenberg model well describes the magetic interactions in La_2CuO_4.

In conclusion, our numerical calculation of the excitation spectrum and finite size analysis suggests that the exact spectrum of the 2D Heisenberg Hamiltonian has the same form as the linear spin wave theory, except for an overall renormalization constant of $Z_E = 1.21 \pm 0.03$. This justifies the use of the spin wave spectrum for a wide variety of calculations, including the Schwinger boson mean field theory and the modified spin wave theory. Our numerical value on spin velocity agrees with both the previous calculations and the neutron scattering experiment.

Acknowledgements. The research was initiated with funding from the NSF-

DMR-MRG and completed with funding from NSF-CHE and from the MSC/BI. The facilities of the MSC/BI are also supported by grants from DOE-ECUT, NSF-DMR-MRG, NSF-CHE, BP America, Allied-Signal Corp., Asahi Chemical, Asahi Glass, Xerox Corp., Chevron Inc., and Beckman Institute. This is contribution #8568 from the Division of Chemistry and Chemical Engineering at Caltech.

note: After finishing the draft of this manuscript, I learnt that authors of Ref. [80] have performed a low temperature Monte Carlo simulation on 64 square lattice and have concluded that $Z_E = 1.18$[80].

Table 2. $E(k_x, k_y)/J$ for all momentum on the 4×4 lattice. The exact results are from Ref.4. The statistical uncertainties are indicated in parentheses.

k_x, k_y	Exact	PMC
0 , 0	−11.2285	−11.228(11)
0 , $\frac{\pi}{2}$	−8.7944	−8.749(12)
0 , π	−8.5183	−8.510(20)
$\frac{\pi}{2}$, $\frac{\pi}{2}$	−8.5183	−8.506(17)
$\frac{\pi}{2}$, π	−8.8864	−8.909(17)
π , π	−10.6499	−10.63(4)

Figure Captions

Fig.(3) Size dependencies of various quantities: (a) the ground state energy (units of J), the line is $e_0 + B/L^3$ fit; (b) the energy gap, $\omega(\pi,\pi) = E_{\pi\pi} - E_0$, the line is $\omega(\pi,\pi) = A/L^2$ (c) the spectrum renormalization factor Z(L) ; (d) Λ(L) from SBMFT.

Fig.(4) Comparison of results from PMC calculations for L $\times$ L lattices with L = $4, 6, 8$ to the spin wave spectrum (see Eq.(18)). In each case, the results have been scaled as $\omega(\mathbf{k})/8JSZ(L)$, with Z(4) = 1.38, Z(6) = 1.26, Z(8) = 1.22, which are obtained by fitting the spectrum in the branch $\mathbf{k} = (0,0)$ to $\mathbf{k} = (0,\pi)$. Except for the gap at $\mathbf{k} = (\pi,\pi)$, all other data points fall along the curve, $\sqrt{1-\gamma_{\mathbf{k}}^2}$.

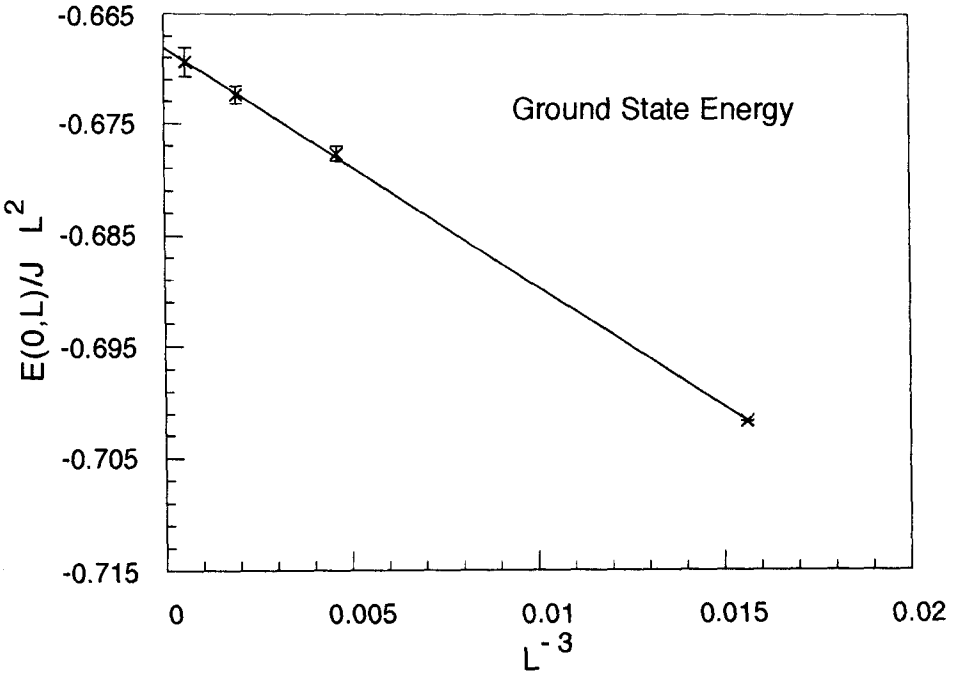
Ground State Energy
E(0,L)/J L 2
-0.665
-0.675
-0.685
-0.695
-0.705
-0.715
0
0.005
0.01
0.015
0.02
L - 3

Fig. (3a)

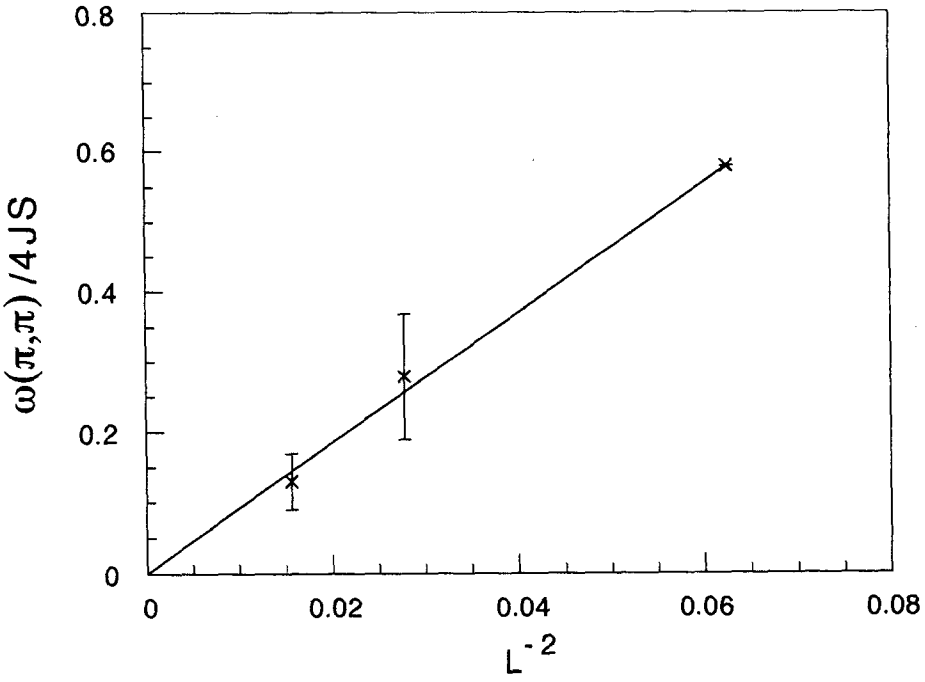
ω(π,π) /4JS
0.8
0.6
0.4
0.2
0
0
0.02
0.04
0.06
0.08
L - 2

Fig. (3b)

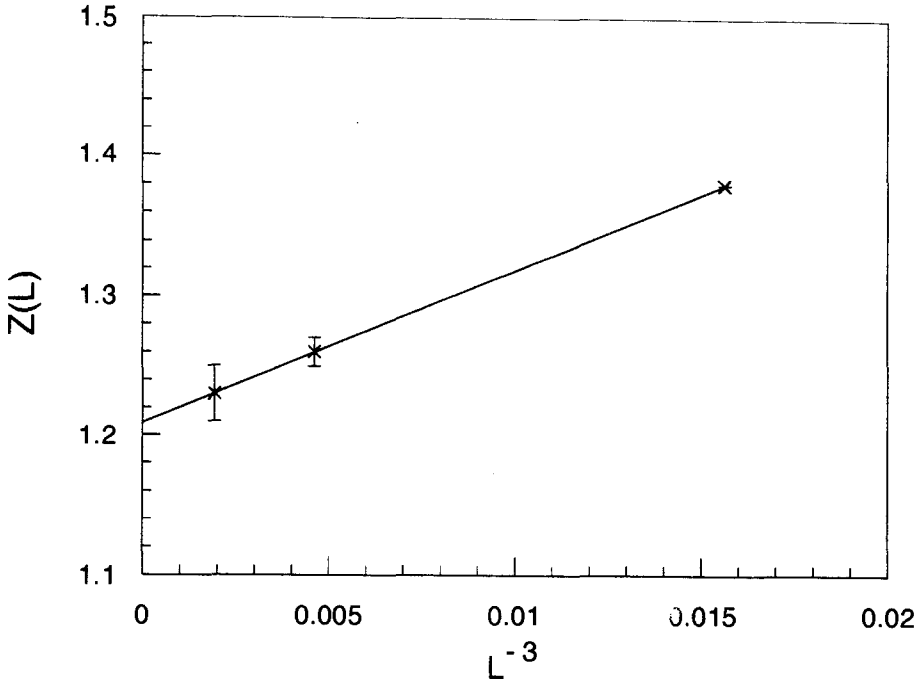
1.5
1.4
1.3
1.2
1.1
Z(L)
0
0.005
0.01
0.015
0.02
L^-3

Fig. (3c)

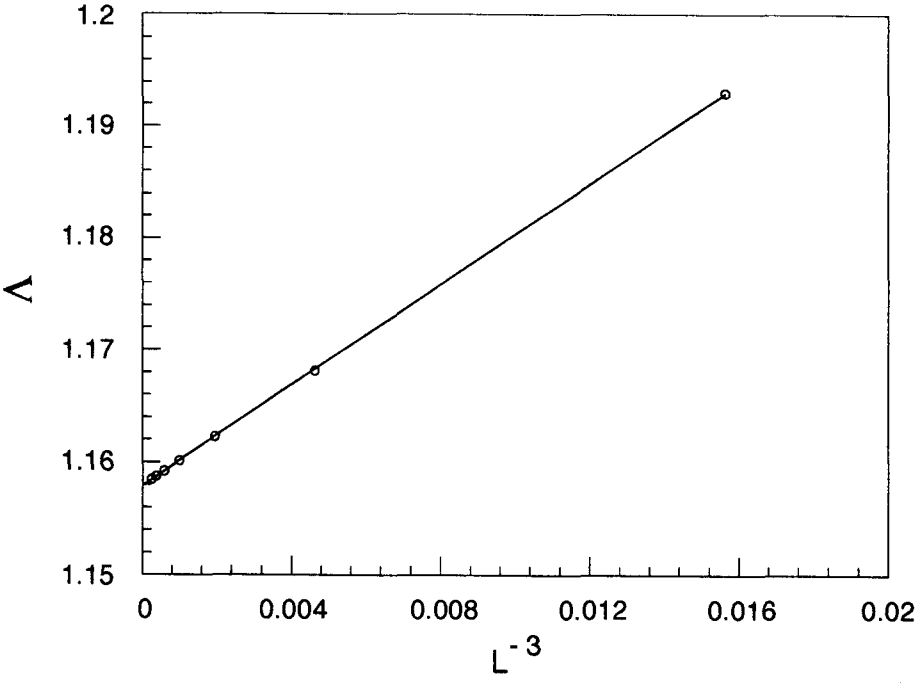
1.2
1.19
1.18
1.17
1.16
1.15
Λ
0
0.004
0.008
0.012
0.016
0.02
L^-3

Fig. (3d)

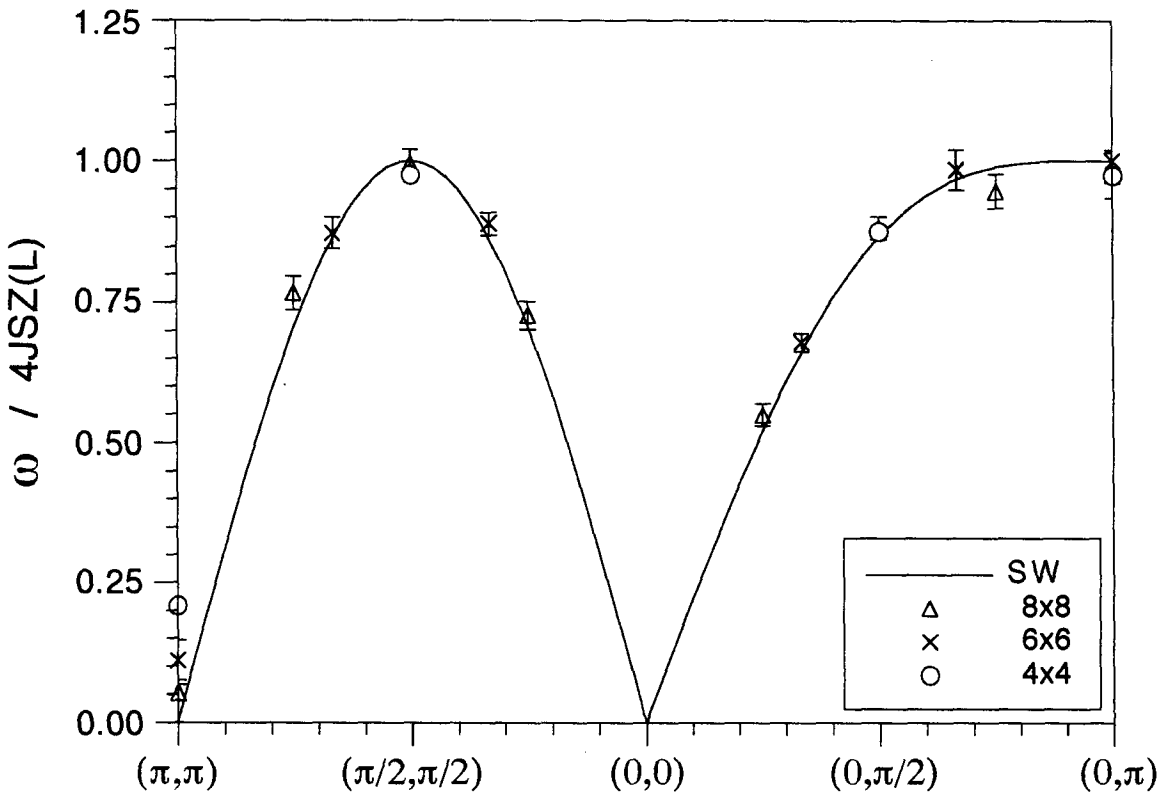

Fig. (4)

1.4 Review of some Microscopic Properties Related to High-T_c Superconductors

The investigation of high-T_c superconductors is at an interesting stage. Much progress has been made in the field, mainly as a result of improved sample quality , and in particular, the availability of single crystals[43]. By now a reasonable amount of agreed experimental data reveals a great deal of information and places quite severe constraints on the character of the normal state and the mechanism of superconductivity. Here we will review some experiments which are central to the understanding of the superconducting mechanism of high-T_c materials. Based on those experiments we will try to establish some general microscopic pictures of the normal and superconducting phases of these cuprate compounds.

1.4.1 Normal State

One major question in the field is: "Is the fermi liquid description valid for the current carriers in high T_c systems ?" Photoemission experiments on Bi2212[11,12], $YBa_2Cu_3O_{6.9}$[44] and $Nd_{2-x}Ce_xO_{4-y}$ [45] clearly demonstrate the fermi edge in photoelectron spectroscopy. Resonant photoemission experiments on Bi2212 [11] and $Nd_{2-x}Ce_xO_{4-y}$ [45] show that photoemission intensity, and hence the density of states within 0.5ev fermi level exhibits a strong enhancement at the O 2s core threshold; a much less enhancement is observed at the Cu 3p threshold, indicating that the electronic states at the Fermi level have a dominant O 2p nature. Further Angle-resolved photoemission is capable of mapping electronic spectra. Experiments on Bi2212 [12] and $YBa_2Cu_3O_{6.9}$[44] have identified the fermi surfaces in the Brillouin zone, which agree with local density calculations[46,47]. Electronic band structure has been measured successfully along major symmetry lines on $Bi_2Sr_2CaCu_2O_8$, and an

effective mass of a factor ~ 2 has been obtained[45]. On $YBa_2Cu_3O_7$, measured angular correlation of annihilation radiation (ACAR) from positrons annihilating with electrons[48] obtains similar results.

The temperature dependence of nuclear spin relaxation rates for O and Y in $YBa_2Cu_3O_7$ follows a Korringa law[49,50] (K^2T_1T = const., K is the NMR shift, T_1 is the relaxation time and T is the temperature), which is characteristic of a fermi liquid. Further, the Knight shifts[49,50] of both Cu and O in the planes are proportional to the static susceptibility $\chi(\omega = 0, q = 0)$, strongly supporting the notion that the spins on the $Cu - 3d$ and $O - 2p$ state are closely connected and are part of the same single component system, which indicates that O 2p has $2p\sigma$ character.

Above observations are all consistent with a conventional fermi liquid picture. However, angle-resolved photoemission study[45] of $Bi_2Sr_2CaCu_2O_8$ reveals that the photohole linewidth increases rapidly as the band moves below the fermi level. They are best fitted by a linear dependence on energy away from the fermi energy, showing $\propto |E - E_f|$, instead of $\propto |E - E_f|^2$ as the conventional fermi liquid[51]. Som people attribute this behavior to the interaction between current carriers of the narrow bands and spin fluactuations[77]

To conclude, quasiparticles in these cuprate superconductors are fermion and are of Cu 3d and O $2p\sigma$ hole character. They exhibit a combination of "ordinary" behavior, such as a single-particle fermi surface and modest mass enhancement, and the "unusual" behavior, for instance, linewidth broadening is linear in energy.

1.4.2 Magnetic Properties

The parent compounds of the cuprate superconductors are magnetic in-

sulators. They are well described as spin-$\frac{1}{2}$ square Heisenberg systems with a strong antiferromagnetic coupling, given by exchange parameters J ranging from $\sim 100 - 130\text{meV}$[2,43]. A tiny interplanar coupling leads to 3D ordering at temperatures T_N of order 100°K. Extensive neutron scattering[14,52] and NMR[53] experiments as well as theoretical works[14] have established this. A recent experiment conducted by substituting additional layers between CuO_2 bilayers found that the 3D transition temperature is determined only by the characters of CuO_2 planes[55].

Doping away from the parent compounds, i.e., adding holes to CuO_2 sheets, 3D antiferromagnetic order begins to disappear. For simplicity, we concentrate on single crystal $YBa_2Cu_3O_{6+x}$ [54]. According to Ref. [54], (i) at x = 0, O on the chain is missing, there are no extra holes on CuO_2 sheets, and therefore an antiferromagnetic magnetic order exists at low temperatures; Cu on the chain is d^{10}, i.e. Cu^+. (ii) For $0 < x < 0.2$, the AF ordering in $YBa_2Cu_3O_6$[56,57] basically remains the same[54]. The low temperature ordered moment $m_0 = 0.64\mu_B$ and the ordering temperature $T_N = 415°K$ are unchanged. This indicates that as the oxygens dope onto CuO chain charge transfers take place solely within the chain and Cu^+ on the chain becomes Cu^{2+}. ^{63}Cu ZFNMR[49] has confirmed this. (iii) For $0.20 < x < 0.40$, T_N and m_0 decrease[54]. The decrease becomes abrupt beyond x = 0.35 and the 3D-AF order disappears around $x_c \approx 0.41$[54]. This is because that around $x \approx 0.20$ holes begin to transfer from CuO chains to CuO_2 sheets[58]. These holes distort the local magnetic moments and are localized. At low temperature the observed reentrant behavior is attributed to the localization of these holes. At high temperatures the motion of quasi-particles (holes and polarons) induces additional spin fluctuations, which reduce T_N[54]. (iv) At $x_c = 0.41$, holes' activation energy vanishes, an

insulating-metal transition occurs and the critical hole concentration is estimated[54] to be $n_c^h \approx 2\%$. (v) For $x_c > 0.41$, the 3D-AF ordering disappears due to a sudden transfer of a large amount of holes $(10 - 15\%)$ in CuO_2 planes, which leads to a superconducting phase at low temperatures, . However, a dynamic AF correlation length $\xi/a \approx 2$ has been observed for both $x = 0.45$ and $x = 0.51$. The correlation length ξ does not vary with temperature up to 250°K[54,59], suggesting that the copper spin dynamics is governed by the motion of the quasi-particles, therefore the correlation length is related to the hole density, or the distances between holes. Another important result concerning these systems is the observation of a gap in spin spectrum for YBCO[58]. The gap is present in the superconducting phase and extends to the temperatures well above the transition temperature T_c. The gap is clearly seen $\mathbf{S}(\mathbf{Q},\omega)$ at $\mathbf{Q} = (\frac{\pi}{2}, \frac{\pi}{2}, q_z)$[58]. This is consistent with earlier NMR[60] results. The origin of such a gap is currentlly controversial. Some attributes it to the pre-existence of superconducting pairs above the transitoin temperature T_c[43]. However a recent study of $YBa_2Cu_3O_{6+x}$ substituting 4% Cu with nonmagnetic Zn[50], found that the temperature variations of the homogeneous susceptibility χ_s of the CuO_2 planes, probed by the shift of the ^{89}Y NMR line, are nearly unchanged with respect to pure samples $(x > 0.5)$, even though T_c changes dramatically. This observation casts serious doubts about the proposition that these magnetic anomalies are associated with the precursive superconducting pairing or with manifestations of a superconducting gap[54,50]. In addition, a neutron scattering experiment on $La_{1.86}Sr_{0.14}CuO_4$ reports that the structure factor $S(\mathbf{Q},\omega)$ $[\mathbf{Q} = (\pi, (1-\delta)\pi)]$ has no gap in a wide range values of ω[78].

NMR is capable of revealing many magnetic properties of the cuprate super-

conductors. For instance, according to Ref. [13,61], NMR studies found that the Knight shift K of the Cu, O in the plane and Y are all proportional to the macroscopic static susceptibility $\chi(\omega = 0, q = 0)$ strongly supporting the notion that the spin density on the Cu-3d and O-2p state is not only closely connected but also part of the same single component system. Further, the fact that the linear slope of the Knight shift K versus $\chi(0,0)$ is independent of the hole concentration through the metallic state, down to the metal-insulator transition region, demonstrates that $\chi(O)/\chi(Cu)$ (the $Cu-O$ covalency) is nearly independent of oxygen content.

Another important result is the zero Knight shift[13] in the insulating state of $YBa_2Cu_3O_{6+x}$, $x < 0.4$, which seriously questions the possibility that spin and charge degrees of freedom are independent in a resonating-valence-bond approach (RVB).

1.4.3 2D Superconductivity

Conductivities parallel and perpendicular to CuO_2 sheets $\sigma_{\|}$ and $\sigma_{\perp}$ are very different. The value of their ratio $\sigma_{\|}/\sigma_{\perp}$ is compound specific and ranges from ≥ 30 in $YBa_2Cu_3O_7$ to $\sim 10^5$ in the Bi-cuprate[43]. This anisotropy is the result of the layered nature of these compounds. A group[62] inserted additional insulating $PrBa_2CuO_{7-x}$ layers between CuO_2 bilayers of YBCO. For 16 PrBCO layers or more, the zero-resistance transition temperatures saturate at $T_{c0} \approx 19°K$. This shows the 2D nature of high-T_c superconductivity.

1.4.4 Microscopic Parameters of The Superconducting Phase

The magnetic penetration length λ and the coherent length ξ are two important parameters related to the superconducting phase. As expected from the layer structure, they are anisotropic. The values of λ and ξ are well known by now for

$YBa_2Cu_3O_7$ from a variety of measurements :[43]

$$\begin{aligned} \xi_{\parallel} &\approx 14 \pm 2\text{Å}, \\ \xi_{\perp} &\approx 1.5 \sim 3\text{Å}, \\ \lambda_{\parallel} &\approx 1400\text{Å}, \\ \lambda_{\perp} &\approx \sim 7000\text{Å}. \end{aligned}$$

We notice that the correlation length $\xi_{\parallel}$ and $\xi_{\perp}$ are short. As a consequence of it, the number of superconducting pairs in a coherence volume is rather small, which is expected to lead to large fluctuation effects. These fluctuations were indeed observed in conductivity, susceptibility and specfic heat[63,43].

A gap in electron energy spectra is characteristic of superconductors. Knowing its magnitude and symmetry is essential to the understanding of superconducvity of a particular material. For high-T_c superconductors, the magnitudes of gap Δ have been studied with a variety of methods : tunneling spectroscopy, inelastic light scattering, photoemission, and others. According to Ref. [43], tunneling spectroscopy is the traditional technique for superconductors. However, high-T_c materials have very short coherence lengths and complicated surface chemistry, and these require delicate experimental techniques. By now, a remarkable agreement has appeared among many results[64]: The ratio $2\Delta/kT_c$ for tunneling parallel to the planes is approximately $5 \sim 6$. Inelastic light scattering[65] revealed changes of phonon frequencies and damping below T_c. Depending on phonon frequency with respect to the gap, a small shift to lower or higher energy is found[43]. The ratio $2\Delta/kT_c$ has been determined[66] to be ~ 5. Photoemission spectroscopy has the energy and angle resolutions which are adequate to measure the superconducting gap in high-T_c cuprates[43–45,65], and $2\Delta/kT_c \approx 6 - 8$ has been found consistently

both in angle integrated and angle resolved spectroscopy[12,65]. All of the above experimental results establish that the $2\Delta/kT_c$ ratio extends from $5-8$.

Another important issue is the symmetry of the superconducting gap. Various experiments have been performed, and a consistent picture has emerged. Angle-resolved photoemission can probe the gap in the Brillouin zone[44,45,65,67]. Experiments on Bi2212[67] find no significant variation of the magnitude of gap around the fermi surface, and that nodes do not exist around the fermi surface. The Knight shift K measurements at Cu(1) and Cu(2) of $YBa_2Cu_3O_7$ reveal a precipitous drop of χ_s just below T_c[68], which suggests strongly the singlet nature of electron pairs and contradicts the pre-existence of pairing above the transition temperature T_c[54]. Moreover, according to Ref. [68], the K doesn't follow a Yosida function with a weak-coupling $\Delta(T)$, but is better described by a strong-coupling BCS s-wave behavior. The muon-Spin relaxation technique (μSR) is a widely used technique to measure many properties of the superconducting phase. It is also used to reveal the symmetry of the superconducting pair in high-T_c superconductors[69]. According to Ref. [69], the relaxation rate $\sigma(T)$ fits to the functional forms given by the singlet pairing and a minimal variation of $\sigma(T)$ in the low temperature region was found in almost all the hole-doped HTC cuprates, indicating a finite energy gap without nodes and singlet spin pairing in these systems. However, a Raman scattering experiment on Bi2212 indicates that nodes exist around the fermi surface for the superconducting phase[79] All these experiments imply a spin singlet pairing, and more experiments are needed to identify the spatial symmetry of the superconducting pairs, s-wave or d-wave.

1.4.5 Correlation between T_c *and* n_s

As mentioned previously, μSR has been used widely to measure many properties of the superconducting phase, like the transition temperature T_c, the penetration length λ and the density of pairs n_s[69]. According to Ref. [69], in the vortex state of type-II superconductors below T_c, the flux vortex lattice produces a local field distribution having width ΔB, which causes the muon spin depolorization. The relaxation rate $\sigma(T) \propto \Delta B \propto 1/\lambda^2 \propto n_s/m^*$[69]. The muon-spin-relaxation rates σ have been measured in sixteen specimens of the cuprate superconductors (the 214, 123, 2212 and 2223 series), and a universal linear relation between T_c and σ has been observed[69]. According to Ref. [69], the same linear relation has been observed in organic superconductors. This linear relation can not be explained in the frame work of 3D weak coupling BCS superconductivity[69]. Authors of Ref. [69] attribute the observation either to the large energy scale of the pair-mediating boson or to the preformation of superconducting pairs. More work is needed to establish this linear relationship between T_c and n_s, both experimentally and theoretically.

1.4.6 Estimations of Coupling Constant λ

Below the transition temperature T_c, there is a clear gap building up. Photoemission[12,65], Inelastic light scattering[65], tunneling spectroscopy[64], infrared and Raman spectroscopy[70] and other techniques[71,72] have concluded that the gap vs. T_c ratio $2\Delta/kT_c$ ranges from 5 to 8, which is a signal of a very strong coupling superconductivity. In addition, the specific heat anomaly at the transition temperature T_c ($\Delta C/\gamma T_c$)[73] and the precipitous drop below T_c of the nuclear spin relaxation rate[68] are also reminiscent of the strong coupling effects. On the other hand, from the measurements of the resistivity $\rho(T)$, the linear coefficient of the specific heat γ and the normal state spin susceptibility χ_s, a rather weak coupling

of the carriers to the unidentified excitaions[43] is inferred.

Despite the difficulties caused by the lattice degrees of freedom which dominate the total measured C(T), the linear coefficient γ of the electronic specific heat is believed to be within a reasonable band of uncertainty[74]. According to Ref. [43], for the optimal compositions of $La_{2-x}Sr_xCuO_4$, the γ is in the range of $5 - 6mJ/mol°K^2$; for $YBa_2Cu_3O_7$, γ's range from $14 - 25mJ/mol°K^2$. From the values of γ, one can deduce the the value of the density of states at the fermi surface $N_{exp}(0)$. According to Ref. [43], comparing that of the band structure calculation $N_b(0)$, $N_{exp}(0) = (1+\lambda)N_b(0)$, one concludes that the coupling constant λ is about 0.5.

The spin susceptibility χ_s provides another measurement of the density of states N(0), from which one can infer the magnitude of the coupling constant λ according to Ref. [43]. For $YBa_2Cu_3O_7$, one obtains that $\lambda \sim 0.5$; for $La_{2-x}Sr_xCuO_4$, $\lambda \sim 0.5 - 1.0$[43].

Another way of estimating the value of λ is DC resistivity measurement. DC resistivity measurements[75] on $La_{1.825}Sr_{0.175}CuO_4$ and $YBa_2Cu_3O_7$ reveal the absence of resistivity saturation at very high temperatures and implies a weak coupling between current carriers and the unspecific excitations. According to Ref. [75] Resistivity verses temperature remains linear up to 1100 °K for LSCO and 600 °K for YBCO, indicating at once that the mean free lengths l are much longer than interatomic spacings a, at temperatures below 600 °K for LSCO and 1100 °K for YBCO. According to Ref. [75], using a relationship between λ and resistivity[76], careful calculation indicates that $\lambda \leq 0.1$ for LSCO and $\lambda \leq 0.3$ for YBCO, respectively.

Data on the specific heat coefficient γ, the normal state spin susceptibility χ_s and the resistivity ρ(T) all infer a weak coupling of current carriers to the unspecified bosons. This seems in contradiction to experimentally measured values of $2\Delta/K_BT_c$. The apparent paradox can be conceivably attributed to the 2D nature of the system or to some unrevealed pair-breaking mechanism[43].

1.4.7 a Emergying Microscopic Picture

From the above discussions and many other experiments, some consensus has emerged with regard to some microscopic characters of high-T_c materials. (i) An undoped cuperate is an insulator or a semiconductor while CuO_2 sheets can be described by the 2D S = 1/2 Heisenberg antiferromagnet at high temperature and the 3D Néél state at low temperature. (ii) Doping introduces holes to the CuO_2 sheets. Those holes exhibit Cu3dx^2-y^2 − O2pσ characters with O2pσ dominating. When the concentration is low, they are localized. The system remains 3D antiferromagnetic; however, the 3D-AF order becomes weaker. (iii) When the concentration of holes exceeds a critical value $n_c^h \approx 0.02$, the holes become delocalized. An insulator-metal transition has occurred and the system is now a metal. The 3D-AF order no longer exists. Holes are fermions, move around in 2D dynamic antiferromagnetically correlated medium and can be described as fermi liquid or near fermi liquid. Although it is still controversial, many experiments indicate that at superconducting transition temperature T_c, those holes form singlet Cooper pairs and the system converts to a superconducting phase.

Although much progress in experiments has been made, some critical issues remain in the need to be sorted out. For instance, although local density approximation has been extremely successful in predicting fermi surfaces, there is no consensus

on whether high-T_c materials can be described by conventional fermi liquids; Some mechanisms[4] advocate the pre-existence of superconducting pairs; one supporting evidence is that neutron scattering experiments on YBCO reveal a gap in spin spectrum[56,58] although the origin of the gap remains to be determined. It is also known that $2\Delta/K_BT_c$ is $5-8$, much larger than that of BCS value , while many experiments result in a small coupling constant λ, etc. All these issues need to be resolved before consensus on the superconducting mechanism can be reached.

References

1. G. Bednorz and K. A. Muller, *Z. Physik B* **64**, 189 (1986); Chu *et. al. Phys. Rev. Lett.*
2. G. Chen and W. A. Goddard III, *Science* **239**, 899 (1988); G. Chen, J-M Langlois, Y. Guo and W. A. Goddard III, *Proc. Natl. Acad. Sci.* **86**, 3447 (1989)
3. P. W. Anderson *Science* **235**, 1196 (1987)
4. N. F. Mott, *Phil. Mag. B* **60**, 365 (1989)
5. P. Prelovsek, T. M. Rice, and F. C. Zhang, *J. Phys. C* **20**, L229 (1987)
6. V. J. Emery, *Phys. Rev. Lett.* **58**, 2794 (1987)
7. J. R. Schrieffer, X. G. Wen, S. C. Zhang, *Phys. Rev. Lett.* **60**, 944 (1988)
8. R. J. Cava, *Scientific American*, August, 42 (1990)
9. Y. Guo, J-M Langlois and W. A. Goddard III, *Science* **239**, 896 (1988)
10. G. Lang, H. Ding and W. A. Goddard III, to be submitted
11. T. Takahashi *et al.*, *Nature* **334**, 691 (1988)
12. C. G. Olson *et al. Phys. Rev. B* **42**, 381 (1990)
13. H. Alloul, P. Mendels, G. Collin and P. Monod, *Phys. Rev. Lett.* **61**, 746 (1988); H. Alloul, T. Ohno and P. Monod, *Phys. Rev. Lett.* **63**, 1700 (1989); G. Balalakrishnan *et al.*, *J. Phys. C* **21**, L847 (1988).
14. R. Birgeneau and G. Shirane, *Physical Properties of High-Temperature Superconductors*, D. M. Ginsberg, ed. (World Scientific, Singapore, 1989); J. M. Tranquada *et al.*, *Phys. Rev. B* **38**, 2477 (1988).
15. G. Chen and W. A. Goddard III, to be submitted.
16. G. Chen, H. Ding and W. A. Goddard III, submitted to *Phys. Rev. B.*

17. M. Takahashi, *Phys. Rev. Lett.* **62**, 2313 (1989).

18. J.D. Reger and A.P. Young, *Phys. Rev. B* **37**, 5978 (1988).

19. N. Trevedi and D.M. Ceperly, *Phys. Rev. B* **40**, 2749 (1989).

20. J. Carlson, *Phys. Rev. B* **40**, 846 (1989).

21. M. Gross, E. Sanchez-Velasco and E. Siggia, *Phys. Rev. B* **39**, 2484 (1989); *Phys. Rev. B* **40**, 11328 (1989).

22. H.-Q. Ding and M.S. Makivic, Phys. Rev. Lett. **64**, 1449 (1990). M.S. Makivic and H.-Q. Ding, *Phys. Rev. B* **43**, 3562 (1991).

23. H.-Q. Ding, *Phys. Lett.* **A159**, 355 (1990).

24. S. Chakravarty, B.I. Halperin and D.R. Nelson, *Phys. Lett.* **60**, 1057 (1988); *Phys. Rev. B* **39**, 2344 (1989).

25. D.P. Arovas and A. Auerbach, *Phys. Rev. B* **38**, 316 (1988). A. Auerbach and D. P. Arovas, *Phys. Rev. Lett.* **61**, 617 (1988).

26. R.R.P. Singh, *Phys. Rev. B* **39**, 9760 (1989).

27. M. Takahashi, *Phys. Rev. B* **40**, 2494 (1989).

28. T. Oguchi, *Phys. Rev.* **117**, 117 (1960).

29. H. A. Bethe, *Z. Physik* **71**, 205 (1931).

30. J. des Cloizeaux and J. J. Pearson, *Phys. Rev.* **128**, 2131 (1962).

31. E. R. Gabliano and C. A. Balseiro, *Phys. Rev. Lett.* **59**, 2999 (1987).

32. R. G. Gordon, *J. Math. Phys.* **9**, 655 (1968).

33. G. Gross and G. Pastori Parravicini, *Advances in Chemical Physics* **62**, 133 (1985).

34. For a review, see E. Manousakis, *Rev. Mod. Phys.* **63**, 1 (1991).

35. P.W. Anderson, *Phys. Rev.* **86**, 694 (1952); R. Kubo, *Phys. Rev.* **87**, 568

(1952).

36. R. Blankenbecler and R. L. Sugar, *Phys. Rev.* D**27**, 1304 (1983).

37. J.H. Hetherington, *Phys. Rev.* **A30**, 2713 (1984).

38. M.H. Kalos, *J. Comp. Phys.* **1**, 257 (1966).

39. G.C.Fox, et al., in *Solving Problems on Concurrent Processors*, Prentice Hall, Englewood Cliffs, New Jersey (1988). H.-Q. Ding, *Comput. Phys. Commun.* **65**, 92 (1991).

40. H. Neuberger, T. Ziman, *Phys. Rev. B* **39**, 2608 (1989).

41. G. Aeppli *et al.*, *Phys. Rev. Lett.* **62**, 2052 (1989).

42. G. Shirane, *et al.*, *Phys. Rev. Lett.* **59**, 1613 (1987). Y. Endoh, et al., *Phys. Rev. B* **37**, 7443 (1988).

43. B. Batlogg *et al.*, *Physica B* **169**, 7 (1991).

44. J. C. Campuzano *et al.*, *Phys. Rev. Lett.* **64**, 2308 (1990).

45. J. W. Allen *et al.*, *Phys. Rev. Lett.* **64**, 595 (1990).

46. W. E. Picket, *Rev. Mod. Phys.* **61**, 689 (1989); R. E. Cohen, W. E. Pickett, H. Krakauer, *Phys. Rev. Lett.* **62**, 831 (1989); *ibid*, **64**, 2575 (1990); K. Schwarz, C. Ambrosch-Draxl, P. Blaha, *Phys. Rev. B* **42**, 2051 (1990).

47. J. Yu, S. Massida, A. J. Freeman and D. D. Koelling, *Phys. Lett. A* **122**, 203 (1987); S. Massidda, J. Yu and A. J. Freeman, *Physica C* **52**, 251 (1988).

48. H. Haghighi *et al.*, *Phys. Rev. Lett.* **67**, 382 (1991).

49. H. Alloul, *Physica B* **169**, 51 (1991).

50. H. Alloul *et al.*, *Phys. Rev. Lett.* **67**, 3140 (1991).

51. J. M. Luttinger, *Phys. Rev.* **119**, 1153 (1960).

52. D. Vaknin *et al.*, *Phys. Rev. Lett.* **58**, 2802 (1987).

53. Y. Kitaoka *et al.*, *J. Phys. Soc. Japan* **56**, 3024 (1987); I. Watanabe *et al.*, *J. Phys. Soc. Japan* **56**, 3028 (1987).

54. J. Rossat-Mignod *et al.*, *Physica B* **169**, 58 (1990).

55. P. Mendels *et al.*, *Physica C* **185-189**, 1191 (1991).

56. J. Rossat-Mignod *et al.*, *Physica C* **152**, 19 (1988).

57. J. M. Tranquada *et al.*, *Phys. Rev. Lett.* **60**, 156 (1988).

58. J. Rossat-Mignod *et al.*, *Physica C* **162-164**, 1269 (1989); J. Rossat-Mignod *et al.*, *Physica C* **163**, 4 (1990).

59. R. J. Birgeneau *et al.*, *Phys. Rev. B* **38**, 6614 (1988).

60. W. W. Warren *et al.*, *Phys. Rev. Lett.* **62**, 1193 (1989).

61. P. Butaud *et al.*, *Physica C* **166**, 301 (1990);

62. D. H. Lowndes, D. P. Norton and J. D. Budai, *Phys. Rev. Lett.* **65**, 1160 (1990).

63. M. B. Salamon *et al.*,*Phys. Rev. B* **38**, 885 (1988).

64. J. Geerk *et al.*, *Physica C* **162-164**, 837 (1989); M. E. Hawley *et al.*, *Phys. Rev. B* **35**, 7224 (1989); S. Pan *et al.*, *Phys. Rev. B* **35**, 7220 (1989); J. R. Kirtley *et al.*, *Phys. Rev. B* **35**, 7216 (1989).

65. R. Manzke *et al.*, *Physica C* **162-164**, 1381 (1989); J. M. Imer *et al.*, *Phys. Rev. Lett.* **62**, 336 (1989).

66. B. Friedl, C. Thomsen and C. Cardona, *Phys. Rev. Lett.* **65**, 915 (1990).

67. C. G. Olson, *Physica B* **169**, 112 (1991); C. G. Olson *et al.*, *Science* **245**, 731 (1989).

68. M. Takigawa *et al. Phys. Rev. B* **39**, 7371 (1989); S. E. Barrett *et al.*, *Phys. Rev. B* **41**, 6283 (1990).

69. Y. J. Uemura, *Physica B* **169**, 99 (1990); Y. J. Uemura *et al.*, *Phys. Rev. Lett.* **62**, 2317 (1989); Y. J. Uemura *et al.*, *Phys. Rev. B* **38**, 909 (1988).

70. M. V. Klein, Physica C **162-164**, 1701 (1989); R. Hackl *et al.*, Phys. REv. B. **38**, 7133 (1988); Physica **162-164**, 1241 (1989).

71. T. Timusk and D. B. Tanner, in *Physical Properties of High-Temperature Superconductors*, Vol. I., N. M. Ginsberg, ed. (World Scientific, Singapore, 1989), p.339.

72. K. E. Gray, *Mod. Phys. Lett. B* **2**, 1125 (1988).

73. N.E. Phillips *et al.*, *Phys. Rev. Lett.* **65**, 357 (1990); N. Okazaki *et al.*, *Phys. Rev. B* **41**, 4296 (1990).

74. J. W. Loram *et al.*, *Physica C* **162-164**, 498 (1989); B. Batlogg *et al.*, *Phys. Rev. B* **35**, 5340 (1987); D. K. Finnemore *et al.*, *Phys. Rev. B* **35**, 5319 (1987);

75. M. Gurvitch and A. T. Fiory, *Phys. Rev. Lett.* **59**, 1337 (1987).

76. B. Chakraborty, W. E. Pickett, and P. B. Allen, *Phys. Rev. B* **14**, 3227 (1976); P. B. Allen *et al.*, *Phys. Rev. B* **34**, 4331 (1986).

77. J. Schmanlian, G. Baumgartel, and K-H Bemenan, *Phys. Rev. Lett.* **68**, 1406 (1992); G. A. Thomas *et al.*, *Phys. Rev. Lett.* **67**, 2906 (1991).

78. T. E. Mason, G. Aeppli, and H. A. Mook, *Phys. Rev. Lett.* **68**, 1441 (1992).

79. T. Staufe *et al.*, *Phys. Rev. Lett.* **68**, 1069 (1992).

80. M. Makivic and M. Jarrell, *Phys. Rev. Lett.* **68**, 1770 (1992).

Chapter 2.

Electron-Phonon Interaction and Superconductivity in A_xC_{60}

Guanhua Chen and William A. Goddard III

Materials Simulation Center, Beckman Institute

California Institute of Technology, Pasadena, CA 91125

Abstract

The electron-phonon couplings are caused by both the changes of electron-ion coulomb interactions while freezing electron orbitals, *the static coupling*, and the adjustments of the electronic states to the lattice vibrations, *the dynamic coupling*. We have investigated both static and dynamic coupling for alkali compounds of Buckminsterfullerene A_xC_{60}, based on which we calculated many properties related to the superconducting phase, such as the transition temperature T_c, the isotope exponent α_c, and $\Delta T_c|_{1GPa}$, etc. By comparing these calculated values with current experimental data, we determined the relative contributions to the electron-electron pairing from the static and dynamic coupling, and predicted that $\alpha_k \approx 0.1 - 0.2$ for the potassium isotope effect.

2.1 Introduction

Recent discovery[1] of superconducting potassium-doped icosahedral compound K_xC_{60} stimulated much experimental and theoretical interests[2-13]. It has been determined that the superconducting phase is K_3C_{60} and that the structure is a face-centered cubic (f.c.c)[3]. Since then, many other superconducting alkali compounds of C_{60} have been synthesized; their transition temperatures T_c range from 2.5°K to 33°K[1,14-17], see Table 1. A natural question arises : Are these compounds conventional phonon-mediated electron pairing superconductors ?

Table 1. The Transition temperatures T_c *of* A_xC_{60}[14-17]

Composition	T_c(°K)
$RbCs_2C_{60}$	33
Rb_2CsC_{60}	31
Rb_3C_{60}	29
KRb_2C_{60}	27
K_2RbC_{60}	23
K_3C_{60}	19
Na_2CsC_{60}	12
Li_2CsC_{60}	12
Na_2CsC_{60}	12
Na_2RbC_{60}	2.5
Na_2KC_{60}	2.5

Several mechanisms[4-6] have been proposed to explain the superconductivity in these materials. Among the proponents of phonon-mediated electron-pairing

mechanisms, disagreements arise regarding which phonon modes are responsible for the superconductivity. One group suggests that the high frequency intramolecular phonon modes of C_{60} couple with conduction electrons to give superconductivity. Another group argues that it is the coupling between the low frequency intermolecular phonon modes of K_3C_{60} and the conduction electrons which lead to superconductivity. Varma *et. al.* [4] suggested that intramolecular vibrations strongly scatter electrons near the fermi surface by dynamic Jahn-Teller effect. Using a frozen-phonon technique, they calculated the Jahn-Teller coupling matrix and concluded that $\lambda \approx 0.3 - 0.9$. Based on these, they were able to show the linearity of T_c vs. N(0) and therefore possibly explain the linear dependence of T_c and the lattice constant A observed in experiment[12]. In their calculation they used a value of $N(0) \approx 10 \sim 20$ states/eV-spin-C_{60} which is $5 \sim 10$ times as high as that of a photoemission experiment[7], but is consistent with the critical field and normal state susceptibility measurements[18]. If we use the photoemission experiment's value of $N(0) \approx 2$ states/eV-spin-C_{60}, then $\lambda < 0.2$, which is too weak to give rise of superconductivity in these systems.

Zhang *et. al.*[6], on the other hand, have estimated various contributions to the electron-electron interaction in K_3C_{60}, and showed that the K^+ optical-phonon modes induce a strong attraction which should be the main source of superconductivity. They also studied the charge density wave in these systems and concluded that because of the frustrations, the charge density wave phase is less stable than the superconducting phase.

In addition to the phonon-mediated electron pairing mechanisms, some exotic mechanisms[5] have also been proposed to explain the superconductivity of

A_xC_{60}. Chakravarty *et. al.* and Baskaran and Tosatti argue that two electrons may pair by electron-electron exchange and correlation on a single C_{60} molecule[5]. Baskaran and Tosatti attribute it to the "stability of molecular singlet" (SMS). However, Zhang *et. al.*[6] adopted the polyacetylene model of Su, Schrieffer and Heeger[19] to describe behavior of a single C_{60} molecule. They found a difference in length between long and short bonds in excellent agreement with experiment. Based on this, they calculated the energy gain from "SMS", which was found to be $1 \sim 2$ orders less than the energy gain resulting from the coupling between conducting electrons and K^+ optical phonon modes. They concluded that "SMS" is too weak to give arise of superconductivity in these systems.

We present here a thorough and quantitative study of A_xC_{60} (A = alkali element). In *Sec. 2.2* we calculate the electronic structures of a C_{60} and discuss its ground states, excited states, and the corresponding energies of each state. It is important to know the electronic structure of a single C_{60} because the icosahedral C_{60} molecular orbitals maintain their identity in A_xC_{60} except for the crystal-field effects. In *Sec. 2.3* we calculate *the static electron phonon coupling* constant (the *static electron phonon coupling* is defined as the coupling between electron and phonon caused by the change of the electron-ion coulomb interactions.) and its implications or connections to the superconductivity of A_xC_{60}. In *Sec. 2.4* we discuss the Jahn-Teller effects and the *dynamic* coupling between the electrons at LUMO and the intramolecular phonon modes (the *dynamic coupling* is caused by the respondings of electron local orbitals to the phonon distortions). In *Sec. 2.5* we calculate various properties related to the superconductivity and obtain a comprehensive picture of the superconducting phase in these systems.

2.2 C_{60} Chemistry

A C_{60} molecule has icosahedral symmetry I_h. It looks like a soccer ball, and has 12 pentagons and 20 hexagons, Fig. (1). Each carbon atom is adjacent to three nearest C, and this makes 90 bonds. Of the 90 bonds, 30 are double bonds and 60 are single bonds. Double bonds are shared by adjacent hexagons and single bonds forms pentagons. It is interesting to know its geometry and its electronic structures. Because of the relatively large size of a C_{60}, it is very expensive to do *ab initio* calculations. An alternative is MNDO[20], which is a semi-empirical technique and has been used successfully on a wide variety of carbon compounds. We present here a MNDO[20] study of one C_{60} molecule.

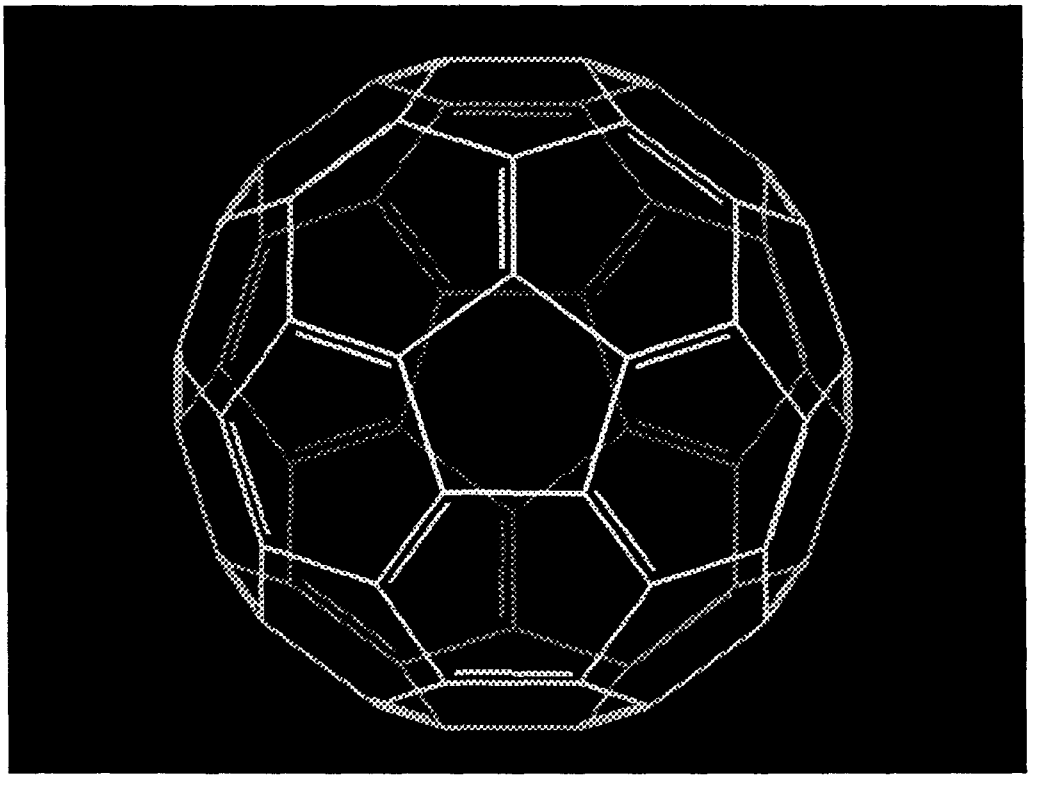

Fig. (1), structure of a C_{60} molecule

2.2.1 Geometry of a C_{60}

^{13}C NMR experiment[21] data indicate the lengths of the single and double bonds in C_{60} are 1.45Å and 1.40Å, respectively. Theoretical calculations[22] indicate that the double bond length $R_{db} \approx 1.40$Å and the single bond length $R_{sb} \approx 1.47$Å. To obtain the optimal geometries of C_{60}, C_{60}^{-} and C_{60}^{3-}, we performed MNDO calculations on five different pairs of double and single bond lengths ($R_2 = 1.40$Å for double bond and $R_1 = 1.47$Åfor single bond). Those structures were obtained by a minimization procedure using BIOGRAF[25]. Since R_1 and R_2 are very close to the optimal bond lengths R_{sb} and R_{db}, respectively, we can use the following harmonic approximation to express the total energy :

$$E = E_0 + \alpha_1(R_1 - R_{sb})^2 + \alpha_2(R_2 - R_{db})^2 \qquad (1)$$

In Table 2, we list the results from five MNDO calculations, in which total charge and total spin of C_{60}, C_{60}^{-} and C_{60}^{3-} are $(0,0)$, $(-1,1/2)$ and $(-3,3/2)$, respectively. Having five sets of known values of E, R_1 and R_2, we solved for the values of R_{sb}, R_{db}, α_1, α_2 and E_0. From the above procedure, we obtained the optimal geometries for C_{60}, C_{60}^{-} and C_{60}^{3-}. In Table 3, we list the optimal single and double bond lengths, R_{sb} and R_{db}, and their corresponding ground state spins and energies. Our results of the bond lengths 1.474Å and 1.399Å of a neutral C_{60} are close to the experimental data[21] and other theoretical results.

Table 2. MNDO Energies (eV) for Five Different Sets of Geometries†

R_{sb}(Å)	R_{db}(Å)	$E_{C_{60}}$	$E_{C_{60}^-}$	$E_{C_{60}^{3-}}$
1.470	1.400	−7636.93824	−7639.66408	−7636.08235
1.475	1.395	−7636.94118	−7639.58489	−7635.91726
1.475	1.400	−7636.95759	−7639.63115	−7636.03848
1.475	1.405	−7636.93251	−7639.63643	−7636.10269
1.480	1.400	−7636.89968	−7639.54108	−7635.90057

† we used the five sets of data E, R_{sb} and R_{db} to obtain the optimal geometries of C_{60}, C_{60}^- and C_{60}^{3-}.

Table 3. Parameters of Optimal MNDO Geometries†

Molecule	R_{sb}(Å)	R_{db}(Å)	S	E(eV)
C_{60}	1.47375	1.39948	0	−7636.95988
C_{60}^-	1.47166	1.40314	$\frac{1}{2}$	−7639.63838
C_{60}^{3-}	1.47017	1.40813	$\frac{3}{2}$	−7636.20593

† the optimal geometries are obtained by the procedure described in the previous paragraph.

Table 3 tells us that extra electrons on C_{60} enlarge the double bond length but decrease the single bond length. The difference between the double and single bond lengths is now smaller. The extra electrons tend to make the distributions of the bond lengths more uniform. The amount of increase in a double bond length is much larger than the decrease in a single bond. The net result is a slight increase of the bucky ball size, which is less than 0.1% for the linear dimension of the C_{60} molecule.

2.2.2 Chemistry of a C_{60}

Some groups[11,23] have studied molecular orbitals of a C_{60}. Basic features are that the highest occupied molecular orbitals (HOMO) have a five-fold degeneracy with H_u symmetry, and that the lowest unoccupied orbitals (LUMO) have a three-fold degeneracy with T_{1u} symmetry. These H_g and T_{1u} are d and p-like orbitals, respectively. In Fig. (2) we plot a LUMO resulting from our MNDO calculation, showing a mix of p_x, p_y and p_z like orbital. However, it clearly has the inversion-u symmetry and is antibonding at the double-bonding sites, which is expected.

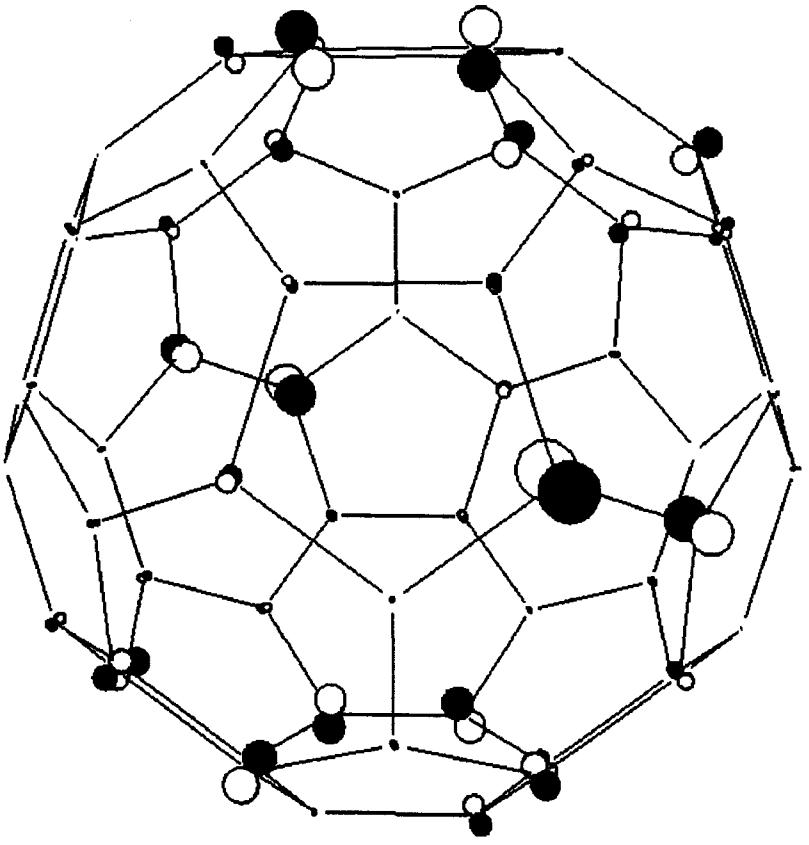

Fig. (2), a LUMO of a C_{60}, which is a mix of p_x, p_y and p_z like orbitals

It is also interesting to know the electronic structures of various spin states. Table 4a lists total energies of various states for three different geometries, C_{60}, C_{60}^{-}, C_{60}^{3-}, and a crystalline K_3C_{60} (the crystalline structure is optimized by BIOGRAF[25] (a sofeware developed by Molecular Simulations Inc., Sunnyvale, California) employing simply the force field of KC_{24}[26], which will be explained later).

Table 4a. Results of MNDO Calculations†. (energies are in units of eV*)*

Q	S	$E_{C_{60}}$	$E_{C_{60}^{-}}$	$E_{C_{60}^{3-}}$	$E_{K_3C_{60}}$
0	0	−7636.95988	−7636.94917	−7636.90409	−7636.33305
−1	$\frac{1}{2}$	−7639.63838	−7639.66303	−7639.65868	−7639.22245
−2	0	−7639.13605	−7639.19692	−7639.23746	−7638.92265
−2	1	−7639.23343	−7639.29236	−7639.32713	−7639.00755
−3	$\frac{1}{2}$	−7635.56883	−7635.66326	−7635.74277	−7635.52861
−3	$\frac{3}{2}$	−7635.72828	−7636.13119	−7636.20593	−7635.97065
−4	0	−7628.82836	−7628.95721	−7629.07798	−7628.95095
−4	1	−7629.33372	−7629.47784	−7629.58190	−7629.31815
−4	2	−7629.52294	−7629.64761	−7629.76463	−7629.61665

† these MNDO calculations were performed without explicit C.I. options.

In order to test the applicability of MNDO method on C_{60}, we calculate the first electron affinity, the ionization energy and the heat of formation for a neutral C_{60} with MNDO. If MNDO is indeed reliable, the calculated results should be comparable to that of experimentally determined values. From our MNDO calculations the first electron affinity is 2.68eV while experimental measurements of the quantity yield the value of 2.65 ± 0.05 eV[24]. This gives us the confidence to

our calculated results.

The LUMO of C_{60} has T_{1u} of symmetry and the HOMO has H_u symmetry. The ground states are S = 0 for C_{60}; S = 1/2 for C_{60}^{-}; S = 1 for C_{60}^{2-}; S = 3/2 for C_{60}^{3-} and S = 2 for C_{60}^{4-}. This is consistent with Hund's rule. All these MNDO calculations are performed without the C.I. (configuration interactions) option. Some groups proposed a "Stable Molecular Singlet" (SMS) mechanism to explain the superconductivities observed in A_xC_{60}. They suggested that the energy of the singlet states C_{60}^{2-} and C_{60}^{4-} is lower than that of two C_{60}^{3-}. From our MNDO calculations, we found that for gas phase,

$$E_{C_{60}^{2-}}(0,-2) + E_{C_{60}^{4-}}(0,-4) = -15268.31544 \text{ eV}$$

and

$$E_{C_{60}^{3-}}(\frac{3}{2},-3) = -7636.20593 \text{ eV},$$

while for crystalline K_3C_{60},

$$E_{K_3C_{60}}(0,-2) + E_{K_3C_{60}}(0,-4) = -15267.87360 \text{ eV},$$

and

$$E_{K_3C_{60}}(\frac{3}{2},-3) = -7635.97065 \text{ eV}.$$

For both gas phase and crystalline K_3C_{60}, the total ground state energy of two C_{60}^{3-} is less than that of the spin singlet states of C_{60}^{2-} and C_{60}^{4-} by $\sim$ 4eV. Furthermore, we notice that the MNDO(no C.I.) ground state of C_{60}^{2-} and C_{60}^{4-} are not spin singlets but are high spin states, S = 1 for C_{60}^{2-} and S = 2 for C_{60}^{4-}. SMS seems to be a remote possibility.

In Table 4b we list results of the same MNDO calculations as those in Table 4b but with C.I. (Configuration Interaction). The basic conclusions are not altered with C.I. option. The ground states are still those high spin states, except for the case of Q = −4, where the ground state's spin is S = 1 instead of S = 2. Even when we take the ground state energies of C_{60}^{2-} and C_{60}^{4-} instead of those of the spin singlets, and include the electronic correlations, the total ground state energy of C_{60}^{2-} and C_{60}^{4-} is still about 3.1 eV higher than that of two C_{60}^{3-} for both gas and crystal phases. Energy gain from geometry relaxation or Jahn-Teller effect is less than 0.1 eV and do not change the picture. Hence the possibility of SMS's playing a role in the superconductivity of alkali Buckminsterfullerene A_xC_{60} is effectively eliminated.

Table 4b. Results of MNDO CI Calculations. (energies are in units of eV)

Q	S	C.I.†	$E_{C_{60}^{3-}}$	$E_{K_3C_{60}}$
−2	0	(3,1)	−7639.25463	−7638.94085
−2	1	(3,0)	−7639.32578	−7639.00760
−3	$\frac{1}{2}$	3	−7636.02060	−7635.79886
−4	0	3	−7629.68417	−7629.54935
−4	0	(6,2)	−7629.68963	−7629.55765
−4	1	(6,1)	−7629.97025	−7629.82965
−4	2	(6,0)	−7629.93171	−7629.73355

† the C.I. options used in the calculations.

Because of symmetry, the ground states of C_{60}^{-} and C_{60}^{2-} are subject to first-order Jahn-Teller effects, while those of C_{60} and C_{60}^{3-} are not. On the other hand,

the energy gap Δ between the spin QUARTET and the spin DOUBLET of triply charged C_{60} is $\Delta = E_{C_{60}^{3-}}(S = \frac{1}{2}; Q = -3) - E_{C_{60}^{3-}}(S = \frac{3}{2}; Q = -3) = 0.46$ eV (without CI) and 0.19 eV (with CI) for the gas phase; $E_{K_3C_{60}}(S = \frac{1}{2}; Q = -3) - E_{K_3C_{60}}(S = \frac{3}{2}; Q = -3) = 0.44$ eV (without CI) and 0.18 eV (with CI) for the crystalline K_3C_{60}. From a LDA calculation[11] the dispersion of LUMO bands is about $\sim$ 0.5 ev. This means that the spin states of C_{60}^{3-} in crystals is a mix of S = 1/2 and S = 3/2. The S = 1/2 state of C_{60}^{3-} is Jahn-Teller active in the first order. This means that the electron at fermi surface is subject to Jahn-Teller effects and it will be discussed later at length.

In conclusion, we obtained the optimal MNDO geometries for C_{60}, C_{60}^{-}, C_{60}^{3-}, which are important late to the study of Jahn-Teller effects; we also calculated the electronic structures of a C_{60} and effectively eliminated the "SMS" mechanism for the superconductivities in A_xC_{60}.

2.3 Static Electron-Phonon Couplings

2.3.1 Lattice Vibrations of A_xC_{60}

The force field method parameterizes the microscopic interaction by chemical bond interactions, Lennard-Jones potentials, coulomb interactions and various correlation interactions, etc. It is being widely used to simulate organic and other systems. The force fields for graphite systems have been well established. Because C_{60} compounds have a close resemblance to the graphite systems in their structures, we may use the force field[26] of the intercalated graphite KC_{24} to simulate vibrations of C_{60} and K_3C_{60}. In Table 5, we list the vibrational frequencies of a C_{60} using the graphite force field[26], and compare them to the experimental measurements. For the majority of IR and Raman active modes, the differences between the calculated and experimental frequencies are less than 6%, and in the worst case the difference is about 12%. The calculated values of low frequency modes are quite close to those of the experimental measurements, and only three high frequency modes $H_g(6)$, $T_{1u}(4)$ and $A_g(2)$, have deviations of more than 10%, which is reasonable. On the basis of these results, we conclude that the graphite force field gives a good description of C_{60} vibration modes, and will use it in our study of A_xC_{60}. (Starting from the graphite force field Guo and Goddard[27] included more angle-angle and angle-bond correlation terms, and obtain a quality force field for C_{60}. The resulting values of vibrational frequencies are listed in column 2 of Table 5.)

Table 5. The vibrational frequencies of C_{60}

mode	GraFF† (cm^{-1})	C_{60}FF‡ (cm^{-1})	Exp. (cm^{-1})	Active
$H_g(1)$	261	279	273	Raman
$H_g(2)$	435	430	434	Raman
$H_g(3)$	759	711	710	Raman
$H_g(4)$	750	774	774	Raman
$H_g(5)$	1080	1099	1100	Raman
$H_g(6)$	1104	1250	1250	Raman
$H_g(7)$	1321	1423	1426	Raman
$H_g(8)$	1517	1576	1576	Raman
$A_g(1)$	488	493	496	Raman
$A_g(2)$	1281	1462	1470	Raman
$T_{1u}(1)$	556	528	527	IR
$T_{1u}(2)$	574	581	577	IR
$T_{1u}(3)$	1113	1183	1183	IR
$T_{1u}(4)$	1276	1439	1428	IR

† frequencies were obtained using the force field of KC_{24}; ‡ frequencies were obtained by Guo and Goddard[27] using improved force field.

We used the force field[26] of the intercalated graphite KC_{24} to optimize the fcc crystal structure of K_3C_{60}. The resulting lattice constant a = 14.18 Å while a x-ray diffraction experiment[3] reveals a simple fcc structure with the lattice constant of 14.24 ± 0.01 Å. The force field was then used to calculate the full phonon spectrum (189 modes for each **k** state of the Brillouin zone)[9]. Fig. (3) shows the density of phonon states for K_3C_{60}.

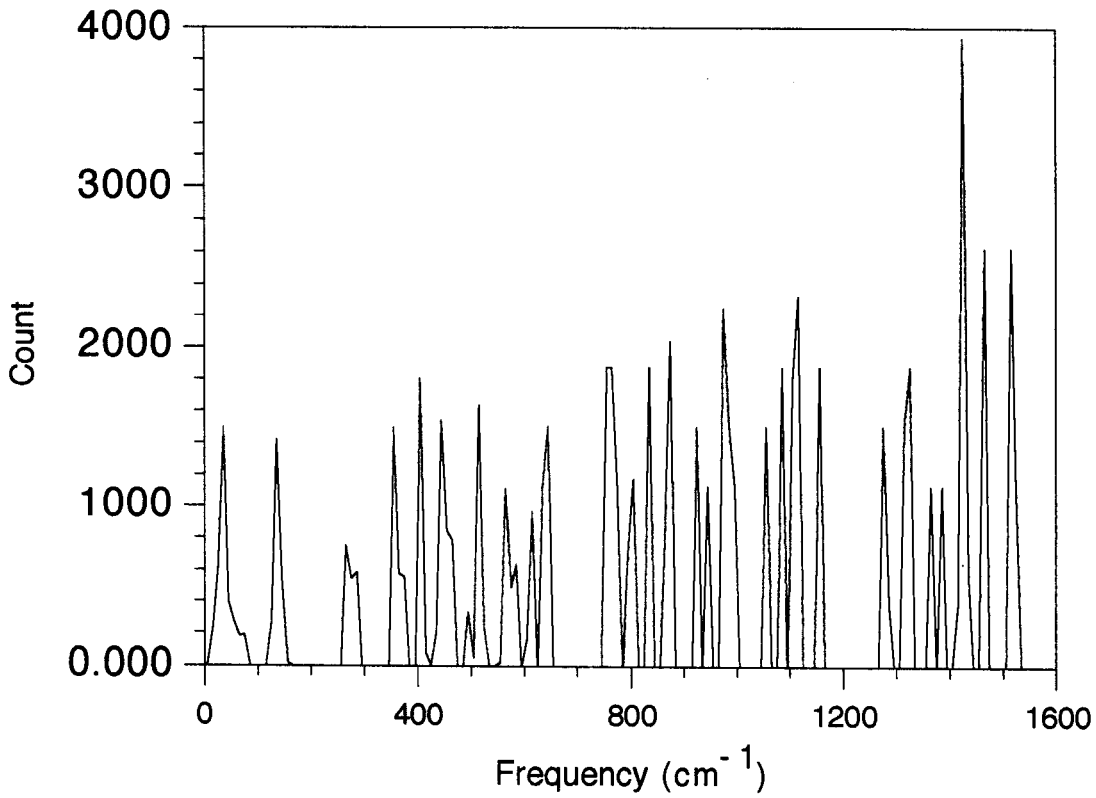

Fig. (3), relative phonon density of states vs. frequency; the lowest two peaks correspond to the intermolecular vibrations and other higher frequency peaks correspond to C_{60} intramolecular modes.

The response of K_3C_{60} to the external pressure is studied. We optimize the crystal structures of K_3C_{60} under the external pressures of 1, 3, 5, 8 and 10 GPa. And then we calculate their corresponding phonon frequencies at the Γ point. Results are plotted in Fig. (4). All the responses up to 10 GPa can be fitted to polynomials of order two. $\frac{1}{V}[\partial V/\partial P]_{P=0} \approx -2.27 \times 10^{-3}$/Kbar at P < 1Gpa. The intermolecular modes respond much more strongly than those of intramolecular modes. The frequencies of the intermolecule modes change $\sim$ 10% in magnitude per GPa when compared to those of the intramolecules' 1% or less (for transverse optical modes of octahedral K, the change is $\sim$ 30% per GPa, Fig. (4b).

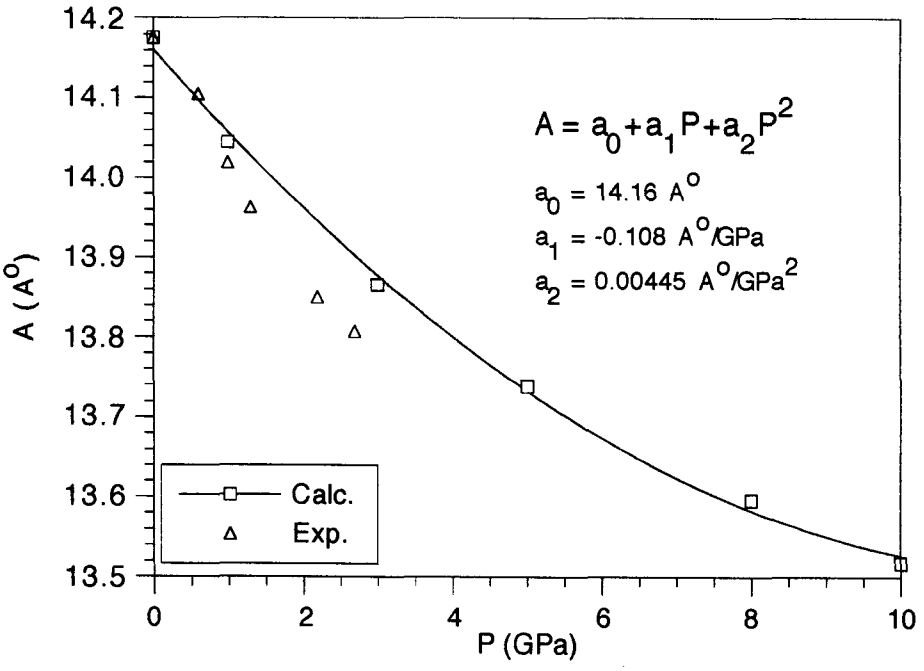

Fig. (4a), lattice constant A vs. pressure.

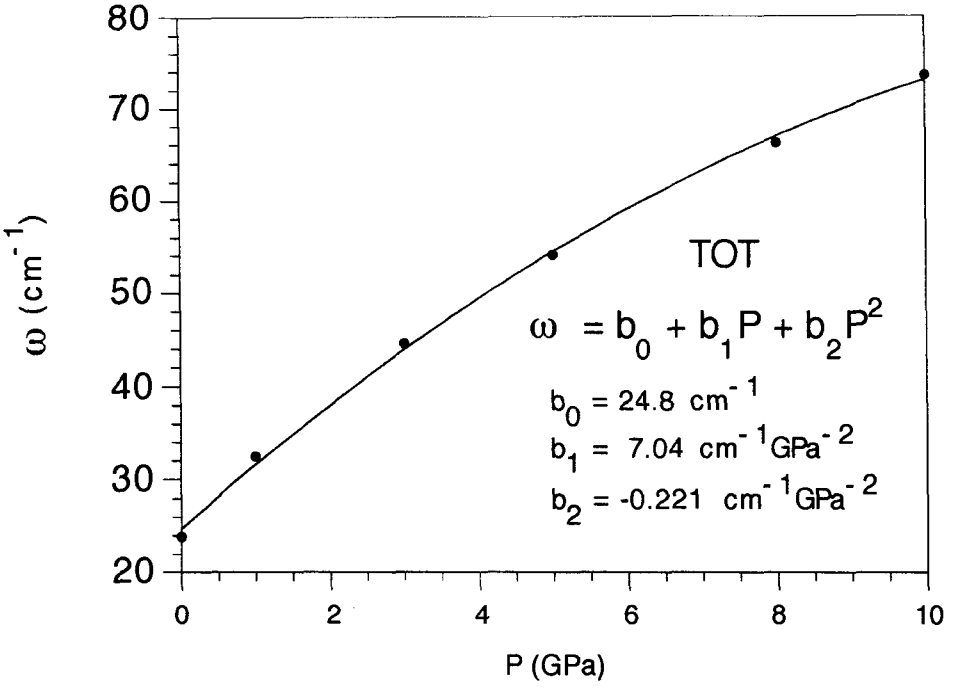

Fig. (4b), frequency vs. pressure for the transverse modes of octahedral K

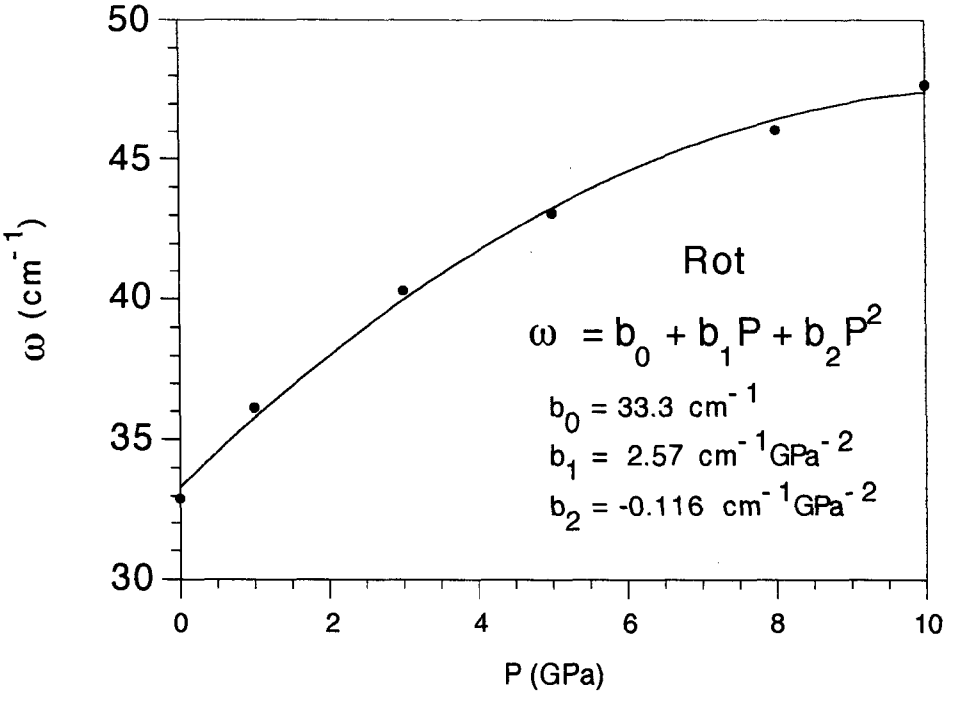

Fig. (4c), frequency vs. pressure for the libration mode of C_{60}

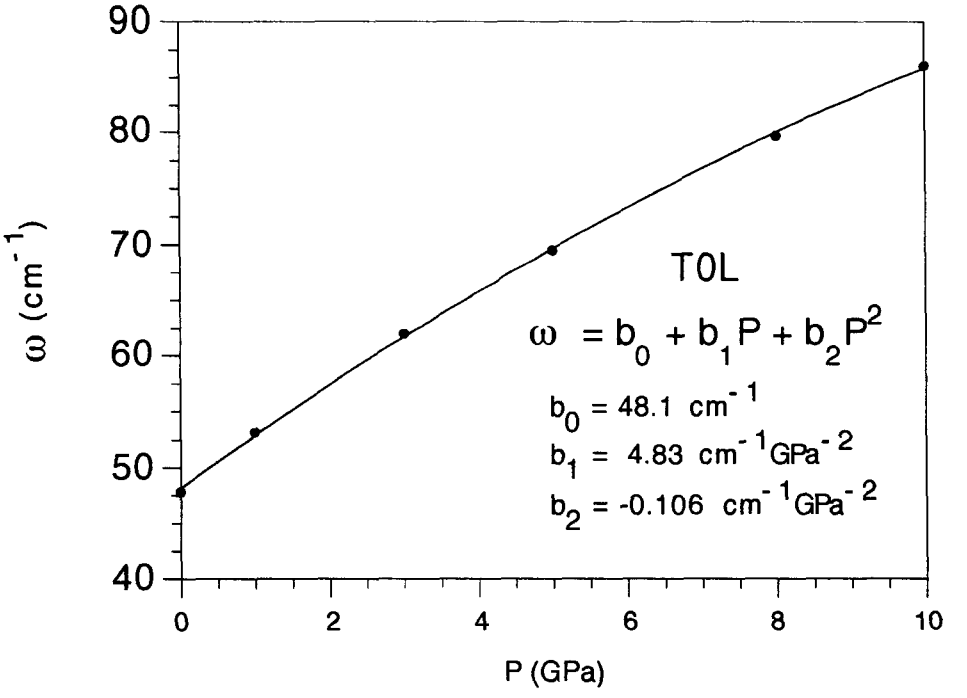

Fig. (4d), freqeuncy vs. pressure for the longitudinal mode of octahedral K

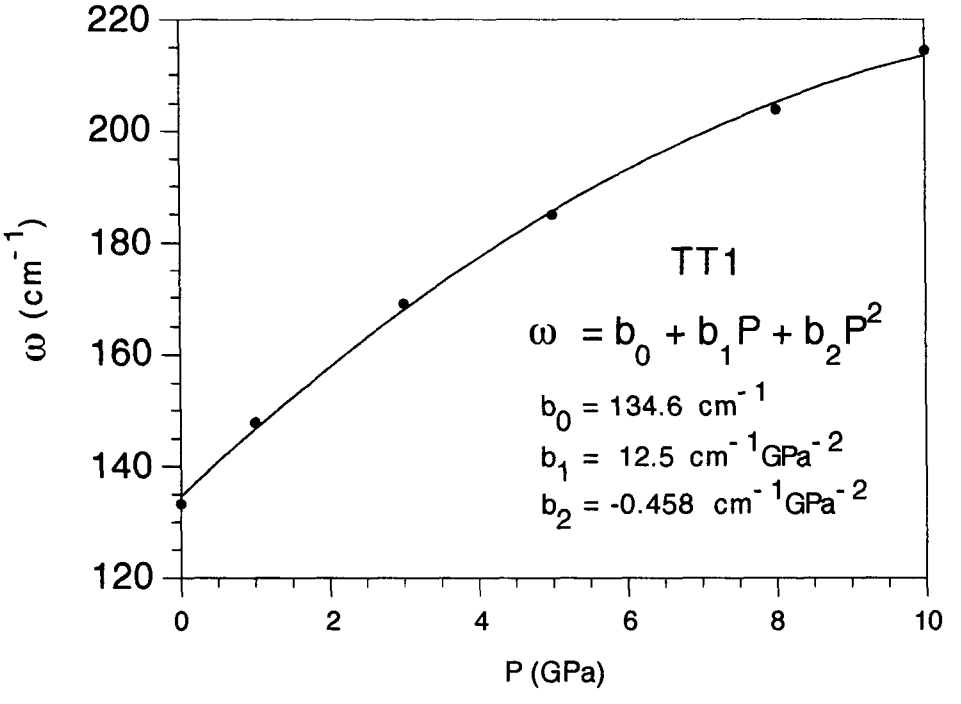

Fig. (4e), frequency vs. pressure for a tranverse mode of tetrahedral K

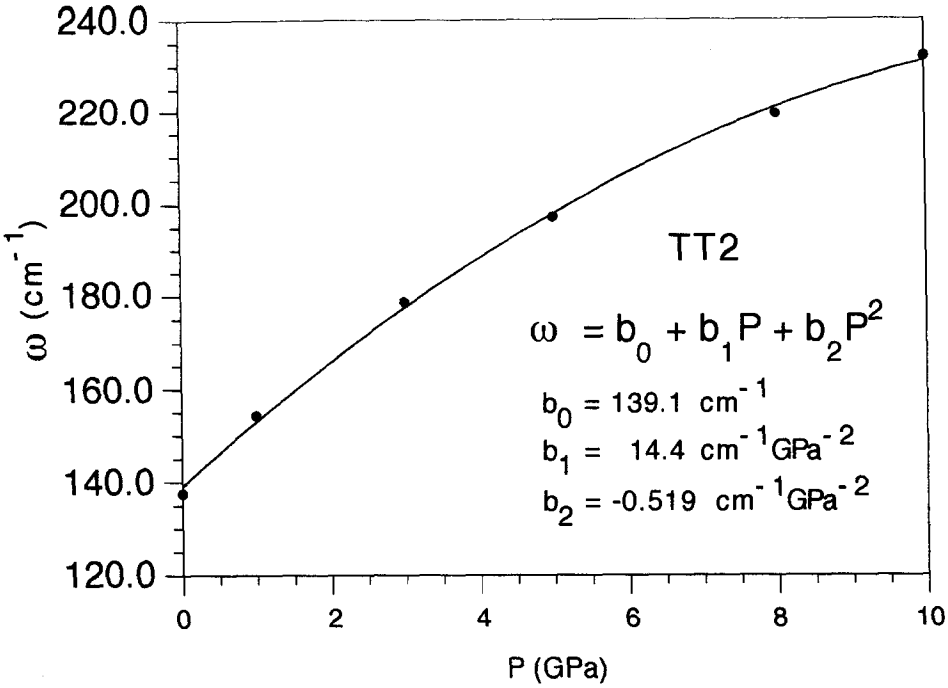

Fig. (4f), frequency vs. pressure for a tranverse mode of tetrahedral K

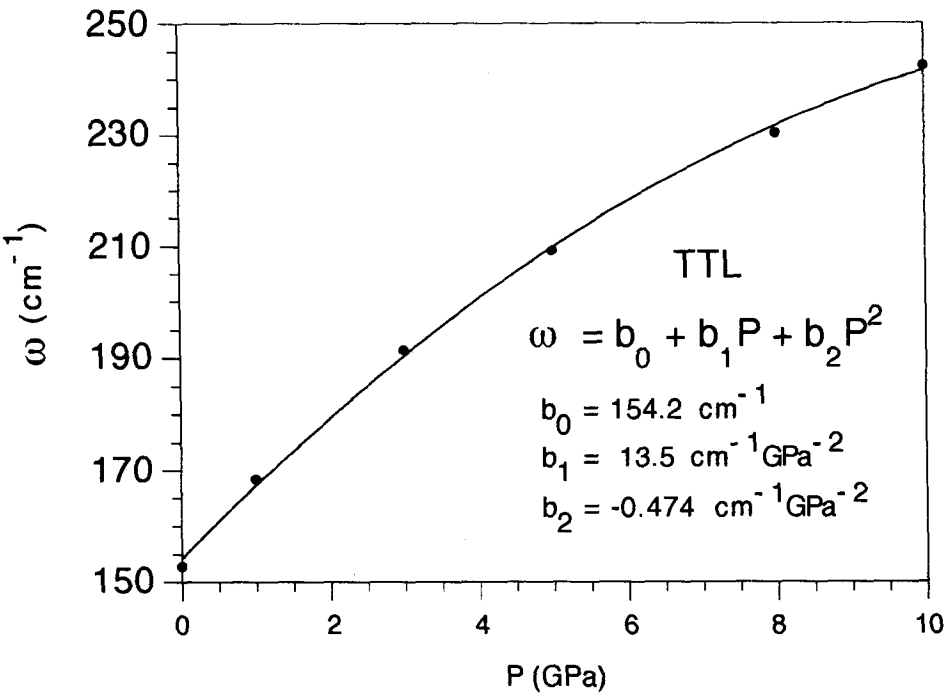

Fig. (4g), frequency vs. pressure for the longitudinal mode of tetrahedral K

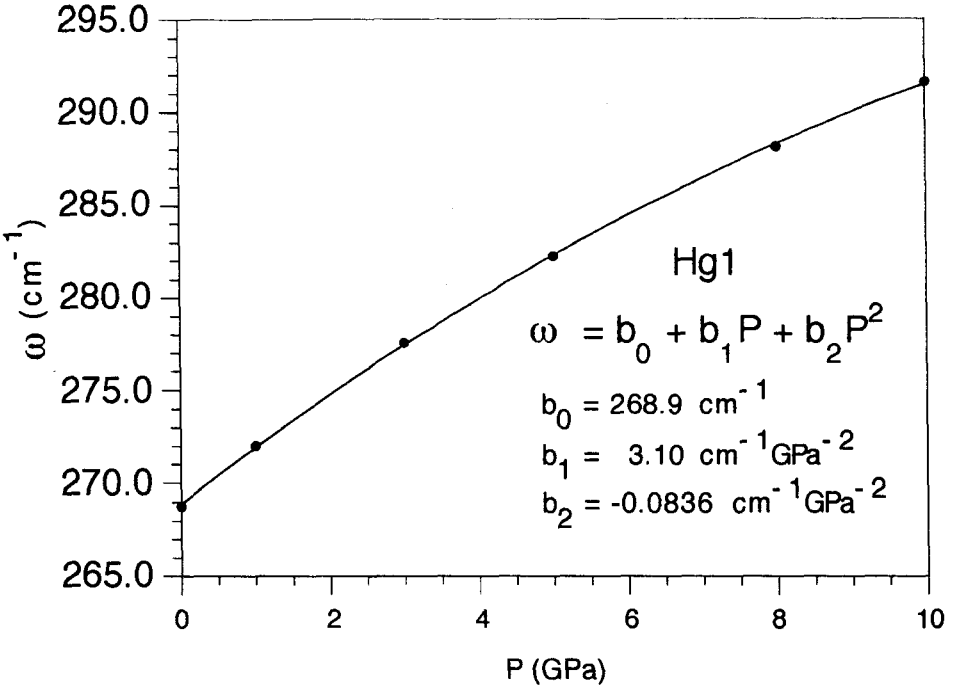

Fig. (4h), frequency vs. pressure for Hg(1)

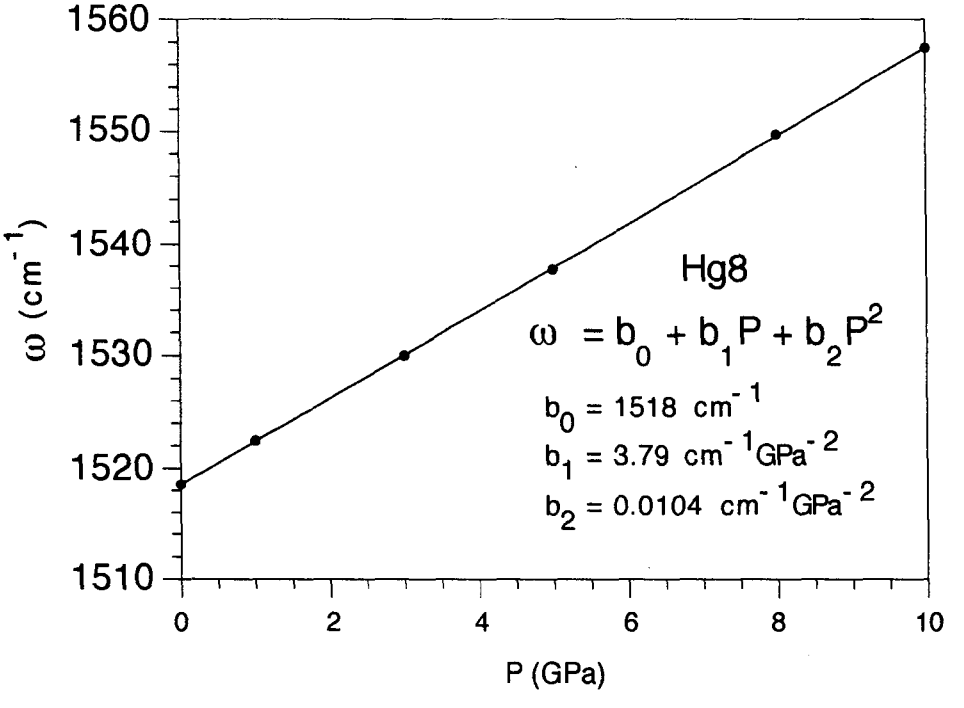

Fig. (4i), frequency vs. pressure for Hg(8)

In the following sections, first we develop a tight binding description of the conducting electrons based on a recent local density approximation calculation (LDA)[10]. Then we develop an accurate formalism to calculate the spectra function $\alpha^2(\omega)F(\omega)$, the electron-phonon coupling constants λ and therefore the transition temperature T_c. This uses the exact phonon eigenvectors and eigenenergies in combination with the localized Wannier orbital for describing electrons in the conduction band. We conclude that the phonon-mediated electron pairing may lead to superconducting phase of K_3C_{60} and that the main contribution to the electron-phonon coupling comes from the interaction between the conducting electrons and the low frequency intermolecular phonon modes of K_3C_{60}.

2.3.2 The Conduction Band

The electronic states of K_3C_{60} can be described in terms of K^+ and C_{60}^{3-} centers, with the conduction electrons on C_{60}. LDA[11] calculations showed that the LUMO of C_{60} is of T_{1u} symmetry (ie. p_x, p_y, p_z). We established the hopping matrix elements from one C_{60} molecule to its the nearest and the next nearest neighbor C_{60}, and carried out tight binding calculations to obtain the conduction bands. The Hamiltonian used for the electron hoppings is,

$$H_e = \sum_{i,j=1,3}^{nn} t_{ij}^{(1)} c_{mi}^{+} c_{nj} + \sum_{k=1,3}^{nnn} t_k^{(2)} c_{mk}^{+} c_{lk} \qquad (2)$$

where $t_{ij}^{(1)}$ and $t_k^{(2)}$ are the nearest and the next-nearest neighbor hopping matrix elements, respectively. In Fig. 5, we plot the various hopping channels between the nearest and the next-nearest neighbors. For hoppings between the nearest neighbors there are three channels with the hopping matrix elements t_1, t_2 and t_3 respectively; for hoppings between the next nearest neighbors we included only one channel with

its matrix element t_4 and ignored the rest of possible channels on the ground that the rest would be much less significant.

In calculations we adjusted the values of t_1, t_2, t_3 and t_4 to fit a recent local density approximation calculation[10] (LDA) on K_3C_{60} (the bandwidth $E_w = 0.6$ eV). the density of states at the fermi surface. The resulting electronic conduction bands and E_f of the tight binding scheme are in good agreement with those of LDA. We found that $t_1 = -0.0136$eV, $t_2 = -0.0068$eV, $t_3 = 0.0306$eV and $t_4 = -0.0055$eV, $E_f = 0.23$eV, and $N(0) = 11.5$ state/eV$-$spin$-C_{60}$ while the LDA gave $N^{LDA}(0) =$ 13.2 states/eV-spin-C_{60}[10]. In Fig. (6a) we plot conduction bands along $\Gamma \rightarrow X \rightarrow W \rightarrow L \rightarrow \Gamma \rightarrow K$; In Fig. (6b), we plot the density of states N(0) vs. energy and both are in good fit to the LDA[10].

Having determined the fermi surface, we can calculate the average fermi velocity v_f which is 9.9×10^6 cm sec^{-1} as compared to $v_f \approx 8 \times 10^6$ cm sec^{-1} resulting from an infrared reflectivity experiment[28] which take $2\Delta/K_BT_c \sim 5$. A LDA calculation[10] reported that $v_f = 1.8 \times 10^7$ cm sec^{-1}.

We have good descriptions of both phonons and conducting electrons and are ready to evaluate the static electron-phonon matrix. To do this, we need to develop a formalism which incorporates the available information of phonons and conducting electrons.

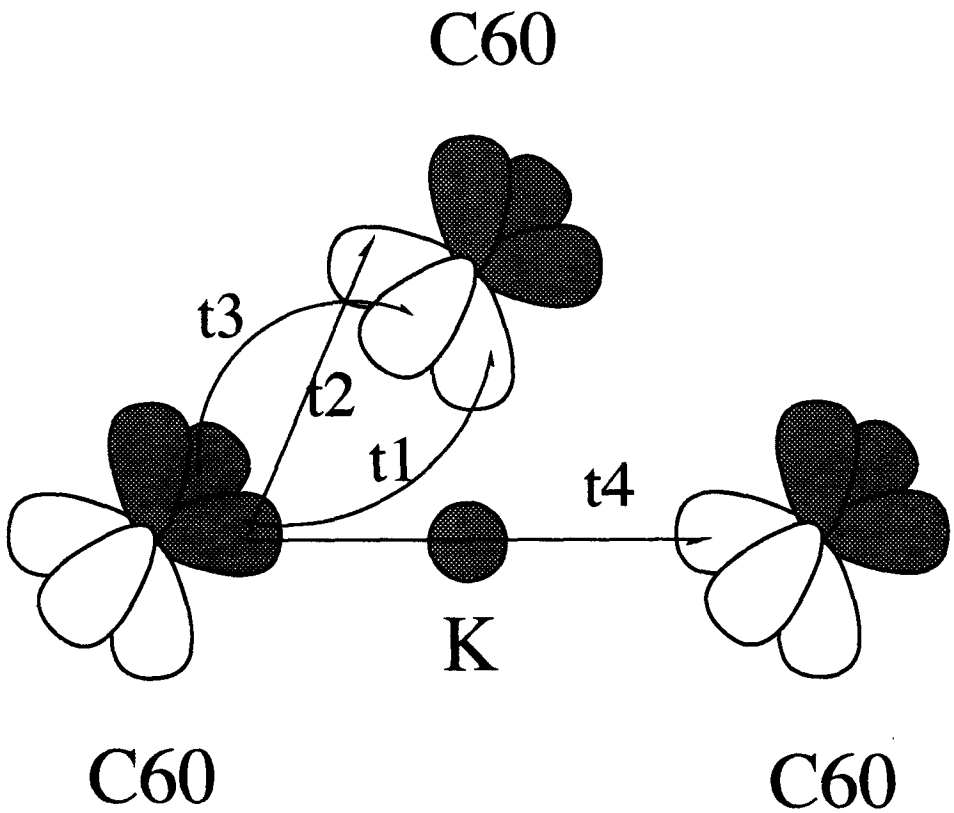

Fig. (5)

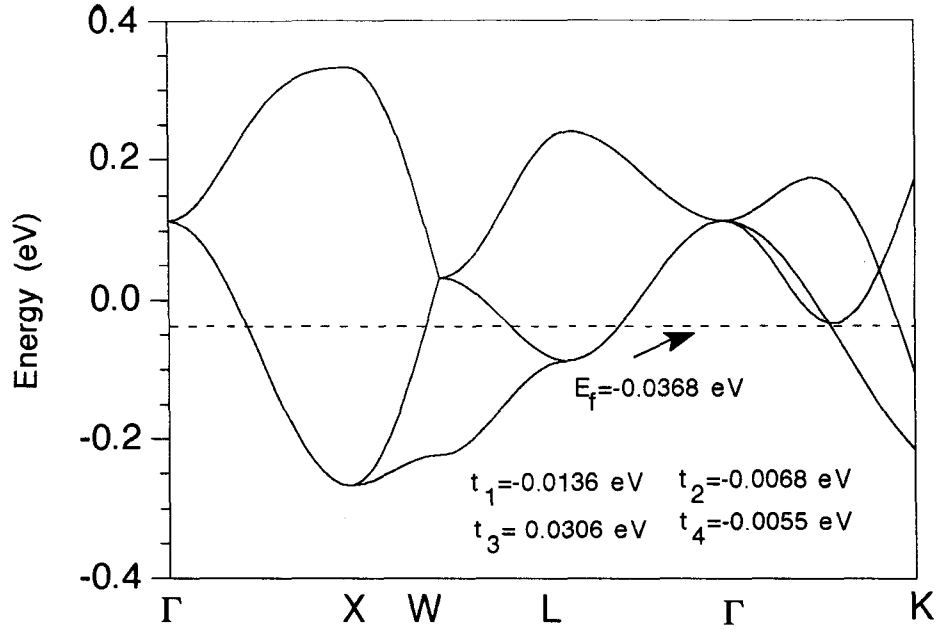

Fig. (6a), solid line is energy spectrum calculated from the tight binding scheme; and deshed line corresponds to the fermi energy.

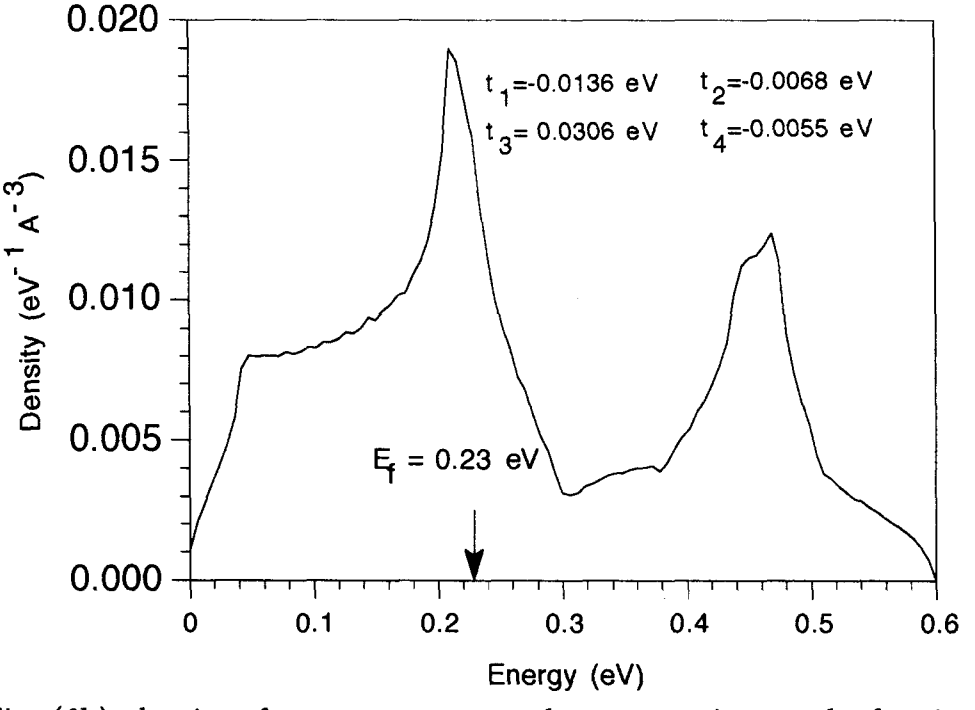

Fig. (6b), density of states vs. energy; the arrow points to the fermi energy.

2.3.3 Static Electron-Phonon Coupling

The total Hamiltonian is the following:

$$H = H_e + H_{ee} + H_{ph} + H_{eph}, \tag{3}$$

where H_e has been defined in Eq. (2), H_{ee} is the screened electron-electron coulomb repulsion,

$$H_{ph} = \sum_{k,j} \Omega_{kj}\, a^+_{kj} a_{kj} \tag{4}$$

is the phonon part of the Hamiltonian, and a^+_{kj} and a_{kj} are creation and annihilation operators of phonon of momentum $\mathbf{k}$, frequency Ω_{kj} and mode j, respectively.

$$H_{eph} = \sum_{l} \sum_{n\alpha} \Delta\mathbf{R}_{n\alpha} \cdot \bigtriangledown_{n\alpha} V_{ei}(\mathbf{r}_l - \mathbf{R}^{(0)}_{n\alpha}) \tag{5}$$

is the electron-phonon interaction, V_{ei} is the screened electron-ion coulomb interaction, $R^{(0)}_{n\alpha}$ is the equilibrium position of the αth ion in the nth unit cell, and $\Delta\mathbf{R}_{n\alpha}$ is the displacement of the ion.

$$\Delta\mathbf{R}_{n\alpha} = \sum_{kj} \sqrt{1/NM_\alpha}\, Q(\mathbf{kj}) e(\alpha|\mathbf{kj}) \hat{\xi}(\alpha|\mathbf{kj}) \exp(i\mathbf{k} \cdot \mathbf{R}^{(0)}_{n\alpha}) \tag{6}$$

$$Q(\mathbf{kj}) = \sqrt{\frac{\hbar}{2\Omega_{kj}}}\, (a^+_{-kj} + a_{kj}) \tag{7}$$

$$V_{ei}(\mathbf{r} - \mathbf{R}^{(0)}_{n\alpha}) = \int d^3\mathbf{q}/(2\pi)^3 \exp(i\mathbf{q} \cdot (\mathbf{r} - \mathbf{R}^{(0)}_{n\alpha}))\, V_{ei}(\mathbf{q}) \tag{8}$$

$$V_{ei}(\mathbf{r} - \mathbf{R}^{(0)}_{n\alpha}) = 4\pi e^2/(q^2 + q^2_{sc}) \tag{9}$$

where $q_{sc} = 1/R_{sc}$ and R_{sc} is the screen length of coulomb interaction.

The electron-phonon interactions may further be expressed in a tight binding picture as the following:

$$H_{eph} = \frac{1}{V^{1/2}} \sum_{k'kj} M_{k'kj}\, c^+_{k'} c_k (a^+_{-qj} + a_{qj}) \tag{10}$$

where,

$$M_{\mathbf{k'kj}} = -i \sum_{\mathbf{G},\alpha} \left(\frac{\hbar}{2\rho_\alpha \Omega_{\mathbf{qj}}}\right)^{1/2} e^{-i\mathbf{G}\cdot\mathbf{R}_\alpha} \hat{V}_{ei}(\mathbf{q}+\mathbf{G})\, e(\alpha|\mathbf{qj})\hat{\xi}(\alpha|\mathbf{qj})\cdot(\mathbf{q}+\mathbf{G})W(\mathbf{q}+\mathbf{G};\mathbf{k'},\mathbf{k}) \quad , \tag{11a}$$

$$W(\mathbf{q}+\mathbf{G};\mathbf{k'},\mathbf{k}) = \sum_{m,n=1}^{3} A_m^*(\mathbf{k'})A_n(\mathbf{k})\, U_{mn}$$
$$U_{mn} = \sum_i e^{-i\mathbf{k'}\cdot\mathbf{R_i}} < \psi_m(\mathbf{R_i})|e^{i(\mathbf{q}+\mathbf{G})\cdot\mathbf{r}}|\psi_n(0) > \quad , \tag{11b}$$

where $e^{-i\mathbf{G}\cdot\mathbf{R}_\alpha}\, e(\alpha|\mathbf{qj})\hat{\xi}(\alpha|\mathbf{qj})$ is a phonon eigenvector of momentum $\mathbf{q}$ ($\mathbf{q} = \mathbf{k'} - \mathbf{k}+$ is in the first Brillouin zone), $\mathbf{G}$ is a reciprocal lattice vector and $\mathbf{A(k)}$ is the electron eigenvector of momentum $\mathbf{k}$, $\mathbf{R}_\alpha$ is the equilibrium position of the αth atom in the unit cell and $\hat{V}_{ei}(\mathbf{q}) = \frac{N}{V}V_{ei}(\mathbf{q})$ (N is the number of unit cells in the volume V). Therefore,

$$\alpha_s^2(\omega)F_s(\omega) = \frac{1}{(2\pi)^3}\int \frac{\mathbf{d^2k}}{\mathbf{v_F}}\alpha_k^2(\omega)F_k(\omega) / \int \frac{\mathbf{d^2k}}{\mathbf{v_F}}$$
$$\alpha_k^2(\omega)F_k(\omega) = \frac{1}{(2\pi)^3}\sum_j \int \frac{\mathbf{d^2k}}{\mathbf{v_F}}|M_{\mathbf{k'kj}}|^2\,\delta(\omega-\Omega_{\mathbf{qj}}) \quad , \tag{12}$$

and the static coupling constant is,

$$\lambda_s = 2\int \alpha^2(\omega)F(\omega)\,\frac{d\omega}{\omega}, \tag{13}$$

where $\mathbf{v_F}$ is the average fermi velocity, $\mathbf{v_F} = \frac{1}{\hbar}\partial\epsilon_k/\partial k_\perp$, where $k_\perp$ is the momentum perpendicular to the fermi surface.

Two important average phonon frequencies $\omega_{s,log}$ and $\sqrt{<\omega_s^2>}$ are defined,

$$\omega_{s,log} = \exp\Big\{\frac{2}{\lambda}\int_0^\infty \frac{d\omega}{\omega}\alpha_s^2(\omega)F_s(\omega)\log\omega\Big\},$$
$$<\omega_s^2> = \frac{2}{\lambda}\int_0^\infty d\omega\,\alpha_s^2(\omega)F_s(\omega) \quad . \tag{14}$$

Their implications will be discussed in *Sec. 2.5.*

In our calculation one undetermined parameter is the screening length R_{sc}. We use the Thomas-Fermi length R_{TF} to estimate R_{sc}[29],

$$\begin{aligned} R_{TF} &= q_{TF} \\ q_{TF}^2 &= \frac{6\pi e^2 n_e}{E_f}, \end{aligned} \tag{15}$$

where n_e is the valence electron density and E_f is the fermi energy. The calculated value of R_{TF} is 0.63Å. It is short due to the fact that there are three valence electrons for each C_{60}. However the Thomas-Fermi picture is for free elecrtons, it may not be a good description for A_xC_{60}, in which conducting electrons mainly reside on C_{60} molecules.

2.3.4 Model

In our calculation, the conducting electrons are treated by the tight binding scheme described in *Sec. 2.2.4* with local orbitals of T_{1u} symmetry. Phonons are simulated by a force field developed by Guo *et al.*[8] using BIOGRAF as mentioned in *Sec. 2.2.1.* To calculate the static electron-phonon coupling constant λ_s, the local orbitals of T_{1u} symmetry are kept in their equalibrium positions and do not change as the lattice vibrates. However, since the orbitals of the conducting electron do change with the lattice vibrations, each C on a bucky ball C_{60} is seen to carry some negative charge q_c when we calculate the static electron-phonon coupling matrix between the conducting electron and C60 molecules. The charge on each K is +e.

2.3.5 Calculation Procedure

To calculate the electron-phonon matrix $\mathbf{M_{k'kj}}$, we need the eigenvectors and eigenvalues of phonons, the momenta and eigenvectors of electrons at the fermi surface. For phonons, we calculated all 189 vibration states for a $6 \times 6 \times 6$ mesh of the momentum $\mathbf{k}$ for the Brillouin zone (Of these modes 174 correspond to intra-atomic vibrational modes of the C_{60}, while the other 15 correspond to (i) three C_{60} translation modes; (ii) three C_{60} libration modes; (iii) three K_{oct} translational modes and (iv) six K_{tet} translational modes). We recorded these eigenvectors and eigenvalues with their corresponding momenta o for later use. The eigenvector and eigenvalue of phonon with momentum $\mathbf{q}$ is approximated by those of lattice site closest to $\mathbf{q}$ in the mesh.

For electronic states at the fermi surface, we store all the eigenstates and momenta of about 300 points around the fermi surface. For local Wannier wavefunctions we use three p-like Gaussian functions to describe three T_{1u} orbitals at a C_{60} site. For instance, $\psi_x \propto x e^{-\alpha x^2 - \beta(y^2+z^2)}$ (By choosing these particular forms, all the integrals may be worked out analytically), where $\alpha = 1/2R_\alpha^2$, $\beta = 0.693/R_\beta^2$, and ψ_x has its maximum value at $(x, y, z) = (R_\alpha, 0, 0)$ and decays to the half of its maximum value at $(x, y, z) = (R_\alpha, R_\beta, 0) = (R_\alpha, 0, R_\beta)$. By adjusting the values of R_α and R_β, we may tune positions and shapes of the local Wannier wavefunctions. In Fig. (7) we plot the values of a wavefunction ψ_x along the x-axis and y-axis respectively, setting $z = 0$, $R_\alpha = 3.55$ Å and $R_\beta = 3.55$ Å. We then orthogonalize the three orbitals up to the next-nearest neighbor in order to use the normal second quantization formalism.

After we have information of both phonon and electron at the fermi surface,

we evaluated $M_{\mathbf{k}'\mathbf{k}j}$ for each pair of momenta $\mathbf{k}', \mathbf{k}$ at the fermi surface for all phonon modes (j = 1,189). To estimate the coupling between the conducting electron and C_{60}, we set the charge on a C to its average value $-3/60 = -0.05$, which overestimates the charge each C carries (we will see later that this does not alter the overall picture). Then we summed them over according to Eq. (7) to get $\alpha^2(\omega)F(\omega)$ and therefore λ_s and T_c.

In our calculations, we use N(0) = 11.5 states/eV-spin-C_{60} for most cases to estimate the static electron coupling constant λ_s, except when we explicitly state the value of N(0) to be otherwise.

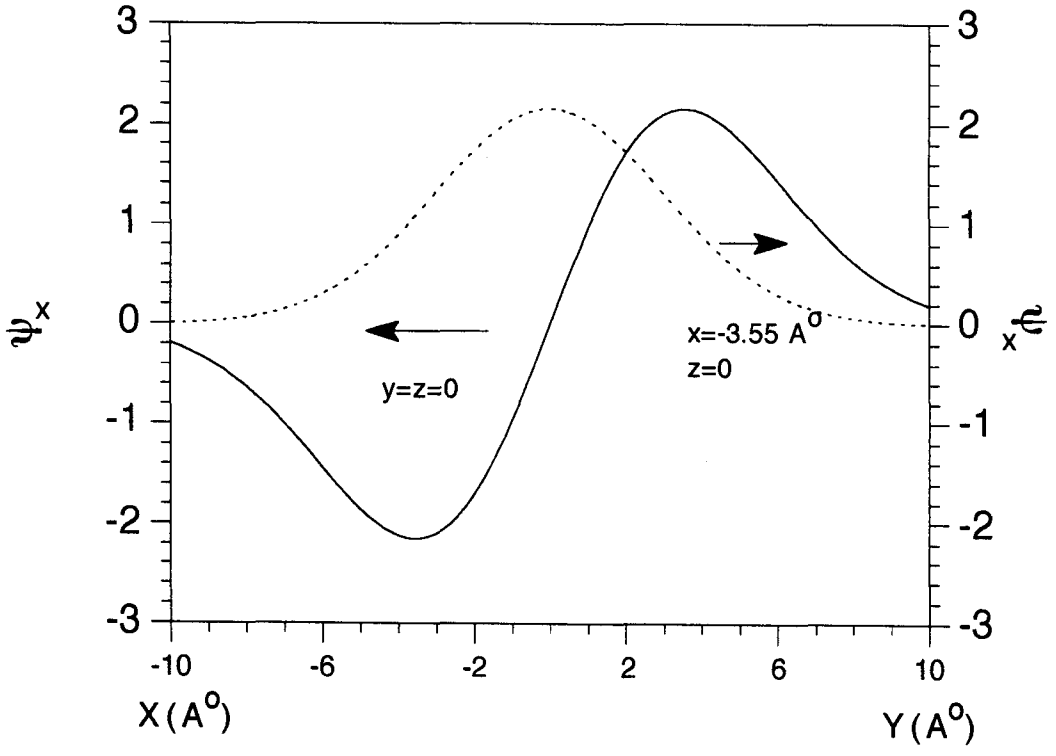

Fig. (7), solid line is for psi_x along x-axis (y=z=0);
dashed line is for for psi_x along y-axis (x=3.55 Å and z=0).

2.3.6 Results and Discussion

In Fig. (8a), (8b), we plot $\alpha^2(\omega)F(\omega)$ vs. ω for $t_1 = -0.0136eV$, $t_2 = -0.0068eV$, $t_3 = 0.0306eV$, $t_4 = -0.0055eV$, $R_\alpha = R_\beta = 3.55$ Å and $R_{sc} = 1$Å. Two peaks appear at low frequencies and their positions correspond to $\omega_1 \approx 20 - 40$ cm^{-1}, which are the frequencies of the libration modes of K_3C_{60} and vibration modes of octahedral site K, and $\omega_2 \approx 130 - 150$ cm^{-1} which are the frequencies of the vibration modes of tetrahedral K. In Fig. (8b), we plot $\alpha^2(\omega)F(\omega)$ vs. ω for ω up to $1600cm^{-1}$. At $\omega > 200cm^{-1}$, $\alpha^2(\omega)F(\omega)$ is apparently negligibly small. This result suggests that contributions to the static coupling constant come mainly from the couplings between electrons and phonons at low frequencies. Those phonons are the low frequency intermolecular vibrational modes rather than the high frequency intramolecular vibrations.

To further identify the sources of contributions, we set the charge on C to zero when we estimated $\alpha_s^2(\omega)F_s(\omega)$, which neglect the interaction between conducting electron and C_{60}, and we plot the results in Fig. (8c). Again, peaks occur at low frequencies similar to the previous case and the magnitudes of the first and second group of peaks has no noticeable changes. These results indicate that the main contributions to the static electron-phonon couplings and hence superconductivity, come from the alkali atoms A. The low frequency vibrations of C_{60} contribute less significantly to the superconductivity of K_3C_{60}. This is due to the fact that the mass of C_{60} is much larger than that of A and the contributions from carbons at different sites are mutually cancelled.

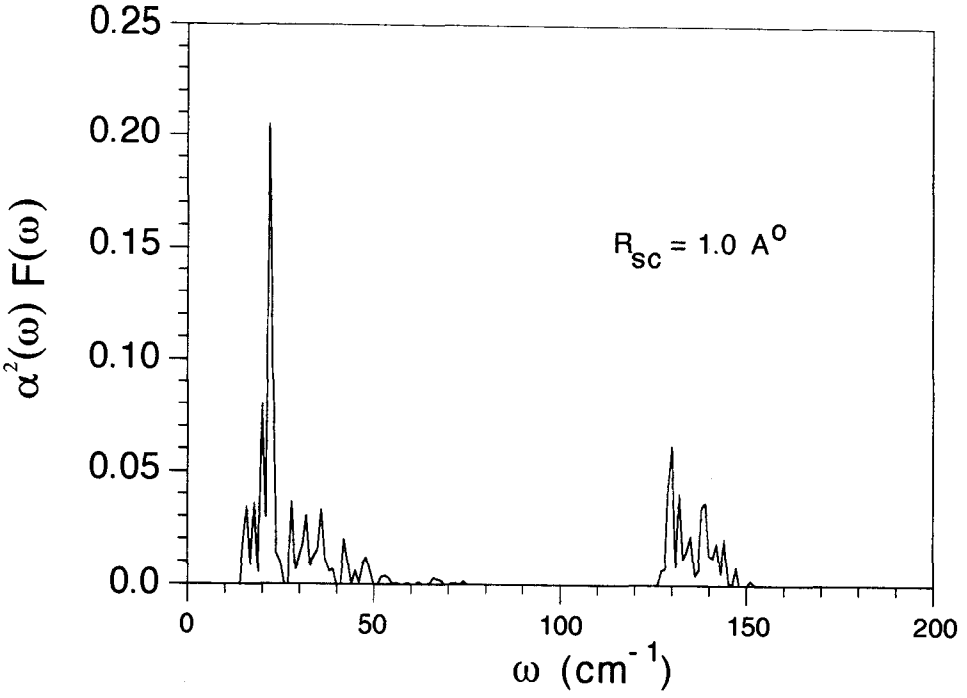
0.25
0.20
0.15
0.10
0.05
0.0
$\alpha^2(\omega)$ F(ω)
R_{sc} = 1.0 A^o
0
50
100
150
200
ω (cm^{-1})

Fig. (8a)

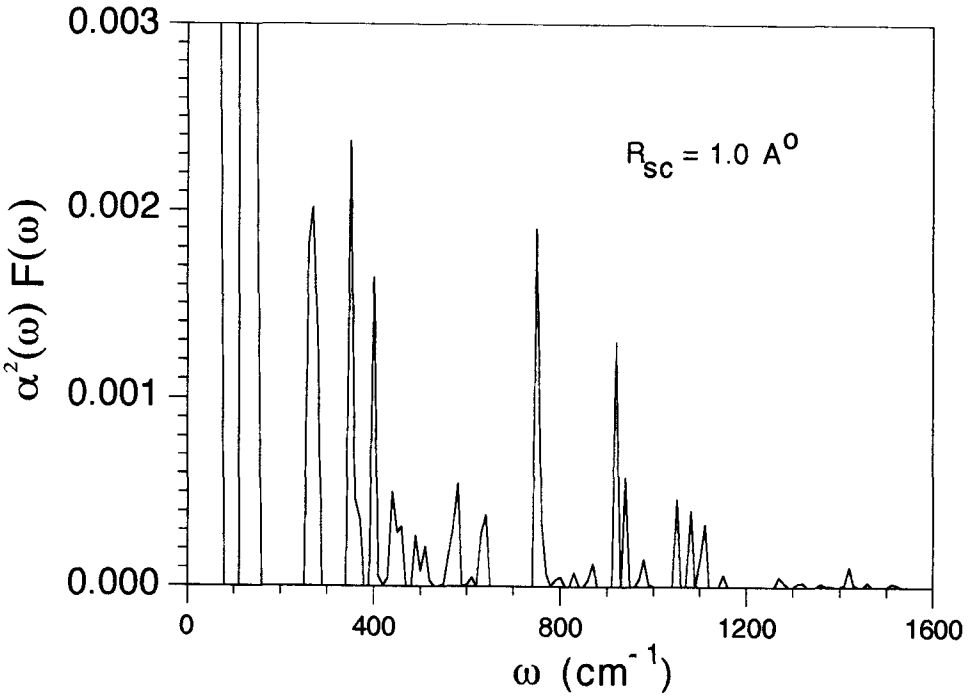
0.003
0.002
0.001
0.000
$\alpha^2(\omega)$ F(ω)
R_{sc} = 1.0 A^o
0
400
800
1200
1600
ω (cm^{-1})

Fig. (8b)

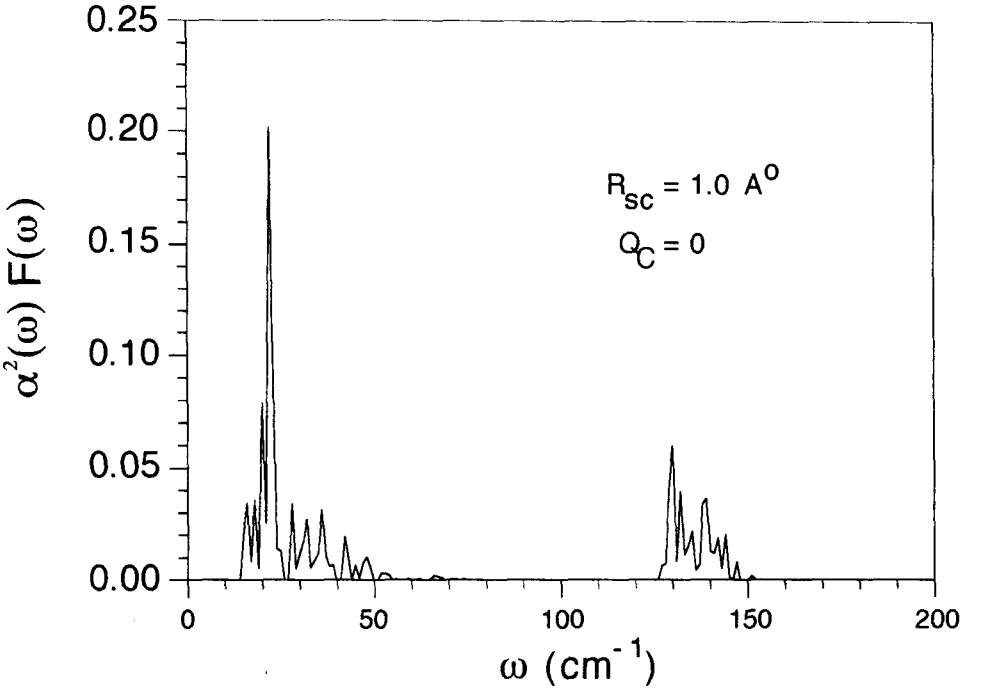

Fig. (8c)

To investigate the sensitivity of various parameters, we varied α, β and the screen length R_{sc} with $t_1 = -0.0136$eV, $t_2 = -0.0068$eV, $t_3 = 0.0306$eV and $t_4 = -0.0055$eV. Table 6 lists the values of λ_s, μ_s^*, $\omega_{s,\log}$, $\sqrt{<\omega_s^2>}$, and the screening length R_{sc} for K_3C_{60}. λ_s depends strongly on R_{sc} and increases monotonically with R_{sc}. When $R_{sc} = 2$Å, $\lambda_s = 5.46$, corresponding to a very strong coupling; and at $R_{sc} = 1$Å, $\lambda_s = 1.15$, a modest pairing. In any case, λ_s depends strongly on the screen length R_{sc}. λ_s also depends on the positions and shapes of local orbitals, *i.e.*, depends on the values of R_α and R_β. This is because R_α and R_β determine the relative distances between the conducting electrons and ions. However, we do not expect the value of λ_s to depend on R_α and R_β as much as R_{sc}. This is indeed the case. Table 7 lists the λ_s's dependence on α and β.

Table 6. R_{sc} Dependence of some Superconducting Properties†

R_{sc}(Å)	$\omega_{s,log}$	$\sqrt{<\omega_s^2>}$	lambda$_s$
0.50	28.7	52.3	0.13
0.63	28.5	51.3	0.28
0.80	28.2	50.2	0.60
1.00	27.9	49.0	1.15
2.00	27.1	45.8	5.46
4.00	26.4	43.3	14.50
8.00	26.0	42.0	26.82

† $\omega_{s,log}$ and $\sqrt{<\omega_s^2>}$ are in units of cm^{-1}; N(0) = 11.5 states/eV-Spin-C_{60}.

Table 7. Dependence of some Superconducting Properties on local orbitals†

R_α(Å)	R_β(Å)	R_{sc}(Å)	$\omega_{s,log}(cm^{-1})$	λ_s
3.00	3.80	10.0	26.1	5.42
3.55	3.55	10.0	25.9	5.06
3.45	3.45	14.2	25.9	6.28
3.55	3.55	14.2	25.9	6.25
3.65	3.65	14.2	25.9	6.18

† N(0) takes the result of a photoemission experiment[7], which is 1.9 states/eV-spin-C_{60}.

It is clear that the intermolecular modes contribute to the static electron-phonon couplings far greater than the intramolecular modes. Hence the intermolecular modes play a dominant role in the static electron-phonon coupling of alkali C_{60} compounds. Although peaks at $\sim 20 - 40$ cm^{-1} are higher than those at $\sim 130 - 150$ cm^{-1} in Fig. (8), we should not conclude that most of the contribution to the electron-phonon coupling comes from phonons at ~ 30cm^{-1} due to the limitations of the current model. One such limitation is that we do not include A-s orbitals in our tight-bind approximation. It changes the relative contributions to the static coupling constant λ_s from both octahedral and tetrahedral alkali atoms.

The screen length R_{sc} is a very important parameter and needs to be investigated. If $N(0) \approx 10 - 20$ states/eV-spin-C_{60}, there is no question that the coupling between the conducting electrons and the intermolecular phonon modes plays a very important role in the superconductivity mechanism of these materials.

2.3.7 Conclusion

Our finding shows an important role that the alkali atoms play in the superconductivity of the alkali fullerence : 1) The contributions to the static electron-phonon coupling come mostly from the low frequency intermolecular phonon modes; 2) The alkali atoms contribute more significantly to the static electron-electron pairing than C atoms; 3) because of its magnitude, the static electron-phonon no doubt plays an important role in the superconductivity of these systems. Any mechanism explaining the superconductivity of M_xC_{60} can not neglect the significant roles of the alkali atoms and the low frequency phonon modes.

2.4 Dynamic Electron-Phonon Couplings

2.4.1 Symmetry and Electron-Intramolecular Phonon Couplings

Local density approximation (LDA)[11], and MNDO calculations[30] have revealed that the lowest unoccupied molecular orbitals(LUMO) are of T_{1u} symmetry, *i.e.*, p-like orbitals. These orbitals are subject to Jahn-Teller effects. Let us turn to the character table, to find out to which phonon modes these orbitals couple.

The symmetry group of C_{60} is the icosahedral group I_h. The corresponding character table is the following[31]:

Table 8. Character Table of the Icosahedral Group I_h

I_h	E	$12C_5$	$12C_5^2$	$20C_3$	$15C_2$
A	1	1	1	1	1
T_1	3	$\frac{1}{2}(1+\sqrt{5})$	$\frac{1}{2}(1-\sqrt{5})$	0	-1
T_2	3	$\frac{1}{2}(1-\sqrt{5})$	$\frac{1}{2}(1+\sqrt{5})$	0	-1
G	4	-1	-1	1	0
H	5	0	0	-1	1
$T_{1u} \bigotimes T_{1u}$	9	$\frac{1}{2}(3+\sqrt{5})$	$\frac{1}{2}(3-\sqrt{5})$	0	1

The characters of $T_{1u} \bigotimes T_{1u}$ are obtained by the direct product of the original two characters. Two ways to decompose $T_{1u} \bigotimes T_{1u}$ are given below.

(i) By the theorem of orthonormality, $\sum_i \frac{n_i}{n_G} \chi_\mu^{\dagger i} \chi_i^\nu = \delta_\mu^\nu$, where $n_G = 60$, is the order of the icosahedral group; n_i is the number of elements in the class i; μ, ν are labels for inequivalent, irreducible representations of I_h; χ_i^μ is the character of class i elements in the μ-representation, we conclude that

$$T_{1u} \bigotimes T_{1u} = A_g \bigoplus T_{1g} \bigoplus H_g. \tag{16}$$

(ii) Summing over the characters of A, T_1 and H, we get exactly the characters of $T_{1u} \bigotimes T_{1u}$. And it is the only choice. Since $u \bigotimes u = g$, we again obtain Eq. (16).

From the above discussion, we know that electrons in LUMO bands couple to A_g, T_{1g} and H_g phonon modes. A_g is the symmetric breathing mode, T_{1g} is a rotational mode, and H_g is a quadrupolar vibrational mode. A_g modes change the local energy level but do not lift the degeneracy. T_{1g} is antisymmetric while Hamiltonian H is real and the LUMO of symmetry T_{1u} can be chosen to be real functions. According to selection rules[32], electrons at LUMO can not couple to the T_{1g} intramolecular modes in the first order. H_g modes split the degeneracy of three T_{1u} orbitals. This is the so-called Jahn-Teller effect; electrons at LUMO couple with these H_g modes in the first order. We will study the couplings between electrons at LUMO of T_{1u} symmetry and two A_g and eight H_g modes in the following sections.

In the crystal, C_{60} molecules are distorted. They no longer have I_h symmetry. However, the above conclusions remain valid. For the structure of a single orientation of C_{60} molecules, it results in a point-group symmetry of T_h within a FCC lattice[23]. It is easy to show by symmetries that A and T symmetry of I_h group remain the same in the T_h symmetry group while G splits to $A \bigoplus T$ and $H \rightarrow E \bigoplus T$. Hence, in this case T_{1u} electronic orbitals couple with A_g, E_g and T_g phonon modes. Because the distortions of the C_{60} molecules are very small, There should be no noticeable quantitative difference between a C_{60} molecule in gas and one in crystal. It follows that studying the structure and behavior of the former will help us elucidate those of the latter, which should be very similar if not the same.

Fig. (9) lists the vibrational modes of two A_g modes and eight H_g modes.

These are obtained by BIOGRAF and are plotted at the initial time t = 0 with SCALE = 20. Arrows stand for the displacements of carbon atoms.

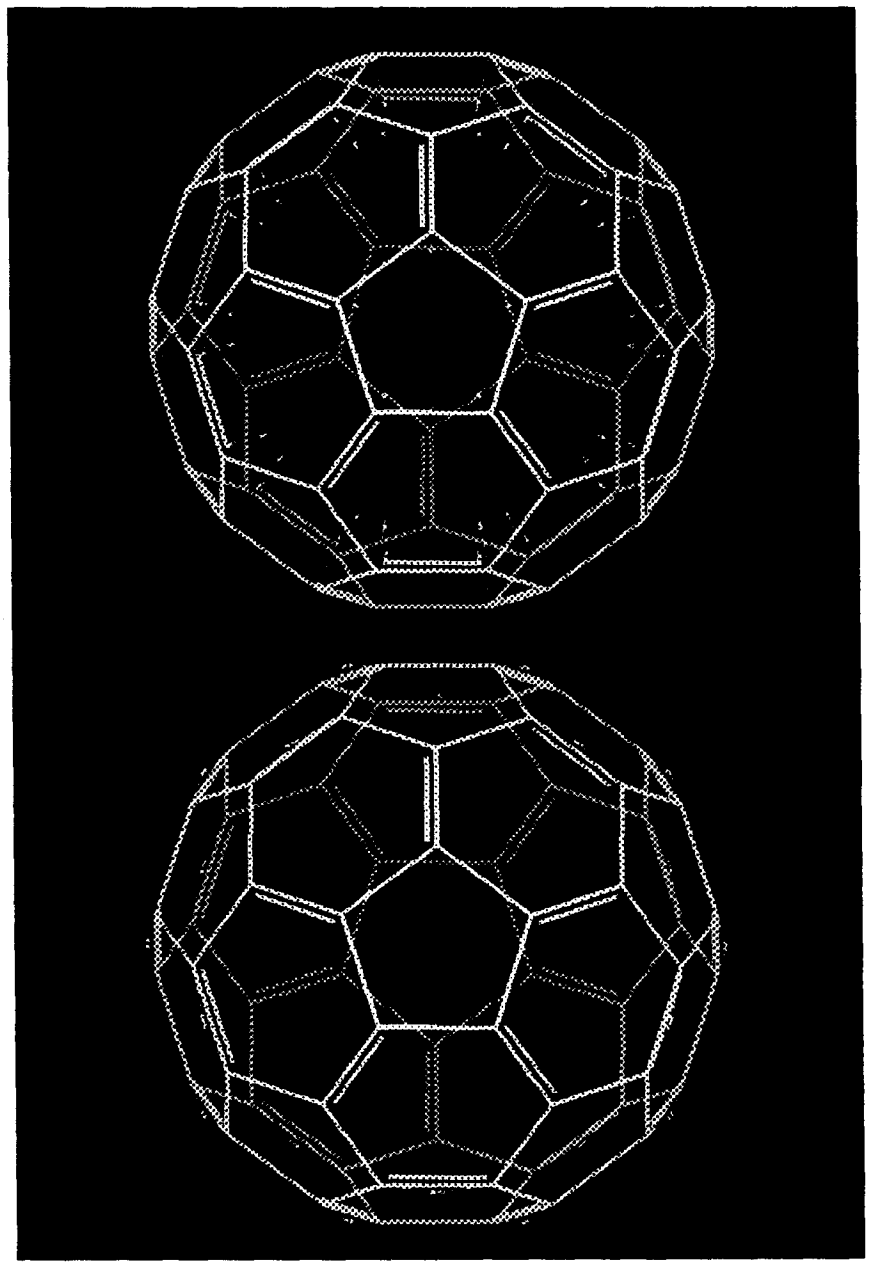

Fig. (9ab), (a) Ag(1); (b) Ag(2).

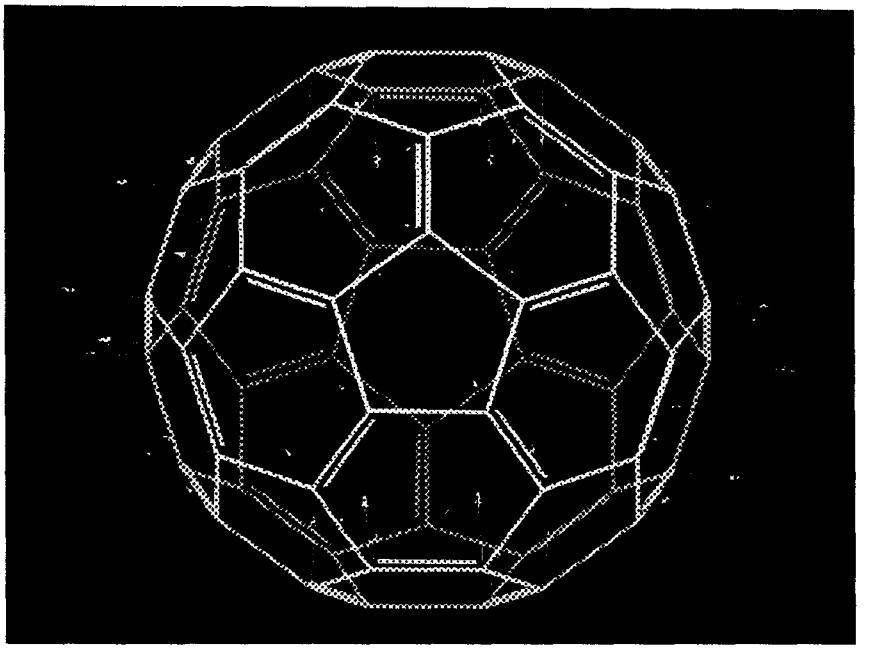

Fig. (9c), Hg(1)

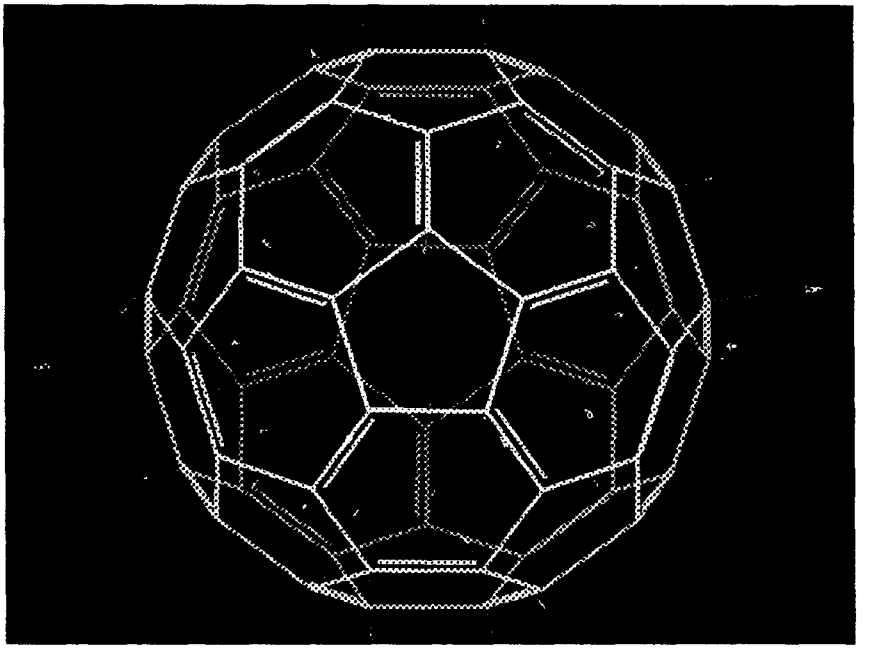

Fig. (9d), Hg(2)

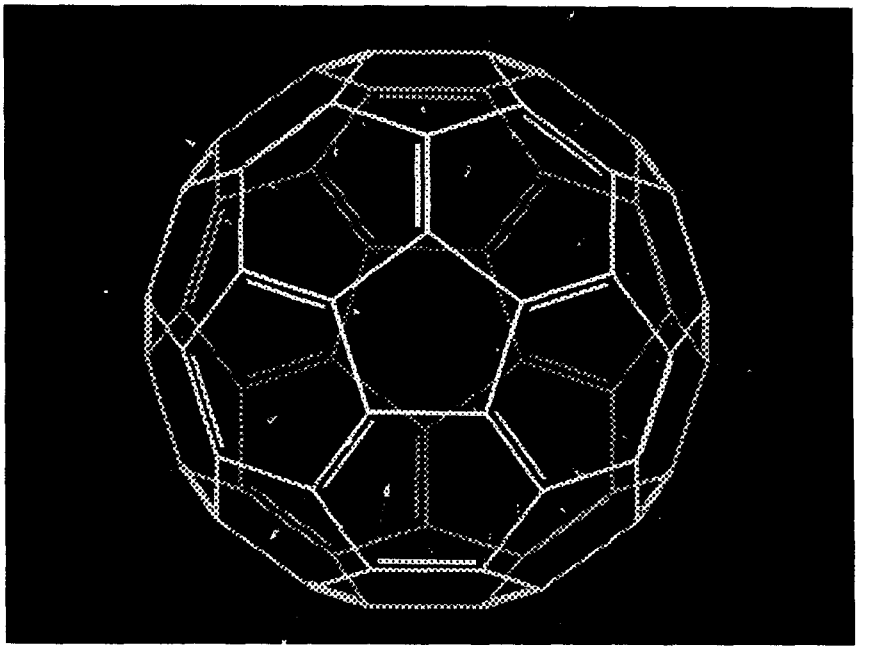

Fig. (9e), Hg(3)

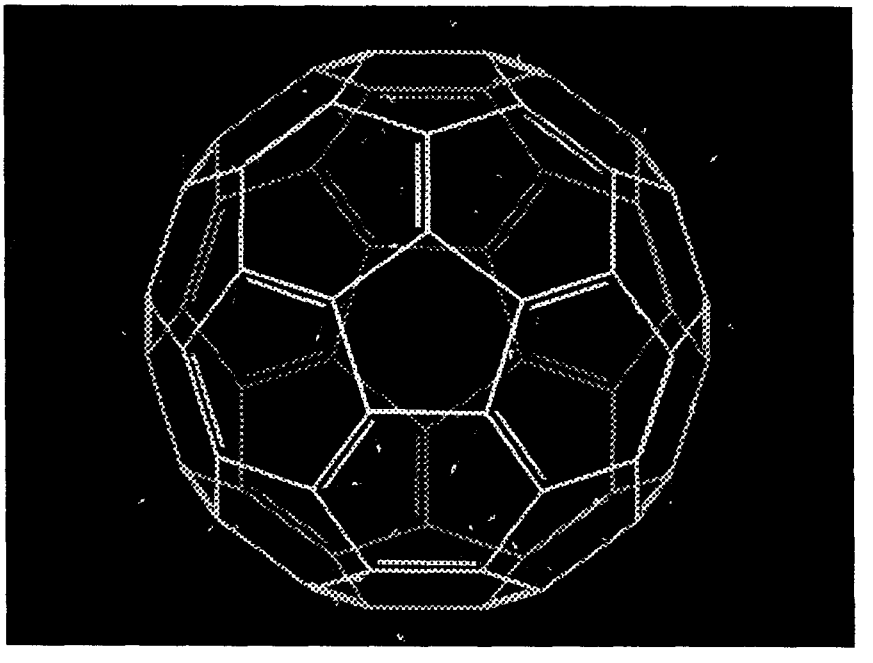

Fig. (9f), Hg(4)

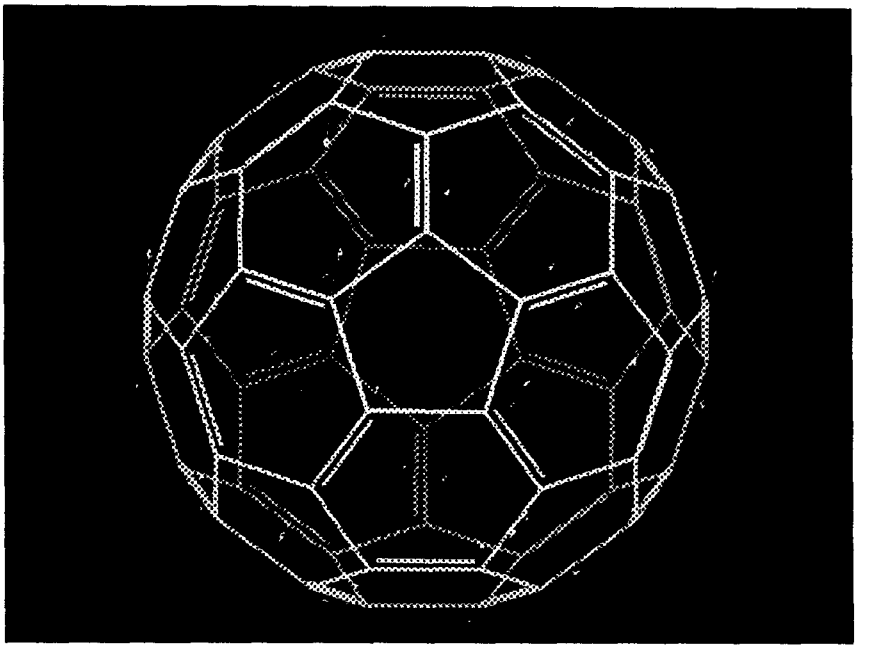

Fig. (9g), Hg(5)

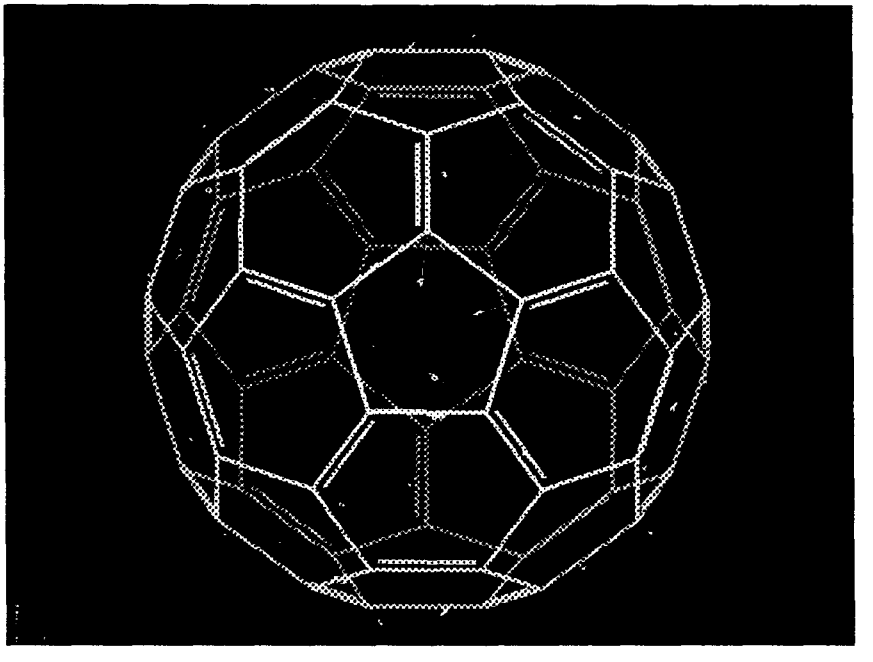

Fig. (9h), Hg(6)

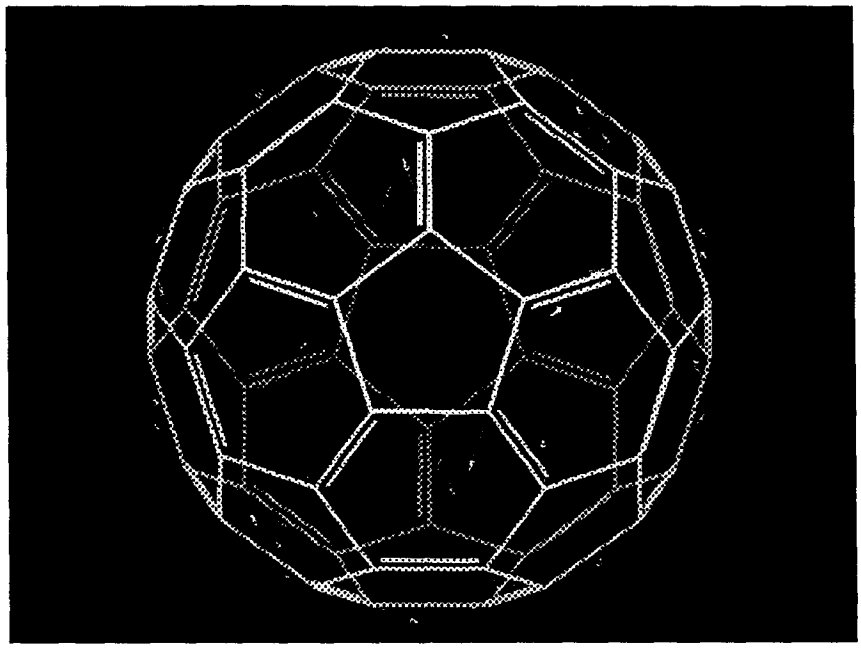

Fig. (9i), Hg(7)

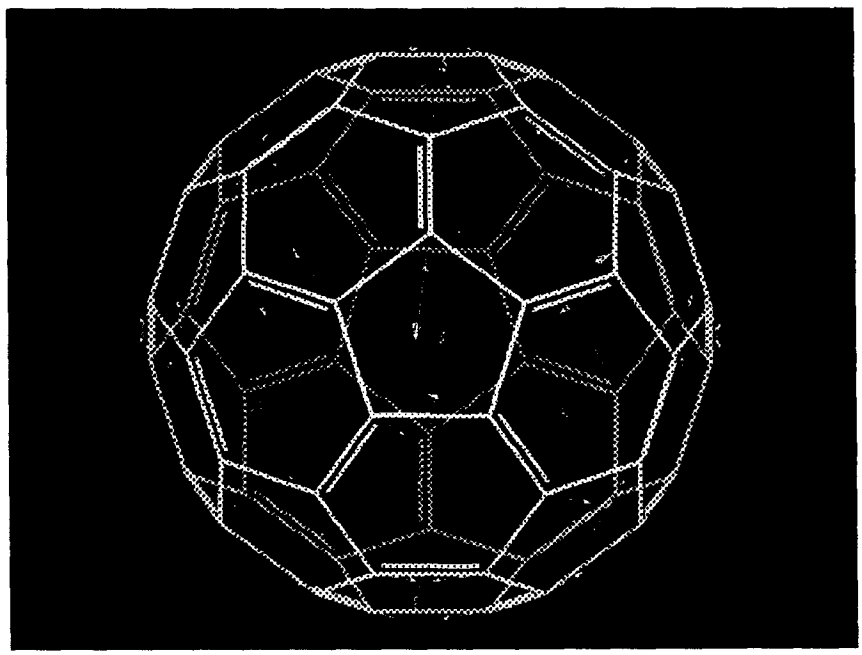

Fig. (9j), Hg(8)

2.4.2 Jahn-Teller Effects and Superconductivity

Several groups[4,33,34] have proposed that the Jahn-Teller effects caused by couplings between LUMO electrons and the intramolecular phonon modes are responsible for the superconductivity in these systems. According to *Sec. 2.3.1*, Only H_g modes are relevant to superconductivity. There are eight H_g modes. So 40 out of 174 intramolecular vibration modes of C_{60} can split the three degenerate T_{1u} electronic states. The Hamiltonian for such processes is the following[4]:

$$H_{ij} = \bar{E} + \sum_{m,\mu} h_{ij}(m,\mu) Q_{m,\mu} + H_{vib}, \tag{17}$$

where $i,j = 1,2,3$ are the index for the three degenerate T_{1u} electronic states, $Q_{m,\mu}$ is the normal coordinate of the m-th H_g mode with degeneracy $\mu = 1...5$, and H_{vib} is the Hamiltonian of the vibrations. E is the total energy of undistorted C_{60}; h_{ij} is the coefficient of the coupling matrix. For this particular case, the coupling matrix is[4,32,35]

$$\frac{1}{2} g_m \begin{pmatrix} Q_{m,5} - \sqrt{3}Q_{m,4} & -\sqrt{3}Q_{m,1} & -\sqrt{3}Q_{m,1} \\ -\sqrt{3}Q_{m,1} & Q_{m,5} + \sqrt{3}Q_{m,4} & -\sqrt{3}Q_{m,3} \\ -\sqrt{3}Q_{m,2} & -\sqrt{3}Q_{m,3} & -2Q_{m,5} \end{pmatrix}. \tag{18}$$

where g_m is the rate of energy change with respect to displacement of the m-th mode. $Q_{m,5}$ is the d_z-like mode while $Q_{m,\mu}, \mu = 1...4$ are $d_{x^2-y^2}$, d_{xy}, d_{yz} and d_{zx} like modes. Eq. (18) tells us that the form of splitting depends on the character of phonons. For $\mu = 5$, the splitting is the following[4]:

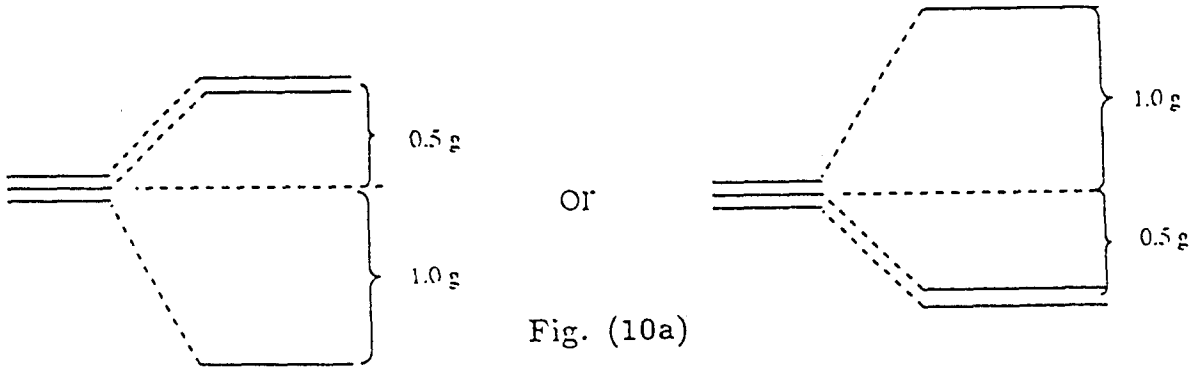

Fig. (10a)

While for $\mu = 1 - 4$, the splitting has the following form,

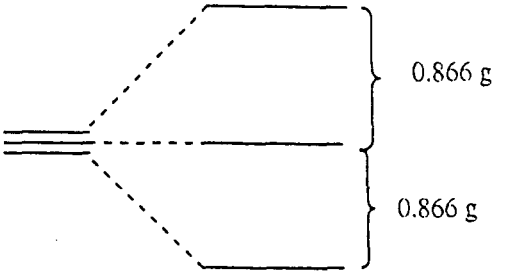

Fig. (10b)

Therefore, C_{60}^{-} and C_{60}^{2-} are the first order Jahn-Teller active. The situation is a little more complicated for C_{60}^{3-}. The S = 3/2 state of C_{60}^{3-} is not Jahn-Teller active while the S = 1/2 state is. Just as is the static electron-phonon coupling, the dynamic Jahn-Teller electron-phonon coupling constant λ_d, according to Ref. [4,34], is given by

$$\begin{aligned} \lambda_{d,m} &= \frac{5}{6}\frac{N(0)}{M\omega_m^2} g_m^2, \\ \lambda_d &= \sum_m \lambda_{d,m}. \end{aligned} \tag{19}$$

Varma, Zaanen and Raghavachari[4] have studied the Jahn-Teller effects of a C_{60} using MNDO technique. However, their MNDO phonon frequency does not fit those of the experimental values well, and they didn't study the electron couplings with A_g modes. Here we present a thorough study of the electron phonon couplings on a C_{60}. We use MNDO to calculate g_m. Two important average phonon frequencies $\omega_{d,log}$ and $< \omega_d^2 >$ are

$$\begin{aligned} \omega_{d,log} &= \exp\left(\frac{\sum_m \lambda_{d,m} \log\omega_m}{\lambda_d}\right), \\ < \omega_d^2 > &= \frac{1}{\lambda_d}\sum_m \lambda_{d,m}\omega_m^2. \end{aligned} \tag{20}$$

2.4.3 Calculation Procedure

Let us concentrate on C_{60}^-. To eliminate other contributions to energy changes, we take the optimized MNDO structure of C_{60}^- (which is obtained by the technique described in *Sec 2.2.1*), use BIOGRAF calculate its vibrational modes, and record its distorted structures with different vibrational amplitudes of eight H_g and two A_g modes onto disk at the initial time t = 0. Then we read out these data, transform them into the MNDO input files, and use MNDO to calculate the energies of the optimal structure and various distorted structures with an extra electron. Finally, we fit the energies to the following formula[4]:

$$E = -c\, g_m Q_m + k_m Q_m^2/2 \tag{21}$$

where k_m is the spring constant of mode m; for d_z-like mode, c = 1; while for other modes, $c = \sqrt{3}/2 = 0.866$. Since our vibration mode from BIOGRAF is a mix of five, we take the average value of c = 0.9.

As illustrated in Fig. (10), three degenerate single electronic energies at LUMO split into either three different energies or one energy and two degenerate ones. Because the splittings are proportional to g_m, we have another way of calculating g_m. The total splitting is $\sqrt{3}g_m$ in Fig (10a), and $1.5g_m$ in Fig. (10b). We examined the energy splitting of LUMO for C_{60}, from which we calculate g_m. In the calculation we take the average values for the total splittings of mode m,

$$\Delta_m = 1.7 g_m. \tag{22}$$

We will compare the values of g_m by two methods.

After we obtain g_m, m = 1 − 8, we use Eq. (19) to calculate the dynamic coupling constant λ_d. In the present case,

$$M\omega_m^2 = 4.452 \times 10^{-5}\omega_m^2 \text{ eV} \cdot \text{Å}^2. \quad (23)$$

$$\lambda_{d,m} = 1.8718 \times 10^4 N(0)\, g_m^2/\omega_m^2. \quad (24)$$

2.4.4 Results

To illustrate the quality of our calculations, we calculate the frequencies of the neutral C_{60} as in Ref [4]. Results are listed in Table 9. Because the geometry of our C_{60} is slightly different from that of Ref. [4], there are slight differences for some of the modes. This demonstrates the consistency of both our and Ref. [4] MNDO calculations. In fitting Eq. (21), we obtain the values of k_m for eight H_g modes and two A_g modes, from which we can calculate their corresponding frequencies by the following formula:

$$\omega_m = \sqrt{\frac{k_m}{M}}. \quad (25)$$

The results are also listed in Table 9. Compared with the frequencies of MNDO calculations, deviations are less than 5% for a majority of the cases and 15% in the worst case. The reasons are the following : 1) as described in *2.4.3* the vibration distorted structures are obtained by the force field method; thus, the vibrational modes of force field by BIOGRAF are not exactly the same as those of MNDO calculations, and there are some mixings between different modes; 2) MNDO is a generic code and therefore is difficult to control. In our calculation, the MNDO program picks its own starting points in every case. There is always the danger that it converges to the excited states. Because of the mixings and inherent features of MNDO, we are not able to fit Eq. (21) to our satisfaction in some cases and we

can not even fit the lowest two modes at all, Fig. (11). On the other hand, the fitted frequencies of two A_g modes are remarkably close to the values of MNDO in spite of the uncertainty of MNDO itself. It is because the freqencies of two A_g modes are far apart such that the two modes have little mixing. In any case our calculations should be accurate enough to reveal information about the dynamic electron-phonon couplings.

Table 9. Comparison of the Vibrational Frequencies (cm^{-1})

mode	Fitting Eq. (21)	Ours MNDO†	Ref. [4]
$H_g(1)$	*	263	263
$H_g(2)$	*	447	447
$H_g(3)$	814	706	711
$H_g(4)$	1000	924	924
$H_g(5)$	1354	1260	1260
$H_g(6)$	1460	1407	1406
$H_g(7)$	1557	1597	1596
$H_g(8)$	1674	1722	1721
$A_g(1)$	617	610	–
$A_g(2)$	1679	1668	–

* unable to fit; – data was not given;† calculation was performed on the optimal C_{60}, Table 3.

In Fig. (11a), (11b), (11c), (11d), (11e), (11f) and (11g), we plot the energy changes vs. the amplitudes of two A_g modes and eight H_g modes. In these figures the zero point of energy is normalized to -7639.000eV. Results of $A_g(1)$ and $A_g(2)$ are plotted in Fig. (11b) and Fig. (11c), respectively. From Fig. (9a) and (9b), we know that A_g modes change only the single and double bond lengths R_{sb} and R_{db}. The harmonic fittings verify the validity of Eq. (1). The small linear terms indicate that the undistorted structure we use is very close to its optimal geometry. Results of $H_g(1)$ and $H_g(2)$ are plotted in Fig. (11d). Because of the mixing of the two modes, we are not able to fit them to Eq. (21). Results of $H_g(3)$ and $H_g(4)$ are in Fig. (11e), and the fittings are reasonably good. Fig. (11f) and Fig. (11g) plot the data of $H_g(5)$, $H_g(6)$ and $H_g(7)$, $H_g(8)$, respectively. The fittings are also pretty good. The resulting vibrational frequencies and linear coupling terms g_m are listed in Table 9 and Table 10, respectively. Fig. (11a) pulls all data together, from which we can compare their relative magnitudes.

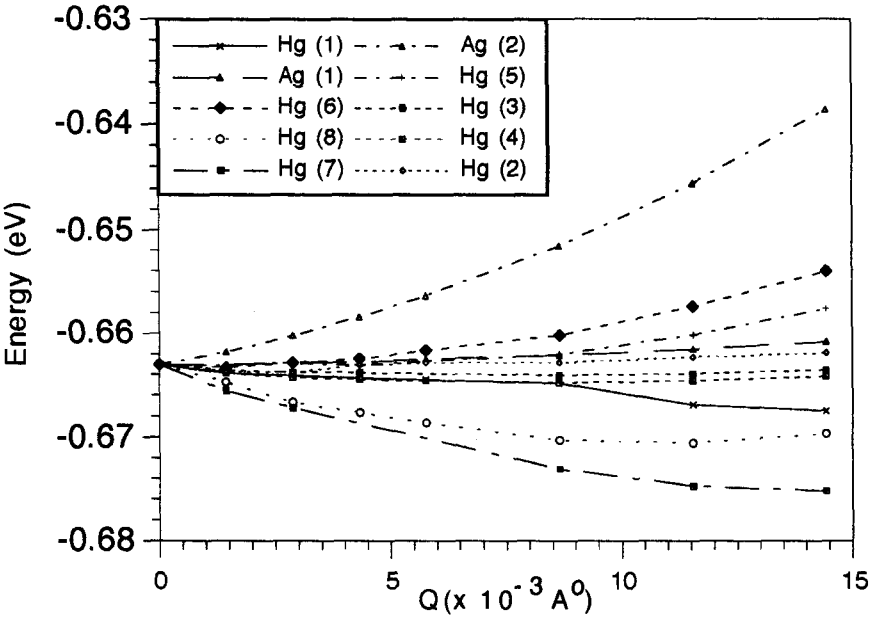

Fig. (11a), energy vs. phonon distortions.

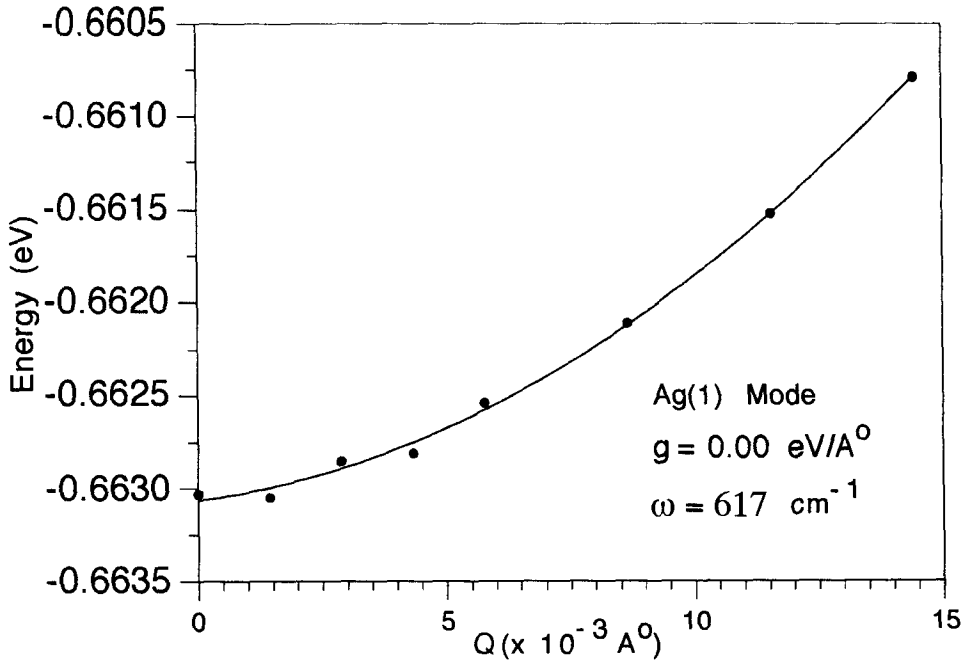

Fig. (11b), energy vs. phonon distortion.

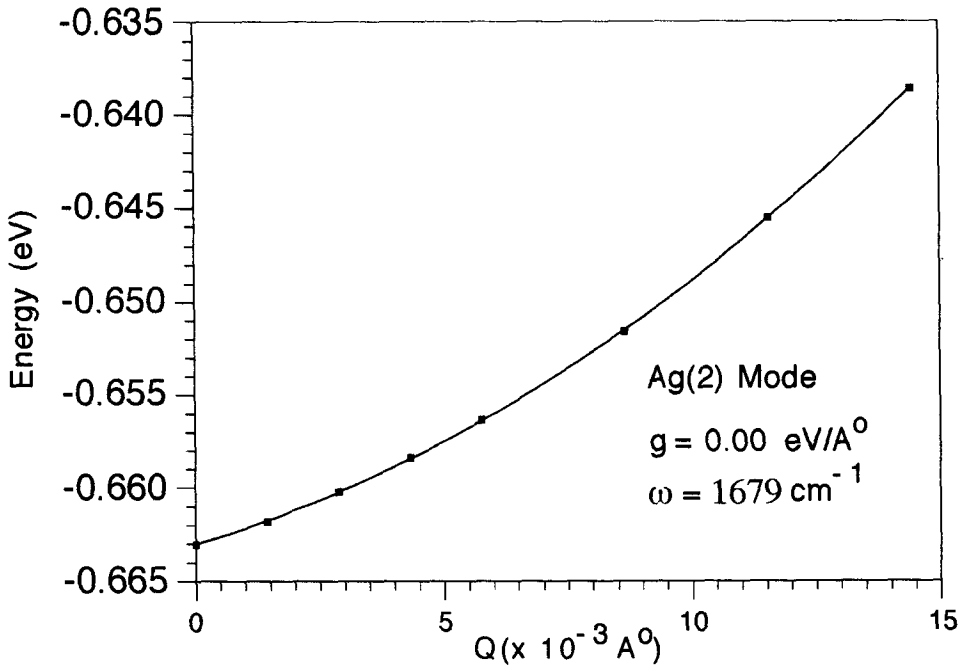

Fig. (11c), energy vs. phonon distortion.

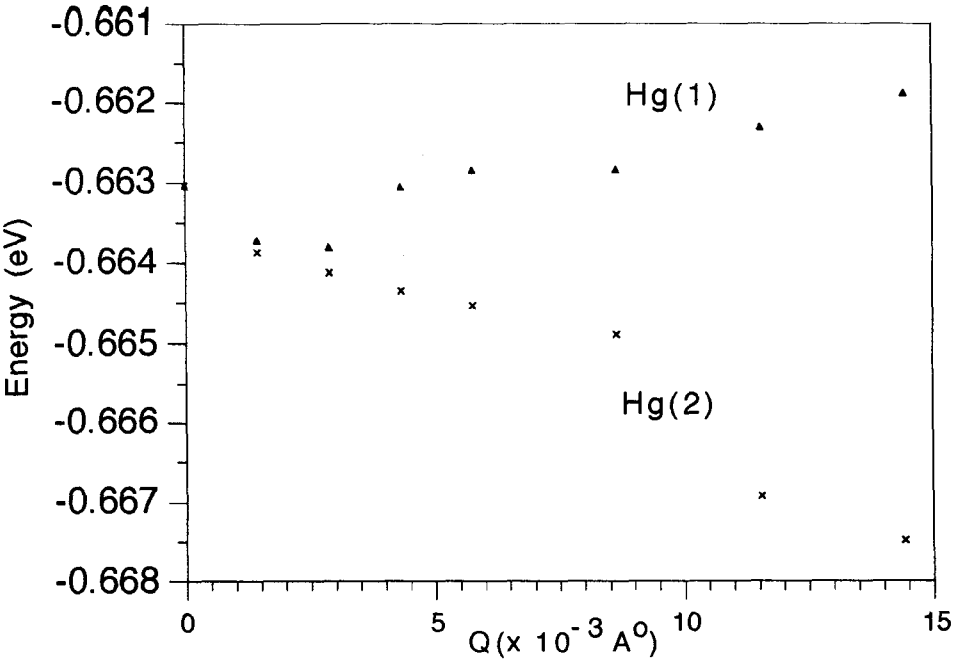

Fig. (11d), energy vs. phonon distortion.

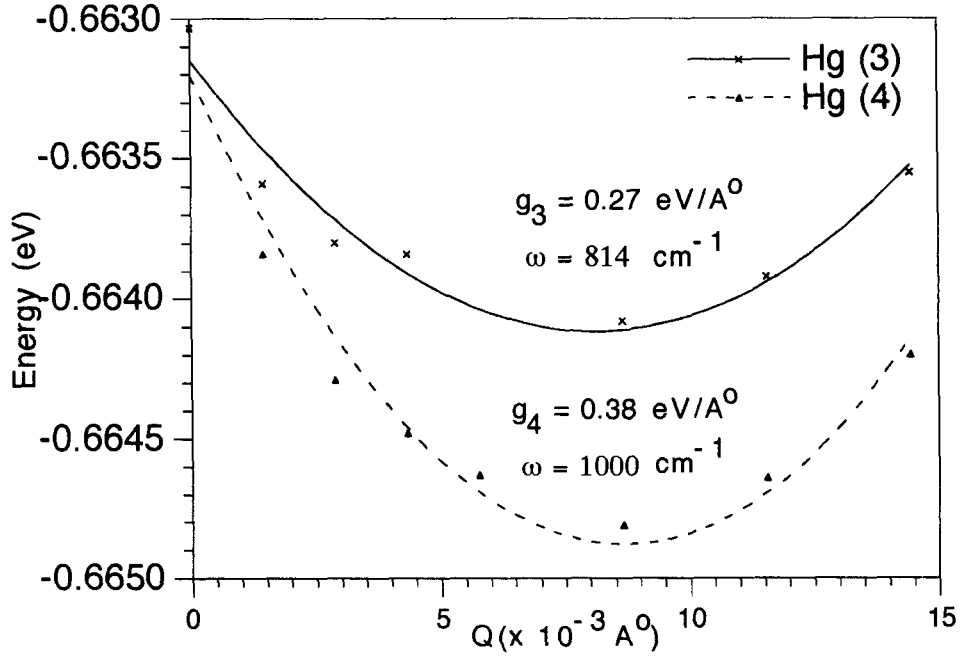

Fig. (11e), energy vs. phonon distortion.

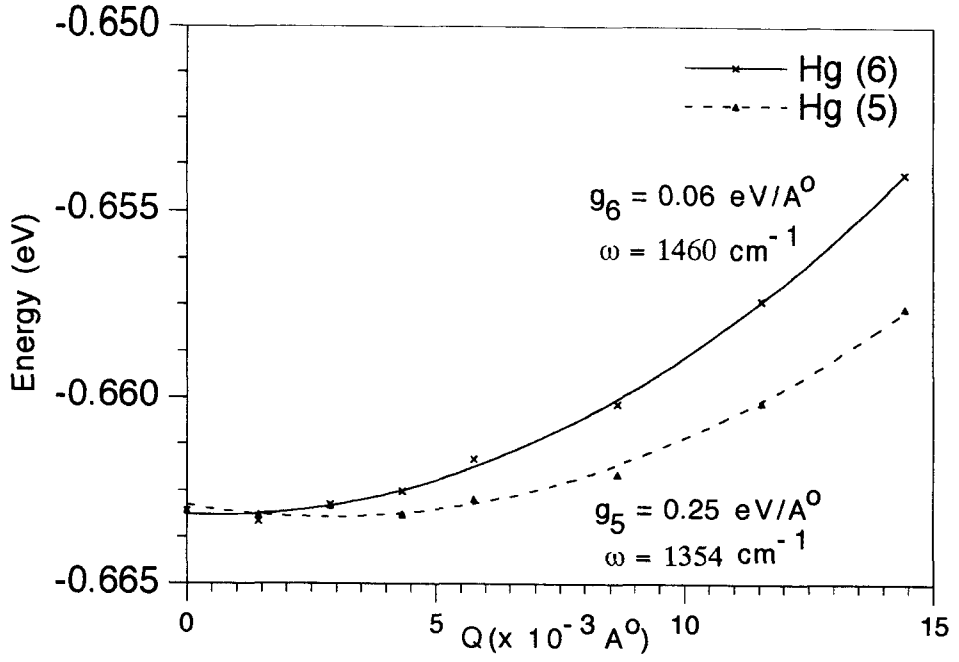

Fig. (11f), energy vs. phonon distortion.

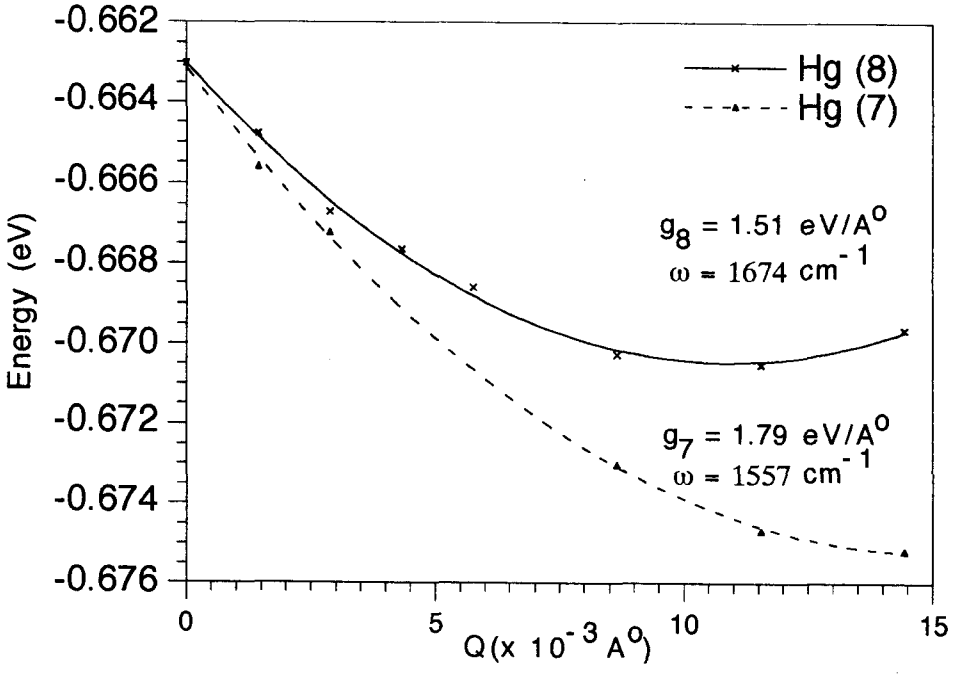

Fig. (11g), energy vs. phonon distortion.

In Table 10, we list also the result of Ref. [4], compared with which our results are fairly consistent. We can estimate g_m by looking at LUMO energy levels' splittings. In order to eliminate the contributions from phonons, we study the energy splittings of the optimized MNDO structure C_{60} and its corresponding vibrationally distorted structures with charge = 0, S = 0 and $Q_m = 5.77 \times 10^{-3}$Å. The results are listed in Table 11 with their corresponding g_m in Table 10, and are consistent with the results of fitting Eq. (21). The fact that two methods (fitting Eq. (21) and fitting Eg. (22)) give analogous values of g_m implies that our calculation is reliable. The difference between our results and those of Ref. [4] is caused by different eigenvectors of vibrations.

Table 10. Values of g_m *in Eq. (18)*

mode	Fitting Eq. (21)	Fitting Eq. (22)	Ref. [4]
$H_g(1)$	*	0.19	0.1
$H_g(2)$	*	0.16	0.1
$H_g(3)$	0.27	0.26	0.2
$H_g(4)$	0.43	0.38	0.0
$H_g(5)$	0.25	0.26	0.6
$H_g(6)$	0.06	0.12	0.2
$H_g(7)$	1.79	1.77	1.8
$H_g(8)$	1.51	1.49	1.2
$A_g(1)$	0.00	0.00	–
$A_g(2)$	0.00	0.00	–

* not able to obtain; – data were not given.

Table 11. The Splittings of LUMO†

mode	e_1(eV)	e_2(eV)	e_3(eV)
$H_g(1)$	−2.56129	−2.56037	−2.55943
$H_g(2)$	−2.56085	−2.55995	−2.55928
$H_g(3)$	−2.56112	−2.55992	−2.55855
$H_g(4)$	−2.56207	−2.55891	−2.55836
$H_g(5)$	−2.56106	−2.55865	−2.55845
$H_g(6)$	−2.56034	−2.55985	−2.55917
$H_g(7)$	−2.56962	−2.55733	−2.55224
$H_g(8)$	−2.56622	−2.56123	−2.55160
$A_g(1)$	−2.55903	−2.55903	−2.55903
$A_g(2)$	−2.54611	−2.54611	−2.54611

† the amplitudes of all phonon modes were taken as $Q_m = 5.77 \times 10^{-3}$Å.

Clearly, A_g modes do not lift the degeneracies of three T_{1u} LUMO, because they do not break I_h symmetry, and therefore there are no energy gains and no first-order electron-phonon couplings.

We calculate the following electron phonon coupling constant λ_m by fitting both Eq. (21) and Eq. (22) as described in *Sec. 2.4.3*, and then compare them with those of Ref. [4] in Table 12. In doing so, the density of states at the fermi surface is chosen the same as in *Sec. 2.3*, which is

$$N(0) = 11.5 \text{ states/eV} - \text{spin} - C_{60}.$$

2.5 Superconductivity in A_xC_{60}

2.5.1 Calculations of T_c and other Properties

1. the Transition Temperature

McMillan's formula for estimating T_c is the following[36]:

$$T_c = \frac{\Theta_D}{1.45}\exp[-\frac{1.04*(1+\lambda)}{\lambda-\mu^*(1+0.62\lambda)}], \tag{26}$$

where Θ_D is the Debye frequency.

Allen and Dynes[37] examined some very strong coupling cases ($\lambda = 0.3 \sim 10$) and found that McMillan's formula was not accurate in the very strong coupling region and that it was valid only for $\lambda \leq 1.5$. They proposed a formula of T_c which covers both weak ($\lambda \sim 0.2$) and very strong coupling ($\lambda \geq 10$) regions.

$$T_c = \frac{\Theta}{1.20}\exp(-\frac{1.04(1+\lambda)}{\lambda-\mu^*-0.62\lambda\mu^*}) \tag{27}$$

where

$$\begin{aligned}
\Theta &= f_1 f_2 \omega_{log} \\
\mu^* &= N(0)V_c/\left[1+N(0)V_c \log(E_w/\omega_{ph})\right] \\
f_1 &= [1+(\frac{\lambda}{\Lambda_1})^{3/2}]^{1/3} \\
f_2 &= 1+\frac{(\sqrt{<\omega^2>}/\omega_{log}-1)\lambda^2}{\lambda^2+\Lambda_2^2} \\
\Lambda_1 &= 2.46(1+3.8\mu^*) \\
\Lambda_2 &= 1.82(1+6.3\mu^*)(\sqrt{<\omega^2>}/\omega_{log}) \\
\omega_{log} &= \exp(\frac{2}{\lambda}\int_0^\infty \frac{d\omega}{\omega}\alpha^2(\omega)F(\omega)log\omega) \\
<\omega^2> &= \frac{2}{\lambda}\int_0^\infty d\omega\alpha^2(\omega)F(\omega) \\
N(0) &= \frac{v_0}{(2\pi)^3}\int\frac{d^2k_{\|}}{\hbar v_F},
\end{aligned} \tag{28}$$

Table 12. The Electron Phonon Coupling Constants λ_m[†]

mode	Fitting Eq. (21)	Fitting Eq. (22)	Ref. [4]
$H_g(1)$	*	0.100	0.03
$H_g(2)$	*	0.030	0.01
$H_g(3)$	0.031	0.029	0.01
$H_g(4)$	0.067	0.052	.00
$H_g(5)$	0.011	0.011	0.07
$H_g(6)$	0.000	0.002	.00
$H_g(7)$	0.340	0.333	0.39
$H_g(8)$	0.197	0.192	0.13
$A_g(1)$	0.000	0.000	–
$A_g(2)$	0.000	0.000	–
λ_d	0.776[‡]	0.749	0.64

† N(0) = 11.5 states/eV − spin − C_{60} and the values of frequencies ω_m are those obtained by C_{60}FF, see Table 5; * unable to obtain; − data were not given; ‡ data of the third column are used for $H_g(1)$ and $H_g(2)$;

where $N(0)$ is the so-called density of state at the fermi surface ($k_{||}$ is the momentum paralell to the fermi surface, v_0 is the volume of a unit cell), Θ is defined as the characteristic phonon freqeuncy, E_w is the width of conduction bands and $V_c = < 4\pi e^2/(k^2 + q_{sc}^2) >$, the average around the fermi surface. In our case,

$$\begin{aligned} \lambda &= \lambda_s + \lambda_d, \\ \omega_{log} &= \exp\left(\frac{\lambda_s \log\omega_{s,log} + \lambda_d \log\omega_{d,log}}{\lambda}\right), \\ < \omega^2 > &= \frac{1}{\lambda}(\lambda_s \omega_{s,log}^2 + \lambda_d \omega_{d,log}^2); \end{aligned} \tag{29}$$

and we choose ω_{log} as ω_{ph}.

In Table 13, we list various parameters related to the superconductivity of K_3C_{60} *vs.* the values of R_{sc}. As usual, $N(0)$ = 11.5 states/eV-spin-C_{60}, $R_\alpha = R_\beta$ = 3.55 Å and lattice parameter A = 14.2 Å. The dynamic coupling constant λ_d = 0.776 is fixed. As R_{sc} varies from 0.5 Å to 8.0 Å, λ_s/λ_d increases from 0.2 to 35, and T_c changes from $\sim$ 10°K to more than 100°K, which covers the values of the transition temperatures of most A_xC_{60}. The quantity λ_s/λ_d is an important parameter. The values of R_{sc} *vs.* the values of λ_s/λ_d are plotted in Fig. (12).

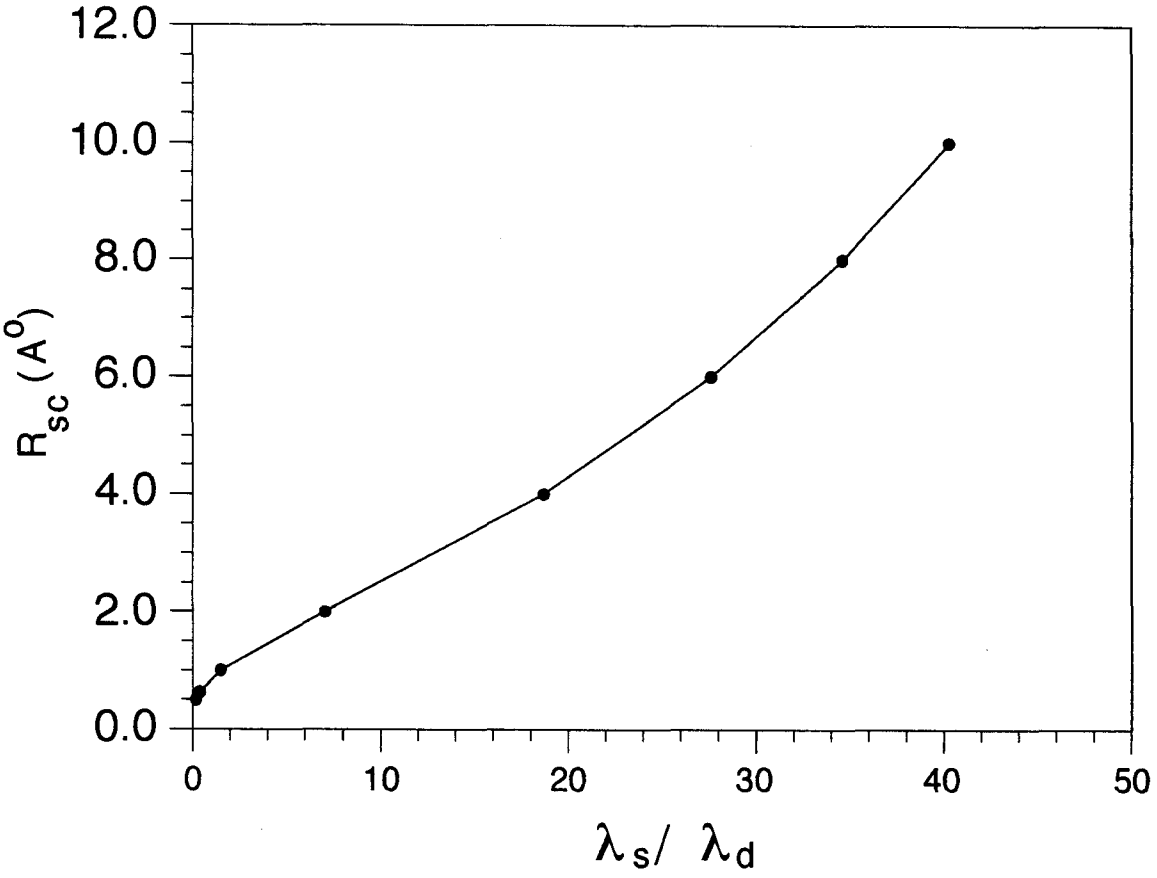

Fig. (12), the screen length vs. the ratio λ_s/λ_d; dots are actual results of calculations, and the line simply connects them.

Table 13. Transition Temperature for K_3C_{60}†

R_{sc}(Å)	ω_{log}	$\sqrt{<\omega^2>}$	μ^*	λ_s/λ_d	λ	T_c(°K)
0.50	627.3	1183	0.29	0.17	0.90	9.7
0.63	399.6	1094	0.29	0.36	1.06	11.6
0.80	214.9	958.1	0.27	0.77	1.38	16.2
1.00	119.9	810.8	0.25	1.48	1.93	17.7
2.00	42.7	452.2	0.21	7.04	6.23	20.0
4.00	31.8	290.6	0.20	18.7	15.3	45.4
6.00	29.7	242.0	0.20	27.6	22.2	77.2
8.00	28.8	217.9	0.19	34.6	27.6	102.8

† data were obtained by strictly following Eq. (27-29) and taking N(0) = 11.5 states/eV-spin-C_{60}; ω_{log} and $\sqrt{<\omega^2>}$ are in units of cm^{-1}.

2. T_c vs. Pressure

The characteristic phonon frequency Θ and the coupling constant λ determine the transition temperature T_c. When the external pressure increases, the following changes take place : 1) an increase in pressure P raises the intermolecular-phonon frequencies which is linearly proportional to the pressure P when P is small; 2) λ_s decreases because of the increases of the intermolecular phonon frequencies ($\lambda \propto 1/\omega^2$), and consequently the total coupling constant λ decreases; 3) the lattice spacing shrinks and this in turn increases the hopping matrix between the adjacent sites and the valence bandwidth, and as a result, N(0) decreases; 4) the increases in the intermolecular phonon frequencies in turn increase the characteristic phonon frequency, and in addition the decrease of λ_s decreases the contributions of the intermolecular phonon to the characteristic frequency Θ, and both factors

make Θ become larger. 5) the increases of Θ and the decrease of λ are competing, and the change of T_c depends on the result of the competition.

In *Sec. 2.3.1* we study the lattice responses to the external pressure in terms of changes of the lattice spacing and various phonon frequencies. We found that the calculated results are in good agreement with the experimental results[45]. We study here the shifts of transition temperatures T_c under the external pressure of 1 GPa. To do this, we apply 1 GPa hydrostatic pressure onto the crystal K_3C_{60} and optimize its structure. Then we calculate its phonon eigenvectors and eigenvalues, and take these data to calculate the electron-phonon coupling matrix. To calculte λ, we need to how the density of states N(0) at the fermi surface change under the pressure. We use the result of a LDA calculation[46], which reports that the change of N(0) is 20%. Table 14 lists the shifts of transition temperatures ΔT_c at different values of R_{sc}.

Table 14. T_c *vs. Pressure* (N(0) = 11.5 *states/eV-spin-*C_{60})

R_{sc}(Å)	0.50	0.63	0.80	1.00	2.00
λ_s/λ_d	0.17	0.36	0.77	1.48	7.04
$T_c\|_{1GPa}$(°K)	9.7	11.6	16.2	17.7	20.0
$\Delta T_c\|_{1GPa}$(°K)	−6.4	−8.7	−9.9	−5.8	−0.1

3. Isotope Effects

Another important issue is the isotope effect, $T_c \propto M^{-\alpha}$ for carbon atoms. That $\alpha = 0.37 \pm 0.05$ for Rb_3C_{60}[39], and 0.30 ± 0.06 for K_3C_{60}[40] have been reported. If we neglect the changes of f_1 and f_2 with respect to the isotope substitution, $^{12}C \rightarrow ^{13}C$, which is very small in many cases. According to Eq. (27,28) and

$\omega_{d,log} \propto M_C^{-\frac{1}{2}}$ (M_C is the mass of a carbon atom), we have that

$$\alpha_c = -\partial \ \log T_c / \partial \ \log M_C$$
$$\approx \frac{\lambda_d}{2\lambda} \{1 - \frac{1.04(1+\lambda)(1+0.62\lambda)\mu^{*2}}{[\lambda - \mu^*(1+0.62\lambda)]^2}\}. \quad (30)$$

If the static coupling dominates, *i.e.*, $\lambda_s/\lambda_d \ll 1.$, i.e. the static coupling limit, $\alpha_c \approx 0$, and then it contradicts the experimental observations[39,40]; If, however, $\lambda_s \sim \lambda_d$ and $\mu^* \ll 1$, $\alpha_c \sim 0.25$; if $\lambda_d \gg \lambda_s$, i.e. the dynamic coupling limit, then $\alpha_c \leq 0.5$, and both cases are consistent with the experiments[39,40].

We present below a numerical study of C isotope effects. We assume that for all eight H_g modes, their frequencies $\omega \propto M_C^{-\frac{1}{2}}$ upon isotope substituting and $\lambda_d \propto 1/M_C\omega^2$ keep the same value. Since the libration modes at $\sim 33cm^{-1}$ contribute little to λ_s, we neglect the changes of their frequencies upon substituting ^{12}C with ^{13}C. Therefore, we calculated T_c and α for the various values of R_{sc}, and results are listed in Table 15 ($N(0) = 11.5$states/eV-spin-C_{60}). For $\lambda_s/\lambda_d = 0.17$, $\alpha_c = -0.1 \leq 0$. This negative isotope effect is caused by the relatively large value of μ^*, which is 0.29, Table 15. When μ^* is large enough, the second term in the parenthesis of Eq. (30) is larger than 1, and therefore $\alpha_c \leq 0$.

Table 15. Isotope Exponents α_c *(*$N(0) = 11.5$ *states/eV-spin-*C_{60}*)*

R_{sc}(Å)	λ_s/λ_d	^{12}C T_c(°K)	^{13}C T_c(°K)	α_c
0.50	0.17	9.72	9.80	−0.10
0.63	0.36	11.62	11.60	0.02
0.80	0.77	16.17	15.30	0.15
1.00	1.48	17.69	17.47	0.16
2.00	7.04	20.03	20.04	−0.01

Clearly, either the dynamic coupling limit or the static coupling limit has difficulty explaining the observed C isotope effects. While $\lambda_s/\lambda_d = 0.7 - 1.5$, the calculated values of the exponent α_c are consistent with the experimental data[39,40], given the complexities of A_xC_{60}.

It is also interesting to study the isotope effects of the alkali elements in A_xC_{60}. We have investigated the K isotope effects by substituting ^{39}K with ^{41}K. As Eq. (30), the exponent α_k of K isotope effects is given,

$$\begin{aligned} \alpha_k &= -\partial \ \log T_c/\partial \ \log M_K \\ &\approx \frac{\lambda_s}{2\lambda}\left\{1 - \frac{1.04(1+\lambda)(1+0.62\lambda)\mu^{*2}}{[\lambda - \mu^*(1+0.62\lambda)]^2}\right\}. \end{aligned} \tag{31}$$

If the static coupling dominates, *i.e.* $\lambda_s/\lambda_d \gg 1.$, and $\mu^* \ll 1$ $\alpha_k \approx 0.5$. If $\lambda_s \sim \lambda_d$ and $\mu^* \ll 1$, $\alpha_k \sim 0.25$; if $\lambda_s \ll \lambda_d$, $\alpha_c \approx 0$. In *Sec. 2.3*, we find that $\omega \propto M_K^{-\frac{1}{2}}$ for the low frequency $(20 - 150\ cm^{-1})$ intermolecular vibrational modes. Using analogous procedures we used for α_c, we calculated the isotope exponents α_k. Results are listed in Table 16. $\alpha_k = 0.54 > 0.5$ of $\lambda_s/\lambda_d = 18.7$ is caused by the change of f_1 and f_2 of Eq. (28), which is neglected in Eq. (30,31).

Table 16. Isotope Exponents α_k *(*$N(0) = 11.5$ *states/eV-spin-*C_{60}*)*

R_{sc}(Å)	λ_s/λ_d	^{39}K T_c(°K)	^{41}K T_c(°K)	α_k
0.50	0.17	9.73	9.73	−0.02
0.63	0.36	11.62	11.61	0.02
0.80	0.77	16.17	16.08	0.12
1.00	1.48	17.69	17.48	0.23
2.00	7.04	20.03	19.59	0.44
4.00	18.7	45.42	44.21	0.54

2.5.2 Comparison with Experiments

1. a Brief Review of Experiments

Many experimental measurements of properties related to superconductivities in A_xC_{60} have been performed. Among them are the measurements of isotope effects, T_c *vs.* the external pressures, photoemissions, NMR, infrared-reflectivity, susceptibility and critical fields, tunnelings, *etc.* The properties which these experiments measured are essential to the understanding of superconductivity in A_xC_{60}. The susceptibility and critical fields measurements[18] estimated that $N(0) \approx 10 - 15$ states/eV-spin-C_{60} and a NMR measurement[42] gives an estimate of $N(0) \sim 20$ states/eV-spin-C_{60}(a LDA[10] calculation obtains that $N(0) = 13.2$ states/eV-spin-C_{60}); while an early photoemission[7] experiment reports that the density of states at the fermi surface $N(0) \approx 1.9$ states/eV-spin-C_{60}, which may be caused by the complications at the surface of the sample. A related parameter is the width of the valence band. A photoemission[7] experiment found that the bandwidth is more than 1eV; the NMR[42] inferred that the bandwidth is about 0.2eV (the LDA[10] gives a bandwidth of 0.6 eV).

The gap-T_c ratio $2\Delta/K_BT_c$ is another important parameter about which there is no consensus. Tunneling experiments[13] obtain that $2\Delta/K_BT_c \approx 5$ for both K_3C_{60} and Rb_3C_{60}, which indicates a strong coupling (LDA calculation[10] estimates that $2\Delta/K_BT_c \approx 17$); on the other hand, a far-infrared reflectivity experiment[28] concludes that $2\Delta/K_BT_c \approx 3 - 5$, which is consistent with both weak and strong coupling pictures. To determine the mechanism of the superconductivity in these systems, it is crucial to know the values of $N(0)$ and $2\Delta/K_BT_c$ and others.

T_c have large negative shifts under pressures in these alkali fullerenes, *i.e.*,

$\partial T_c/\partial P \leq 0$. Experiments found that the value of $\partial T_c/\partial P$ ranges from -0.63 to -0.78 °K kbar^{-1} [12,38], and under the external pressure of 1 GPa,the shift of the transition temperature T_c is about -7°K[12]. Isotope effects ($T_c \propto M^{-\alpha}$) are intimately related to the phonon-mediated pairing mechanism and is an important signature in determining the mechanism of any superconducting materials. Several results have been reported. An early report[41] put the exponent α_c to be 1.4 ± 0.5. And later experiments find that $\alpha_c = 0.37 \pm 0.05$ for Rb_3C_{60}[39], and 0.30 ± 0.06 for K_3C_{60}[40]. Existence of relatively large isotope effects [39,40] favors strongly the phonon-mediated pairing mechanisms.

Other important quantities are the coherent length ξ_0, the penetration depth λ_L and critical fields H_{c1} and H_{c2}. Ref. [43] reported that $H_{c1}(0) \approx 130$G and $H_{c2}(0) \approx 50$T as the temperature goes to zero. From the value of H_{c2}, the coherent length $\xi_0 = 26$Å for K_3C_{60} has been obtained because $H_{c2}(0) = \hbar c/2e\xi_0^2)$[43]. The muon spin relaxation technique (μSR) has been widely applied to study the penetration depth λ_L in many type-II superconductors[44], including high-T_c superconductors. In transverse-field μSR experiments, an external field H_{ext} ($H_{c1} \ll H_{ext} \ll H_{c2}$) is applied, and in the superconducting phase H_{ext} forms a lattice of flux vortices, resulting in a local magnetic field having a distribution of a width $\Delta B \propto \lambda_L^{-2}$. Therefore, the muon spin relaxation rate[44] $\psi \propto \Delta B \propto \lambda_L^{-2}$. For K_3C_{60}, Ref. [44] obtained $\lambda_L \approx 4,800$Å. A point to be noticed is that the short coherent length ξ_0 and high critical field H_{c2} resemble those of high-T_c superconductors[44].

2. Comparisons of theory and experiments

Table 17a Superconducting properties at different values of R_{sc}

R_{sc}(Å)	N(0)†	T_c(°K)⋆	λ_s/λ_d	μ^{*}‡	λ	$\alpha_c^{\diamond}$	$\Delta T_c\|_{1GPa}$(°K)◁	$\alpha_k^{\diamond}$
0.50	21.3	18.7	0.17	0.46	1.67	−0.47	−8.5 (−9.4)	−0.08
0.63	15.6	19.0	0.36	0.35	1.43	0.005	−11.9 (−8.8)	∼ 0
0.80	12.9	19.0	0.77	0.29	1.55	0.16	−10.3 (−5.3)	0.12
1.00	12.4	19.0	1.48	0.25	2.08	0.15	−5.4 (+0.1)	0.24
2.00	10.7	19.0	7.04	0.20	5.80	0.002	−0.1 (+3.2)	0.44
4.00	5.20	19.0	18.7	0.17	6.92	−0.07	−3.2 (−0.3)	0.52
6.00	3.59	19.0	27.6	0.16	6.95	−0.08		0.54
8.00	2.87	19.0	34.6	0.15	6.89	−0.08		0.54
exp.	10 − 20	∼ 19	-	-	-	∼ 0.3	∼ −7	-

† the values of N(0) were tuned to yield the experimental value of T_c (19 °K) while $N(0)E_w$ is kept constant, and N(0) is in units of states/eV-spin-C_{60}; ‡ the values of μ^* were calculated according to Eq. (28); ⋆ the fitted values of T_c resulted by tuning N(0). ◇ $\delta T_c(^{13}C) \approx -0.5$ °K; $\delta T_c(^{39}K) \approx -0.1$ and -0.2 °K for $\alpha_k = 0.1$ and 0.2, respectively; ◁ the data are calculated with $N(0) = 0.8 \times 11.5$ states/eV-spin-C_{60} for P = 1GPa according to a LDA calculation[47] while those in parenthes are calculated without modifying the value of N(0) (N(0) = 11.5 states/eV-spin-C_{60}); − not available.

In *Sec. 2.5.1* N(0) = 11.5 states/eV-spin-C_{60} is used, and in many cases the values of T_c are not consistent with the experimental result T_c = 19 °K for K_3C_{60}[1]. However, in order to compare with experiments, we need to fit T_c to the experiment value 19 °K. Since there is no consensus on the exact value of N(0) which ranges from ~ 2 °K to ~ 20 °K, we take it as a tuning parameter to fit T_c to 19 °K, and at the same time we keep the value of $N(0)E_w$ fixed. Using the same procedures as in *Sec. 2.5.1*, we calculated $\Delta T_c|_{1GPa}$, α_c and α_k. Results are listed in Table 17a. For the case of $\lambda_s/\lambda_d = 0.17$, because the value of μ^* is quite large and changes with N(0), we had difficulty in fitting it exactly to 19 °K; instead, we tuned T_c to 18.7 °K, which is close enough to 19 °K to give a reliable comparison to experiments.

Isotope shifts are useful in determining the mechanism of superconductivity. For $\lambda_s/\lambda_d = 0.17$, $\alpha_c = -0.47$ (a large negative isotope shift), is caused by a large value of μ^*, and this is explained in the previous section. When $\lambda_s/\lambda_d \approx 0.4$, $\alpha_c \approx 0$; this is again caused by the relatively large value of μ^*, which is about 0.35. Should $\mu^* \ll 1$, α_c for both of the above two cases should be close to 0.5; when $\lambda_s/\lambda_d \approx 0.77 - 1.5$, $\alpha_c \approx 0.15$; considering the complexities of the problem, it is conceivable that this may explain the experimental observation[40] $\alpha_c = 0.30 \pm 0.06$. When $\lambda_s/\lambda_d \approx 7$ or more, α_c is very small or slightly negative, which is caused by small changes of f_1 and f_2 in Eq. (27,28) and which is the result of the different responses of ω_{log} and $\sqrt{<\omega^2>}$ to the isotope substitution ($^{12}C \rightarrow ^{13}C$). By comparing the above observations to the experiments[39,40], we conclude that λ_s/λ_s should be ~ 1.

A_xC_{60} has a large negative $\partial T_c/\partial P$. This is caused by changes of both N(0) and phonon frequencies. The effect that is due to changes of frequence has two

sides or facets : The increase of $< \omega >$ increases the characteristic frequency Θ but decreases λ_s because $\lambda \propto 1/\omega^2$. When $\lambda_s/\lambda_d \approx 0.2 - 1.5$, $\Delta T_c|_{1GPa} \approx -5 \sim -12$ °K consistent with the experiments[12,38].

Other parameters to be noticed are N(0), λ and μ^*. N(0) decreases as λ_s/λ_d increases; when $\lambda_s/\lambda_d \ll 1$, N(0) has to be $\sim$ 20 states/eV-spin-C_{60} to give rise to $T_c \approx 19$ °K; this is because λ_d is small. At $\lambda_s/\lambda_d \gg 1$ $\lambda \approx 6 - 7$, and this corresponds to a extremely strong coupling superconductivity; while at $\lambda_s/\lambda_d \ll 1$, $\lambda \approx 1.5$, which is a modest strong coupling superconductor. The values of μ^* are quite interesting, decreasing from 0.46 at $\lambda_s/\lambda_d = 0.17$ to 0.15 at $\lambda_s/\lambda_d = 34.6$. The relatively large value of μ^* at $\lambda_s/\lambda_d \ll 1$ is caused by a small ratio of $E_w/ < \omega >$, and requires a modest coupling strength to give rise to $T_c = 19$ °K. In their proposal, Varma *et al.*[4] used $\mu^* \approx 0.1 - 0.2$ to obtain the appropriate value of T_c and they argued that since the actual electronic structure of A_xC_{60} consists of a ladder of many bands of width $\sim$ 1 eV spreading out $\sim$ 20 eV, the value of μ^* should be close to those of conventional superconductors, which range from $\sim$ 0.1 to $\sim$ 0.2 [36]. This needs further investigation.

Actually, there are no good estimates of μ^*, except that the values of μ^* increase as bandwidth E_w shrinks and as phonon frequencies increase. As Varma *et al.*[4] pointed out, the value of μ^* could be close to those of conventional superconductors, which are $\sim$ 0.1 to $\sim$ 0.2. We took $\mu^* = 0.2$ and tuned N(0) to fit the transition temperature to its experimental value $T_c = 19$ °K; then we recalculated everything in Table 17a except $\Delta T_c|_{1GPa}$. Results are listed in Table 17b.

Table 17b. Superconducting properties at different values of R_{sc} ($\mu^* = 0.2$)†

R_{sc}(Å)	N(0)‡	T_c(°K)	λ_s/λ_d	λ	$\alpha_c^{\triangleleft}$	$\alpha_k^{\triangleleft}$
0.50	10.2	19.0	0.17	0.81	0.43	0.04
0.63	10.1	19.0	0.36	0.93	0.37	0.13
0.80	10.1	19.0	0.77	1.21	0.44	0.22
1.00	10.6	19.0	1.48	1.78	0.20	0.30
2.00	10.6	19.0	7.04	5.75	0.01	0.49
4.00	5.75	19.0	18.7	7.65	−0.07	0.56
6.00	4.15	19.1	27.6	8.04	−0.08	0.59
8.00	3.38	19.0	34.6	8.13	−0.08	0.59

† the value of μ^* is kept to 0.2; ‡ the values of N(0) were tuned to yield the experimental value of T_c and N(0) is in units of states/eV-spin-C_{60}; $\triangleleft$ values were calculated by the procedures described in *Sec. 2.5.1.*

In Table 18, we summarize the various cases. We list the values of λ, T_c and the experimental result that can be explained and that can not be explained under the different situations. Table 18 is constructed according to Table 17a. In doing so, we consider the deviations between the calculated and the experimental data within 30% consistent, except for isotope exponents α_c, we consider $\alpha_c \approx 0.15$ consistent with the experimental result[40] 0.30 ± 0.06. We also need to estimate the values of $2\Delta/K_BT_c$ in order to compare with the results of infrared -reflectivity[28] and tunneling[13] experimental results. To do this, we took the result of Ref. [45] to estimate the value of $2\Delta/K_BT_c$.

Table 18. Comparison to Experiments*

λ_s/λ_d	R_{sc}(Å)	λ	μ^*	consistent	inconsistent
0.17	0.50	1.67	0.46	pressure, , NMR infrared, tunneling† suscep.&crit.field, T_c	isotope†
0.36	0.63	1.43	0.35	pressure, NMR infrared, tunneling† suscep.&crit.field, T_c	isotope†
0.77	0.80	1.55	0.29	infrared, tunneling pressure, isotope NMR, T_c suscep.&crit.field	
1.48	1.00	2.08	0.25	infrared, tunneling isotope‡, pressure NMR, T_c suscep.&crit.field	
7.04	2.00	5.80	0.20	infrared tunneling	isotope, NMR pressure, $T_c(Rb_{3-x}Cs_xC_{60})$ suscep.&crit.field

$\star$ NMR and suscep. & crit. fiald measure the values of N(0) and E_w; "pressure effects" experiments measure the value of $\partial T_c/\partial P$; tunneling and infrared-reflectivity measure the ratio of $2\Delta/K_BT_c$; isotope experiments measure the value of the exponent α_c; photoemission experiment is not included in the comparison because it is in serious disagreement with LDA calculations and other experiments; † if we take $\mu^* \ll 1$, we expect a large positive value of α_c for for $\lambda_s/\lambda_s \leq 0.4$ according to Eq. (30), which is consistent with the experiments[40], for instance, $\alpha_c = 0.37$ if $\mu^* = 0.2$, Table 17b; however, λ will decrease so that the calculated $2\Delta/K_BT_c$ will not be consistent with the tunneling experiment[13].

We summarize various cases into three catalogues : the static coupling limit, $\lambda_s/\lambda_d \gg 1$; the intermediate region, $\lambda_s/\lambda_d \sim 1$; and the dynamic coupling limit, $\lambda_s/\lambda_d \ll 1$. In Table 19 we summarize the three cases.

Table 19. Summary*

λ_s/λ_d	λ	consistent	inconsistent
$\gg 1$	~ 6	infrared	isotope
		tunneling	pressure
		suscep.&crit.field	NMR
			$T_c(Rb_{3-x}Cs_xC_{60})$
$\ll 1$	~ 1	pressure, NMR	isotope†
		infrared, tunneling†	
		suscep.&crit.field, T_c	
~ 1	~ 2	isotope, pressure	
		infrared, NMR	
		tunneling, T_c	
		suscep.&crit.field	

$\star$ for the descriptions of experiments, see the captions of Table 18 and *Sec. 2.5.2* (1); photoemission experiment is not included in the comparison because it is in serious disagreement with LDA calculations and other experiments; $\dagger$ if we take $\mu^* \ll 1$, we expect a large positive value of α_c for for $\lambda_s/\lambda_s \leq 0.4$ according to Eq. (30), which is consistent with the experiments[40], and then, however the calculated ratio of $2\Delta/K_BT_c$ will be too small to fit that of the experiment[13].

Taking the results of far-infrared relectivity experiment[28], *i.e.*, $2\Delta/K_BT_c \approx 3-5$, $\xi_0 = \hbar v_f/\pi\Delta \approx 25-40$ Å for K_3C_{60}, and the experimental result[43] $\xi_0 \approx 26$ Å.

The static coupling limit, $\lambda_s/\lambda_d \gg 1$, has serious problems. Because the characteristic phonon frequency is small, being $20 \sim 30cm^{-1}$, it requires an extremely large value of λ (more than 10) to explain the observed value of the transition temperature T_c, ~ 30 °K for $Rb_{3-x}Cs_xC_{60}$ [14,15,16]. In addition, it is difficult to explain a large negative value of $\partial T_c/\partial P$[12,38], and it can not explain the ^{13}C isotope shift of T_c[39,40]. Therefore, the static coupling limit is safely ruled out.

The dynamic coupling limit, $\lambda_s/\lambda_d \gg 1$, is consistent with many experimental observations[1,12,14,15,38-40] except for those of the tunneling[13] and the photoemission[7] experiments. If we take smaller value of μ^* as suggested by Varma *et al.*[4], we will have values of α_c consistent with experiments[39,40]. As pointed out before, results of the tunneling[13] and the photoemission[7] experiments are contradictory to other experiments[18,28,42]. From experimentalists' point of view, the dynamic coupling limit is still a possibility. However, the dynamic coupling limit corresponds to cases $R_{sc} \leq 0.5$ Å, which is too small and unlikely.

Properties of the intermediate region, $\lambda_s/\lambda_d \sim 1$, is consistent with most of the experimental observations except for one photoemission experimental report[7] whose results are in dispute[18,42]. We conclude that most likely $\lambda_s/\lambda_d \approx 0.8-1.5$. An experiment on K isotope effects , replacing ^{39}K by ^{41}K, may help us verify the above conclusion. Again, depending on the values of μ^*, the values of isotope exponent α_k vary. Using our values of μ^*, we predict that $\alpha_k \approx 0.1 - 0.2$; assuming that $\mu^* \ll 1$, we have $\alpha_k = 0.2 - 0.2$ according to Eq. (31). Therefore, an observation of a positive K isotope shift $\alpha_k \approx 0.1 - 0.3$ will confirm our above conclusion.

The correlation length ξ_0 is very short. This is because the fermi velocity v_f is small and the gap Δ is relatively large. Taking the results of far-infrared relectivity experiment[28], *i.e.*, $2\Delta/K_BT_c \approx 3-5$, $\xi_0 = \hbar v_f/\pi\Delta \approx 25-40$ Å for K_3C_{60}, and the experimental result[43] $\xi_0 \approx 26$ Å.

One more thing is to be noted : If we take $N(0) \approx 2$ states/eV-spin-C_{60}, as a photoemission measurement[7] reported, only the static coupling limit $\lambda_s/\lambda_d \gg 1$ or $R_{sc} \gg 1$ gives rise to the observed $T_c = 19$ °K for K_3C_{60}[1]. Since the static coupling limit can not explain many established experiments, as described earlier, we conclude that $N(0) = 10-20$ states/eV-spin-C_{60}, as suggested by many other experiments[18,42] and LDA calculations[10].

The main conclusions of our studies :

1) The "SMS" mechanism as suggested by some groups[5] is unlikely;
2) $N(0) \approx 10-20$ states/eV-spin-C_{60} as reported by critical field & normal state susceptibility[18] and NMR[42] measurements, unless the superconductivity in A_xC_{60} are caused by some exotic mechanisms;
3) $R_{sc} \approx 0.8-1.0$ Å or $\lambda_s/\lambda_d \sim 0.8-1.5$ is most likely;
4) $\alpha_k \approx 0.1-0.2$ is predicted and an experiment on K isotope effects is encouraged.

To summarize, we have calculated the electron-phonon coupling constant: both static and dynamic (Jahn-Teller) coupling constants, and have identified a plausible mechanism of superconductivity in A_xC_{60}. To confirm our findings, a K isotope effect experiment is suggested .

References

1. A. F. Hebard *et al.*, *Nature* **350**, 600 (1991).
2. P. J. Benning *et al.*, *Science* **252**,1417 (1991)
3. P. W. Stephen *et al.*, *Nature* **351**, 632 (1991).
4. C. M. Varma, J. Zaanen and K. Raghavachari, *Science* **254**, 989 (1991)
5. S. Chakravarty, M. P. Gelfand and S. Kivelson, *Science* **254**, 970 (1919); G. Baskaran and E. Tosatti, *Current Science* **61**, 33 (1991)
6. F. C. Zhang, M. Ogata and T. M. Rice, *Phys. Rev. Lett* **67**, 3452 (1991)
7. C. T. Chen *et al.*, *Nature* **352**, 603 (1991)
8. Y. Guo, N. Karasawa and W. A. Goddard III, *Science* **351**, 464 (1991).
9. N. Karasawa, G. Chen, Y. Guo, and W. A. Goddard III, unpublished.
10. Steven C. Erwin and Warrwn E. Pickett, *Science* **254**, 842 (1991)
11. S. Saito and A. Oshiyama, *Phys. Rev. Lett.* **66**, 2637 (1991).
12. G. Sparn *et. al.*, *Science* **252**, 1829 (1991); R. M. Fleming *et. al.*, *Nature* **352**, 787 (1991)
13. Z. Zheng *et al.*, *Nature* **353**, 333 (1991); Z. Zheng and C. M. Lieber, *Mod. Phys. Lett.* B **5**, 1905 (1991).
14. M. J. Rosseinsky *et al.*, *Phys. Rev. Lett.* **66**, 2830 (1991).
15. K. Holezer *et al.*, *Science* **252**, 1154 (1991).
16. K. Tanigaki *et al.*, *Nature* **352**, 222 (1991).
17. K. Tanigaki *et al.*, *Nature* **356**, 419 (1991).
18. A. P. Ramirez, M. J. Rosseinsky, D. W. Murphy, R. M. Fleming, and R. C. Haddon, *Bulletin of the American Physical Society* **37**, 714 (Mar. 1992).
19. W. P. Su, J. R. Schrieffer and A. J. Heeger, *Phys. Rev. Lett.* **42**, 1689 (1979)

20. M. J. S. Dewar and W. Thiel, *J. Am. Chem. Soc.* **99**, 4899 (1977); *ibid*, 4907 (1977).

21. C. S. Yannoni *et al.*, *J. AM. Chem. Soc.* **113**, 3190 (1991).

22. M. Haesen, J. Almlof, G. E. Scuseria, *Chem. Phys. Lett.* **181**, 497 (1991).

23. S. C. Erwin and W. E. Pickett, *Sicence* **254**, 842 (1991).

24. L. S. Wang *et al.*, *Chem. Phys. Lett.* **179**, 449 (1991).

25. S. L. Mayo, B. D. Olafson and W. A. Goddard III, *J. Phys. Chem.* **94**, 8897 (1990).

26. W. A. Goddard III and N. Karasawa, submitted to *J. Phys. Chem.*.

27. Y. Guo and W. A. Goddard III, to be submitted.

28. L. D. Rotter *et al.*, *Nature* **355**, 532 (1992).

29. G. D. Mahan, in *Many-Particle Physics*, Plenum Press, (1981), p.420.

30. R. E. Stanton and M. D. Newton, *J. Phys. Chem.* **92**, 2141 (1988).

31. F. A. Cotton, in *Chemical Applications of Group Theory*, Wiley-Interscience.

32. J. Bourgion and M. Lannoo, in *Points Defects in Semiconductors, II. Experimental Aspects*, Springer Series in Solid-State Sciences Vol. 35 (Springer-Verlag,Berlin, 1983).

33. K. H. Johnson, M. E. Mchenry and D. P. Clougherty, *Physica C* **183**, 319 (1991).

34. M. Lannoo, G. A. Baraff, M. Schluter and D. Tomanek, *Phys. Rev. B* **44**, 12106 (1991); M. Schuluter *et al.*, *Phys. Rev. Lett.* **68**, 526 (1992).

35. M. C. O'Brien, *J. Phys. C: Solid state Phys.* **4**, 2524 (1971).

36. W. L. McMillan, **Phys. Rev. 167**, 331 (1968)

37. P. B. Allen and R. C. Dynes, *Phys. Rev. B* **12**, 905 (1991)

38. J. E. Schirber *et al.*, *Physica C* **178**, 137 (1991).

39. A. P. Ramirez *et al. Phys. Rev. Lett.*, **68**, 1058 (1992).

40. C.-C. Chen and C. M. Lieber, *High-*T_c *Update* (Mar. 3, 1992), p.1.

41. T. W. Ebbesen *et al. Nature* **355**, 620 (1992).

42. R. Tycko *et al.*, *Science* **253**, 884 (1991).

43. K. Holczer *et al.*, *Phys. Rev. Lett.* **67**, 271 (1991).

44. Y. J. Uemura *et al.*, *Nature* **352**, 605 (1991).

45. O. Zhou *et al.*, *Science* **255**, 833 (1992).

46. A. Oshiyama and S. Saito, *Solid State Comm.* **82**, 41 (1992).